

WIDE-BAND ANTENNA DESIGN FOR USE IN MINIMAL-SCAN, MICROWAVE  
TOMOGRAPHIC IMAGING

By

Jacob Klaser

A THESIS

Submitted to  
Michigan State University  
in partial fulfillment of the requirements  
for the degree of

Electrical Engineering - Master of Science

2013

## ABSTRACT

### WIDE-BAND ANTENNA DESIGN FOR USE IN MINIMAL-SCAN, MICROWAVE TOMOGRAPHIC IMAGING

By

Jacob Klaser

Microwave tomography is widely-used in biomedical imaging and non-destructive evaluation of dielectric materials. A novel microwave tomography system that uses an electrically-deformable mirror to steer the incident energy for producing multi-view projection data is being developed in the Non-Destructive Evaluation Laboratory (NDEL). Such a system will have a significant advantage over existing tomography systems in terms of simplicity of design and operation, particularly when there is limited-access of the structure that is being imaged. The major components of a mirror-based tomography system are the source mirror assembly, and a receiver array for capturing the multi-view projection data. This thesis addresses the design and development of the receiver array.

This imaging array features balanced, anti-podal Vivaldi antennas, which offer large bandwidth, high gain and a compact size. From the simulations, as well as the experimental results for the antenna, the return loss ( $S_{11}$ ) is below -10dB for the range from 2.2GHz to 8.2GHz, and the gain is measured to be near 6dB. The data gathered from the receiver array is then run through MATLAB code for tomographic reconstruction using the Filtered Back-Propagation algorithm from limited-view projections. Initial results of reconstruction from the measured data shows the feasibility of the approach, but a significant challenge remains in interpolating the data for a limited number of receiving antenna elements and removing noise from the reconstructed image.

## ACKNOWLEDGEMENTS

I would like to express my sincerest thanks to my advisor, Dr. Lalita Udpa, for providing me with the opportunity to be a part of this research in the Non-Destructive Evaluation Laboratory at MSU. I would also like to thank Dr. Satish Udpa and Dr. Prem Chahal for their assistance in the research, as well as for their service on my committee.

I would also like to thank the ECE Technical Services for their assistance in fabrication and testing of the antenna array and subsequent components; their help has been invaluable. Also, a large thank-you to Pavel and Amin, for all of the assistance you gave while we worked on developing this innovative microwave tomography system.

Finally, I would like to thank my family, my fiancé, Megan, and all of my friends for their support and encouragement during my time completing this research. I would also like to thank God for giving me the ability, patience and knowledge to complete this project.

# TABLE OF CONTENTS

LIST OF TABLES .....	vi
LIST OF FIGURES .....	vii
<b>Chapter 1 - Introduction</b> .....	<b>1</b>
1.1 - Research Background .....	1
1.2 - Objective .....	2
1.3 - Organization of Thesis .....	3
WORKS CITED .....	5
<b>Chapter 2 - Theory</b> .....	<b>7</b>
2.1 - Introduction .....	7
2.2 - Fourier Diffraction Theorem .....	9
2.3 - MSFBPP Implementation Process .....	14
WORKS CITED .....	20
<b>Chapter 3 - Microstrip Antennas</b> .....	<b>22</b>
3.1- Introduction .....	22
3.2 - Patch Antennas .....	22
3.3 - Series and Corporate-Fed Antennas .....	24
3.4 - Microstrip Log-Periodic Antennas .....	26
3.5 - Tapered-Slot Antennas .....	27
WORKS CITED .....	33
<b>Chapter 4 - Antenna Simulation Results</b> .....	<b>35</b>
4.1 - Introduction .....	35
4.2 - Simulated Results .....	35
WORKS CITED .....	51
<b>Chapter 5 - Antenna Control</b> .....	<b>53</b>
5.1 - Introduction .....	53
5.2 - Initial Designs.....	54
5.3 - Fully-Automated Switching System .....	56
5.4 - LabVIEW Control .....	58
WORKS CITED .....	63
<b>Chapter 6 - Simulations for Antenna Control</b> .....	<b>65</b>
6.1 - Introduction .....	65
6.2 - Design Procedures and Results .....	65
WORKS CITED .....	73
<b>Chapter 7 - System Measurements</b> .....	<b>75</b>
7.1 - Introduction .....	75
7.2 - Antenna Measurement Results .....	76

7.3 - System Measurements of Microwave Switch .....	81
7.4 - Polarization Measurements of Receiver Array Antennas .....	83
7.5 - Complete System Measurements .....	86
7.6 - Initial Reconstruction Results .....	100
WORKS CITED .....	103
<b>Chapter 8 - Conclusions and Future Work .....</b>	<b>105</b>
8.1 - Summary .....	105

## LIST OF TABLES

Table 5.1 - Truth Table for Antenna Control Via Microwave Switch [3].....59

Table 5.2 - Control Logic Sequence for 20-Element Antenna Array .....60

## LIST OF FIGURES

Figure 1.1 - Schematic of Mirror for Microwave Tomography System. For interpretation of the references to color in this and all other figures, the reader is referred to the electronic version of the thesis.....	2
Figure 1.2 - Proposed System Layout.....	3
Figure 2.1 - Graphical Representation of the Fourier Slice Theorem [1].....	8
Figure 2.2 - Graphical Representation of the Fourier Diffraction Theorem [2].....	10
Figure 2.3 - 360° Coverage of Fourier Space.....	11
Figure 2.4 - 270° Coverage of Fourier Space.....	12
Figure 2.5 - Simulated Scattered Data.....	15
Figure 2.6 - Effect of Weight Filters on Reconstruction of Simple Object.....	16
Figure 2.7 - Weighted and Un-Weighted Reconstruction Results for MATLAB Code....	17
Figure 2.8 - Total Variation Regularization Applied to MSFBPP Images.....	18
Figure 3.1 - Microstrip Antenna Fringing and Radiating Fields [3].....	23
Figure 3.2 - Radiating Edges of Patch Antenna [3].....	23
Figure 3.3 - Microstrip Log-Periodic Antenna with Inset-Fed Patches.....	26
Figure 3.4 - TSA Types [9].....	28
Figure 3.5 - Slot-line Radiation for Vivaldi Antenna [6].....	29
Figure 3.6 - Radial Stub for Feeding Vivaldi Antenna [11].....	30
Figure 3.7 - Anti-Podal Vivaldi Antenna [11].....	30
Figure 3.8 - Balanced, Anti-Podal Vivaldi Antenna[11].....	31
Figure 4.1 - Patch Antenna Layout.....	36
Figure 4.2 - $S_{11}$ for Patch Antenna.....	37
Figure 4.3 - Layout of 4x2 Patch Array.....	38

Figure 4.4 - Return Loss for 4x2 Patch Antenna Array .....	39
Figure 4.5 - Layout of Corporate Series-Fed Antenna .....	40
Figure 4.6 - Return Loss of Corporate Series-Fed Antenna .....	41
Figure 4.7 - Log-Periodic Microstrip Antenna Layout.....	42
Figure 4.8 - Return Loss of 5-Element Log-Periodic Microstrip Antenna.....	43
Figure 4.9 - 18-Element Log-Periodic Microstrip Antenna.....	44
Figure 4.10 - Return Loss of 18-Element Log-Periodic Antenna.....	44
Figure 4.11 - Vivaldi Antenna Layout.....	45
Figure 4.12 - Front and Back Layer of Vivaldi Antenna.....	45
Figure 4.13 - Simulated Return Loss of Vivaldi Antenna .....	46
Figure 4.14 - Layout of Anti-Podal Vivaldi Antenna.....	47
Figure 4.15 - Simulated Return Loss of Anti-Podal Vivaldi Antenna.....	48
Figure 4.16 - Layout of Balanced, Anti-Podal Vivaldi Antenna .....	48
Figure 4.17 - Simulated Return Loss of Balanced, Anti-Podal Vivaldi Antenna.....	49
Figure 4.18 - Simulated Gain of Balanced, Anti-Podal Vivaldi Antenna at 6GHz .....	50
Figure 5.1 - Control for Multiple Microwave Switches .....	53
Figure 5.2 - Initial Switch Design with HP Coaxial Switch.....	55
Figure 5.3 - Series and Shunt Configurations for PIN Diode Switches [1].....	56
Figure 5.4 - Hittite HMC345LP3 Microwave Switch .....	57
Figure 5.5 - Schematic of Hittite HMC345LP3 Chip and Evaluation Board .....	58
Figure 5.6 - Parallel Port Pin-Out .....	60
Figure 5.7 - Stepper Motor.....	62
Figure 6.1 - Series and Shunt PIN Diode Switches [1].....	66

Figure 6.2 - S-Parameters for SPDT in Reverse-Biased Mode .....	68
Figure 6.3 - SPDT in Forward-Bias Model .....	69
Figure 6.4 - SP4T for Switch 4 Selected.....	70
Figure 6.5 - SP4T for Switch 3 Selected.....	71
Figure 6.6 - HMC345LP3 Return Loss Parameters from Data Sheet [4] .....	72
Figure 7.1 - Receiver Array Setup .....	76
Figure 7.2 - Measured Return Loss of BAPV Antenna .....	77
Figure 7.3 - Measured Gain of BAPV Antenna versus Frequency.....	79
Figure 7.4 - Measured Radiation Pattern of BAPV Antenna.....	80
Figure 7.5 - Signal Through Selected and Un-Selected Series of Microwave Switches ...	82
Figure 7.6 - Isolation Between Switches from Hittite Microwave Data Sheet [4] .....	83
Figure 7.7 - Polarizing Filter.....	85
Figure 7.8 - Polarizing Filter Effect on Signal Transmitted from Source .....	86
Figure 7.9 - Scattered Field of Dielectric Cylinder for 0°-Rotation .....	88
Figure 7.10 - Scattered Field of Dielectric Cylinder for 90°-Rotation .....	89
Figure 7.11 - Scattered Field of Off-Centered Circle 0° Rotation .....	90
Figure 7.12 - Scattered Field of Off-Centered Circle 180° Rotation.....	90
Figure 7.13 - Scattered-Field Plot for Dielectric Square at 45° Rotation .....	91
Figure 7.14 - Scattered-Field Plot for Dielectric Square at 135° Rotation .....	92
Figure 7.15 - Cylinder with Defect .....	93
Figure 7.16 - Scattered Field Plot for Cylinder with Defect at 0°-Rotation .....	94
Figure 7.17 - Scattered Field Plot for Cylinder with Defect at 180°-Rotation .....	95
Figure 7.18 - AbsolutePlot of Scattered Field for Cylinder with Copper Sheet Metal.....	96

Figure 7.19 - Absolute Plot of Scattered Field for Cylinder.....	97
Figure 7.20 - Scattered Field of Cylinder with Water in Defect.....	98
Figure 7.21 - Scattered Field of Cylinder .....	99
Figure 7.22 - Permittivity Versus Percentage Difference of Scattered Fields .....	100
Figure 7.23 - Initial Reconstruction Results of Dielectric Cylinder .....	101
Figure 7.24 - Initial Reconstruction of Off-Centered Cylinder .....	102
Figure 8.1 - Original Image of Square with Electrical Size of $2\lambda$ .....	106
Figure 8.2 - Reconstructed Image with 64 Sensors at $5^\circ$ Projection Increments.....	107
Figure 8.3 - Reconstructed Image with 128 Sensors at $2^\circ$ Projection Increments.....	108
Figure 8.4 - Reconstructed Image with 256 Sensors at $2^\circ$ Projection Increments.....	109

## **Chapter 1 - Introduction**

### **1.1 - Research Background**

Imaging is a method of non-invasively analyzing structures and objects that provides applications in areas of biology and non-destructive evaluation. Tomography is one of these imaging techniques, and uses projections of an object acquired by illuminating this object from different angles using an energy source that is capable of penetration. In common tomographic imaging systems, such as X-Ray or MRI, a source emitting radiation and receivers collecting the radiation are required to rotate around the object that is being imaged, and often require a full 360°-revolution for an image to be reconstructed. This type of imaging is an often-used method in the detection of cancerous tissue. In breast cancer detection, X-Rays have been used for decades, but using this method has several disadvantages, even though its use is very widespread, and successful detection rate for breast cancer reaches up to 90% [1], while cases of false-positives can range from 5-15% of individual cases. The density contrast between healthy and malignant tissues is not large, with maximum contrast achieved at lower energies, around 15keV, which results in longer exposure time and high radiation absorption in the tissue [2]. The objective of this research presented in this proposal is to design and develop a microwave tomographic-imaging system that can be used in bio-medical imaging, as well as structural health monitoring and evaluation of dielectric materials, such as polymer laminates, composite and ceramic structures.

Microwaves are electromagnetic radiation within the range of 30MHz-300GHz. Unlike X-Rays, microwaves diffract whereas X-Rays are absorbed or passed through an object, and therefore this diffraction, which makes straight-ray tomography, used for X-rays, invalid. The wave object interaction at microwave frequencies are governed by wave propagation and

diffraction phenomenon [1], which will be described in Chapter 2. Since the wavelengths at these frequencies are in the range of meters diffraction effects make microwave tomography more complex.

In order to obtain these minimal-angle scans, a different part of this research involves beam steering through a deformable electromagnetic mirror. Doing so is completed through using reflect-array antenna, which are used to steer incident beams based upon voltages applied to varactor diodes placed across the patches of the array. While initial results have shown beam-steering to work for  $\pm 30^\circ$ , the goal is to have over  $120^\circ$  of coverage through the novel idea of beam-steering, which is currently being progressed through comparing different diode and patch combinations. *Figure 1.1* shows one of the layouts used in designing the mirror.

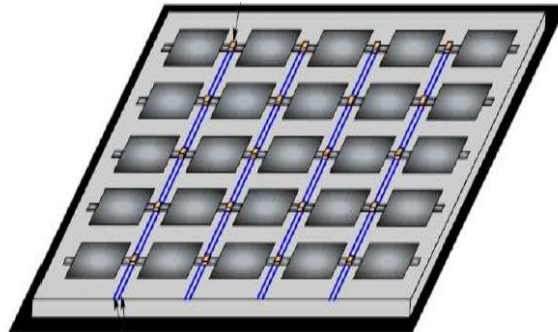


Figure 1.1 - Schematic of Mirror for Microwave Tomography System. For interpretation of the references to color in this and all other figures, the reader is referred to the electronic version of this thesis.

## 1.2 - Objective

The objective of this research is two-fold; the first objective is to create a proto-type imaging antenna array to be used in minimal-scan microwave imaging. To accomplish the goal, Vivaldi antennas, a type of microstrip antenna that is classified as a tapered-slot antenna, or TSA, was chosen, due to their ability to operate over a wide range of frequencies, as well as possessing

low cross-polarization, high gain and compact size, when compared to other microstrip antennas. Secondly, to develop a tomographic reconstruction algorithm that can be used for diffracting sources with limited views and limited scans. *Figure 1.2* shows the system layout.

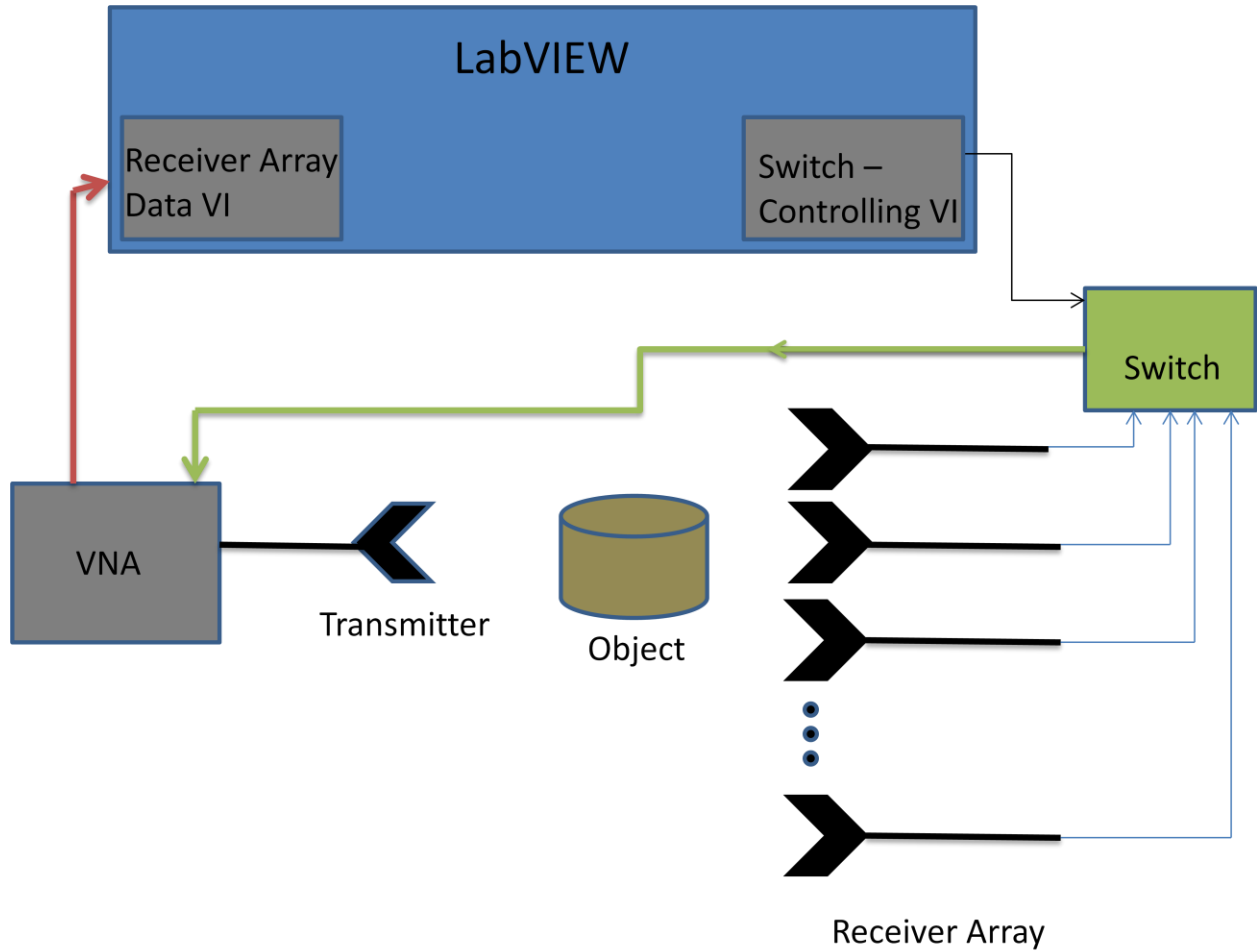


Figure 1.2 - Proposed System Layout

### 1.3 - Organization of Thesis

This thesis has been organized as follow: Chapter 2 starts by first explaining some of the background and imaging methodology used in this research via the Fourier Diffraction Theorem and Minimal-Scan Filtered Back-Propagation. Then, a brief overview and theory of microstrip antennas is presented in Chapter 3, followed by some simulation results for several different

types of antennas. In Chapter 5, a simulation study on the microwave switches used in this research is presented, followed by the measured results obtained from the switches. After the components of the microwave tomography system have been tested individually in Chapter 6, Chapter 7 shows the full system integration results, and how the automated antenna array performs as part of the whole system. Finally, Chapter 8 concludes this thesis with on-going and future work for this research.

WORKS CITED

## WORKS CITED

- [1] K.Arunachalam (2006), "*Investigation of a Deformable Mirror Microwave Imaging and Therapy Technique for Breast Cancer.*" Doctoral Thesis, Michigan State University, USA.
- [2] Paladhi, Pavel, Tayebi, Amin. "Design and Development of a Mirror-Based Alternative Microwave Tomography System." 2013.
- [3] D. G. Berry et al, " *The Reflectarray Antenna*", IEEE Transaction on Antennas and Propagation, 1963.

## Chapter 2 - Theory

### 2.1 - Introduction

Imaging can be accomplished through various techniques, with one of them being tomography; tomography can be thought of as combining cross-sections of projected data into the final result of an image, or tomogram. Many conventional imaging methods use X-Rays as a source for imaging, which do not scatter, also called non-diffracting, when incident with an object, but rather are either passed through or are absorbed by the object. For reconstruction, it is a measurement of the absorption by the tissue or object, and for non-diffracting objects, the Fourier Slice Theorem can be implemented to reconstruct the object being imaged; the Fourier Slice Theorem can be derived by, "...taking the one-dimensional Fourier Transform of a parallel projection, and noting that it is equal to a slice of the two-dimensional Fourier Transform of the original object." [1]. From *Figure 2.1* below, the projection data is transformed to the frequency domain via the Fourier Transform, where the original object can then be reconstructed from line integrals via the inverse Fourier Transform, as the values of the original object lie along the straight line in the Fourier-space.

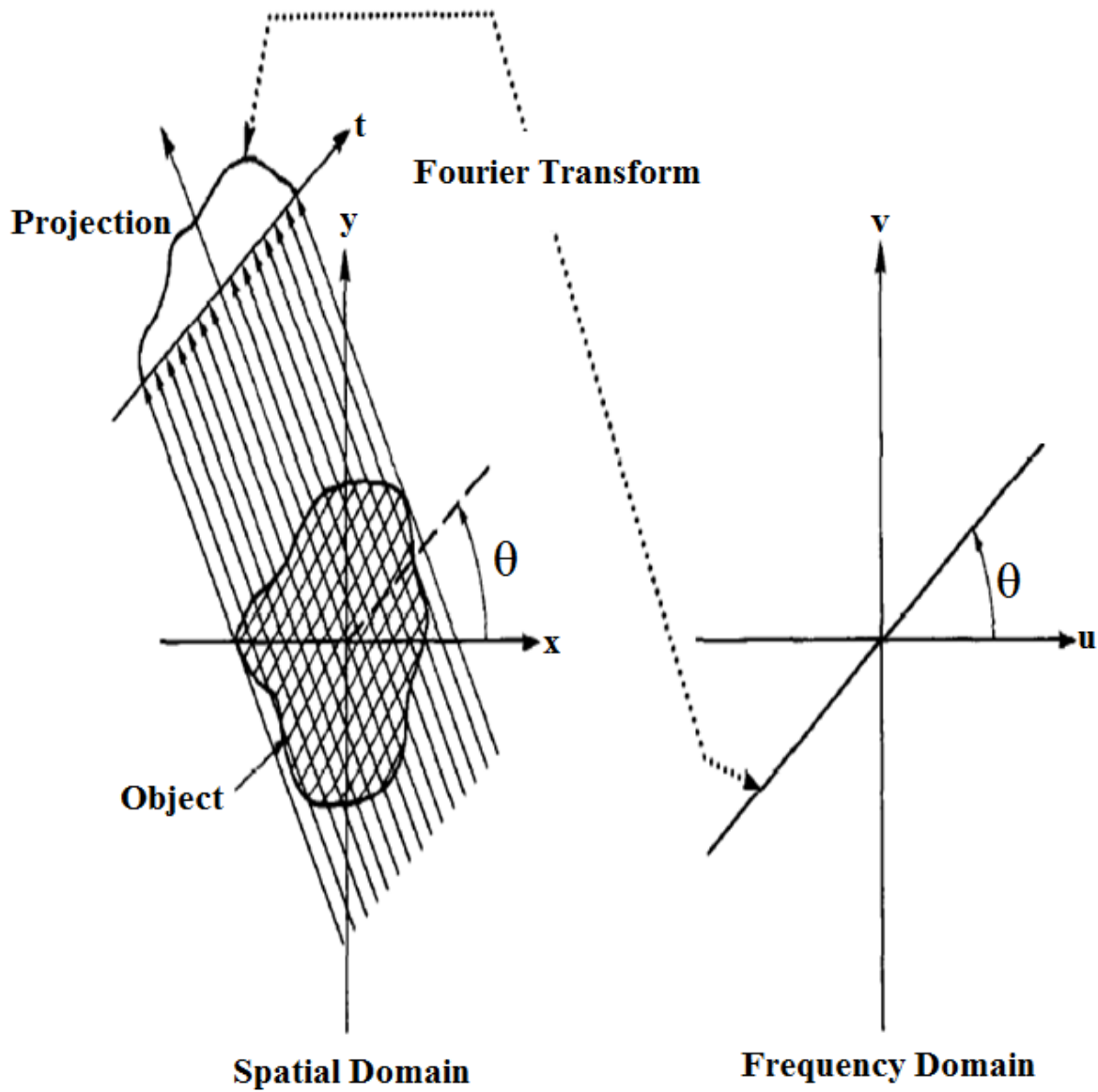


Figure 2.1 - Graphical Representation of the Fourier Slice Theorem [1]

One of the negatives with using X-Rays, however, is that they are ionizing radiation, which, after prolonged exposure, can cause cancer in a living patient. A new, safer, method using micro-waves has become more-prevalent over recent years because the radiation is non-

ionizing, as well as providing much larger contrasts between healthy and damaged tissue, and therefore offering a higher detection rate. Compared to X-Rays, however, microwaves diffract when they are incident with an object, and, therefore, the same techniques of straight-ray tomography based on the Fourier Slice Theorem cannot be used; in order to account for the scattering, the Fourier Diffraction Theorem must be employed for image reconstruction, and will be introduced in the following section.

## 2.2 - Fourier Diffraction Theorem

As mentioned above, for diffracting objects, that is, where the inhomogeneities are less than approximately one wavelength in size [2], imaging that uses microwaves as the incident source cannot use line integrals to reconstruct the object in question, but, rather, must rely on plane-wave propagation properties to determine the reconstructed image. This thesis will not delve into too much of the mathematics behind the Fourier Diffraction Theorem; for a full explanation, the reader should refer to [2], but a brief description will be provided here. The homogenous wave equation, shown in Equation (1) below, describes the behavior of an electromagnetic wave that travels through a medium.

$$\nabla^2 u(\vec{r}, t) - \frac{1}{c^2} \frac{\nabla^2}{dt^2} u(\vec{r}, t) = 0 \quad (1)$$

Equation (1) can be simplified [2] to the following:

$$[\nabla^2 + k^2(\vec{r})] u(\vec{r}, t) = 0 \quad (2)$$

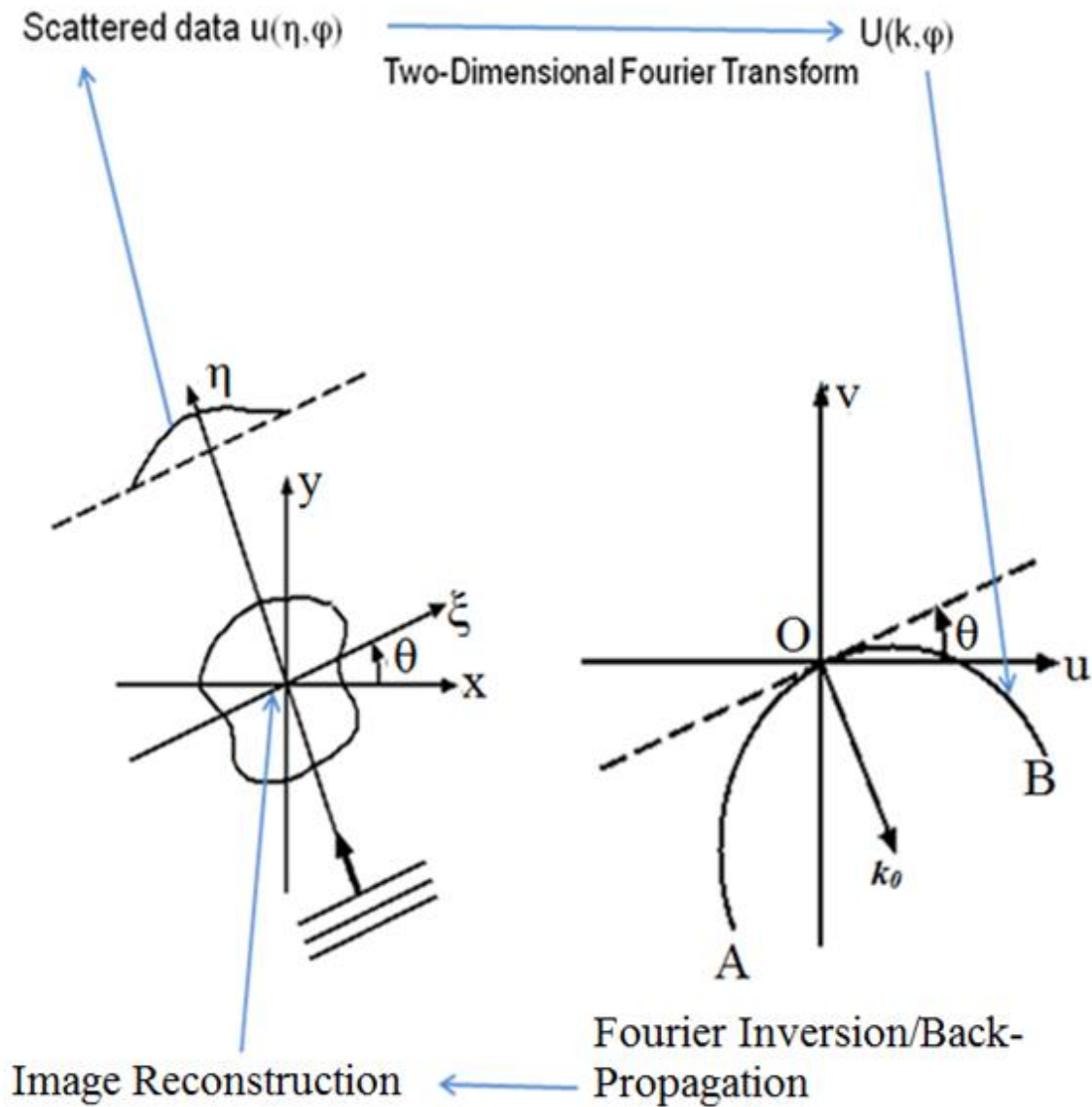


Figure 2.2 - Graphical Representation of the Fourier Diffraction Theorem [2]

which is satisfied for both homogenous or inhomogenous cases if the wavenumber,  $k$ , is assumed to be strictly real by ignoring de-polarization effects of the medium [3].

The reconstruction process reconstructs the complex permittivity of a weakly-scattering object, as experimental data will show in subsequent chapters, and a circular window ranging from  $-2k_0$  to  $2k_0$  is used as a low-pass filter, and anything outside of this window is regarded as

an evanescent wave, which is an electromagnetic wave that decays exponentially, instead of sinusoidally [4], and is filtered out from the reconstruction process. The circular window is constructed from the arcs shown in *Figure 2.2* which rotate around the entire Fourier-plane for  $360^\circ$  of coverage, as seen in *Figure 2.3*. As seen in *Figures 2.1* and *2.2*, the main difference is that in the Fourier Slice Theorem, the data in the Fourier-space is collected along straight lines, whereas in the Fourier Diffraction Theorem, the data is along a semi-circle in the Fourier-space. The coverage of the Fourier-space is what creates the low-pass filter mentioned above, and depicted in the following figures.

Noted by Pan, et. al. in 1999, the Fourier space can also be covered by applying what are called 'weight filters,' which use the data redundancy of the coverage in the Fourier space to completely reconstruct the object with  $270^\circ$  of coverage with the same fidelity as  $360^\circ$  of coverage. Note the comparisons between *Figure 2.3* and *Figure 2.4*, that the same amount of Fourier space is covered by the arcs generated by the Fourier Diffraction Theorem.

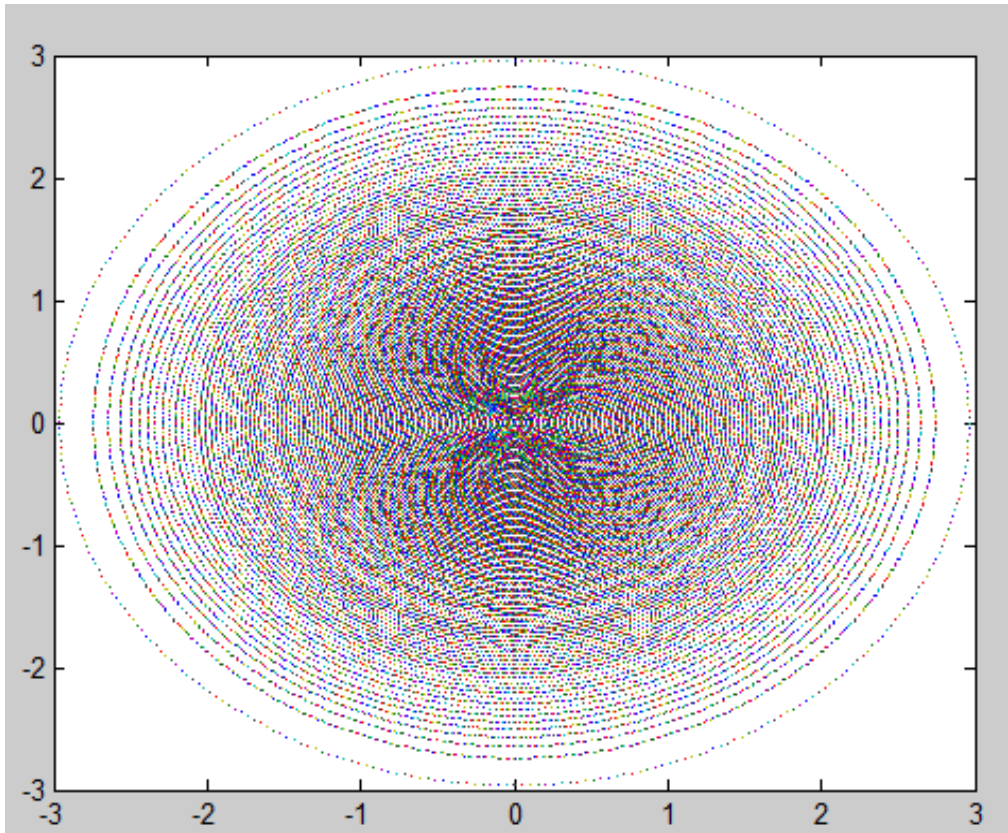


Figure 2.3 - 360° Coverage of Fourier Space

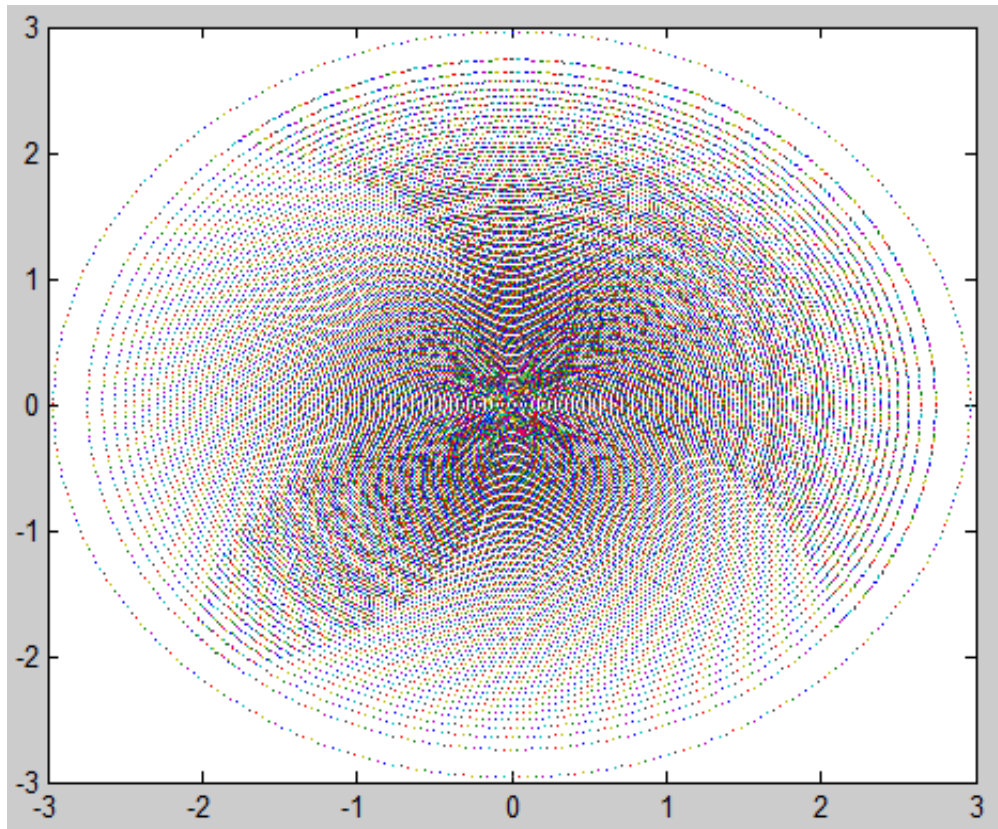


Figure 2.4 - 270° Coverage of Fourier Space

Based upon the double-coverage in the Fourier space, this is the basis for the coding that has been developed that allows for minimal angle scans to be taken and reconstruct the object in question; this process has been given the name minimal-scan filtered back-propagation, or MSFBPP.

Once the scattered fields have been generated, that data, along with the locations of the sensors along each arc point in the Fourier space for each angle, are passed through the MSFBPP portion of the code. For full, 360° coverage of an object, the standard Filtered Back-Propagation equation can be used:

$$\begin{aligned}
& a(r, \theta) \\
&= \frac{1}{2} \int_{\phi=0}^{2\pi} \int_{v_m=-v_0}^{v_0} \frac{v_0}{v'} |v_m| M(v_m, \phi) \cdot e^{[j2\pi v_m \cos(\phi-\alpha-\theta)]} dv_m d\phi \\
& (3)
\end{aligned}$$

Where  $v_m$  represents the wavenumber, and  $M(v_m, \phi)$  represents the scattered data. For limited-angle scans, however, the Minimal-Scan, Filtered Back-Propagation algorithm is:

$$\begin{aligned}
& a^w(r, \theta) \\
&= \frac{1}{2} \int_{\phi=0}^{3\pi/2} \int_{v_m=-v_0}^{v_0} \frac{v_0}{v'} |v_m| M'(v_m, \phi) \cdot e^{[j2\pi v_m \cos(\phi-\alpha-\theta)]} dv_m d\phi \\
& (4)
\end{aligned}$$

with  $M'(v_m, \phi)$  representing the weighted data set, which is defined as:

$$M'(v_m, \phi) = w(v_m, \phi) M(v_m, \phi) \quad (5)$$

and, one set of weight filters,  $w(v_m, \phi)$ , is defined as:

$$w(v_m, \phi) = \begin{cases} \sin^2 \left[ \frac{\pi}{4} \cdot \frac{\phi}{\pi/4 + \alpha} \right], & 0 \leq \phi \leq \pi/2 + 2\alpha \\ 1, & \pi/2 + 2\alpha \leq \phi \leq \pi + 2\alpha \\ \sin^2 \left[ \frac{\pi}{4} \cdot \frac{3\pi/2 - \phi}{\pi/4 - \alpha} \right], & \pi + 2\alpha \leq \phi \leq 3\pi/2 \\ 0, & 3\pi/2 \leq \phi \leq 2\pi \end{cases} \quad (6)$$

Currently, the weight filters are not being used on the experimental data, due to the effects of noise on these filters being unknown. For the simulated data, as will be shown later in this chapter, the weight filters do provide better reconstruction results for limited-angle scans down to near  $180^\circ$ . For a full explanation of the weight filters, the reader should refer to [5], but the following images show a glimpse into the affects of these filters.

### **2.3 - MSFBPP Implementation Process**

While the main goal of this research and thesis was in designing the receiver array, much time was also spent on developing, testing, de-bugging and evaluating the minimal-scan filtered back-propagation code, which is the basis for how the images are reconstructed; this section will cover some of, but not all, the aspects of the coding process. The method of MSFBB, while relatively new, has, to our knowledge, not been implemented with experimental data, but only run with simulated data.

The coding process begins by generating scattered data, and, based off of the Born Approximation and Fourier Diffraction Theorem [2], this scattered data represents theoretical data under ideal conditions.

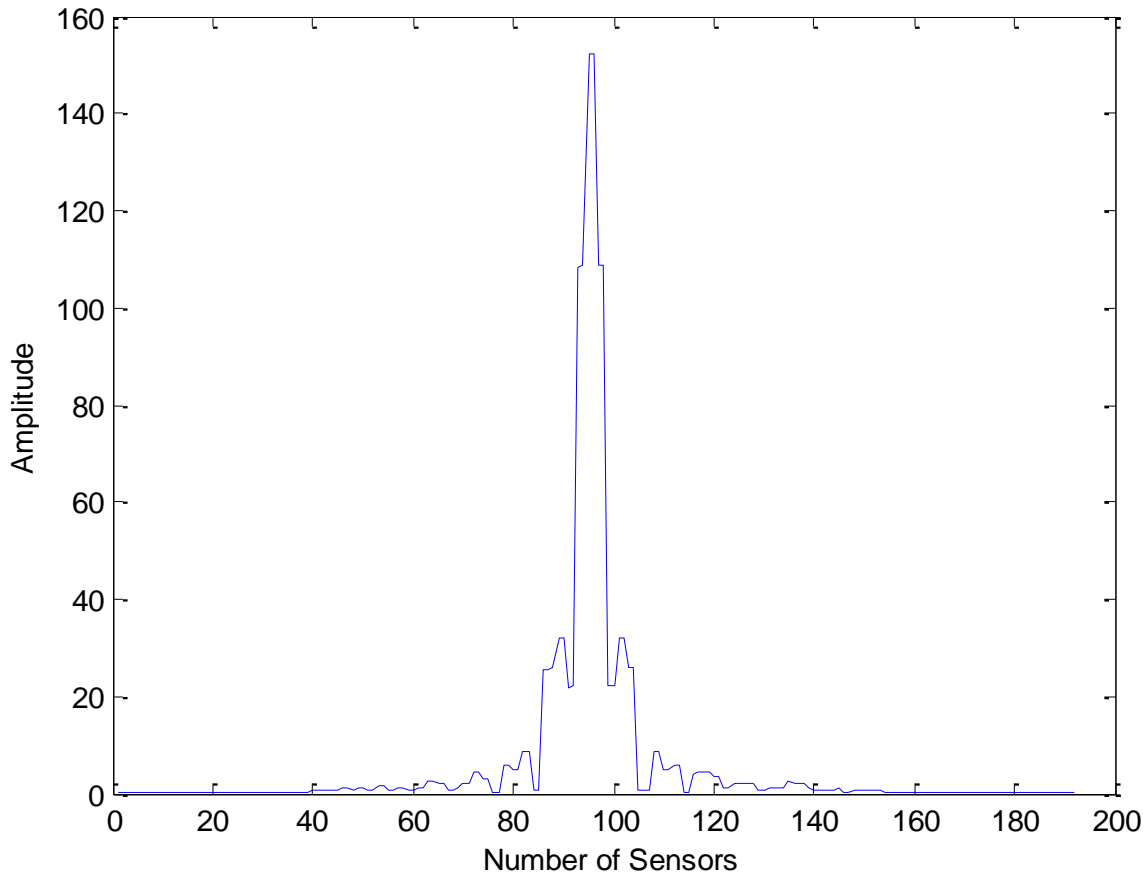


Figure 2.5 - Simulated Scattered Data

The scattered data has been generated for simple objects, such as circles and squares, as well as more recently, object such as the Shepp-Logan phantom. Once a seed image is generated, typically 64x64 pixels, it is then zero-padded to 512x512 pixels, or larger, so that there is more available data in the Fourier space; without this extra padding, many of the smaller details, such as edges or un-symmetrical components, are not detected in the reconstruction process. From this point, the two-dimensional Fourier Transform is taken, and once the data is in the Fourier-space, the method outlined above in *Figure 2.2* of passing the arc through the u-v plane is completed via the Fourier Diffraction Theorem.

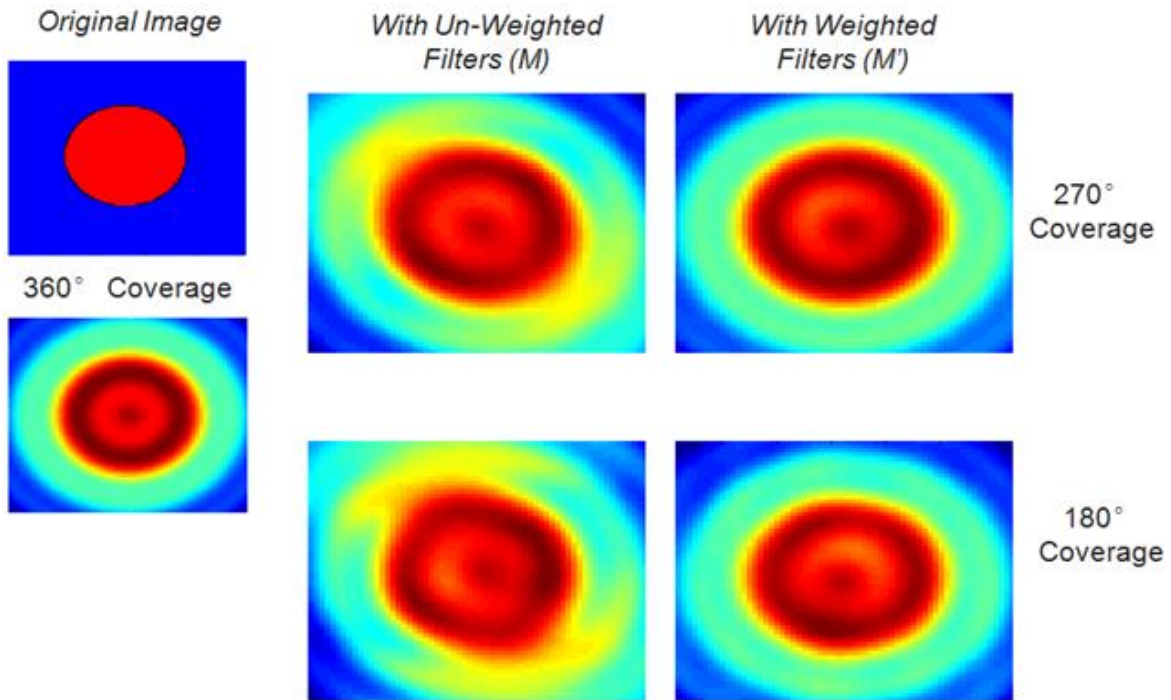


Figure 2.6 - Effect of Weight Filters on Reconstruction of Simple Object

Clearly, from this figures, the initial set of weight filters developed in [5] allow for better reconstruction results than without using the filters. For more-complex objects, the following results have been obtained through the Filtered Back-Propagation and Minimal-Scan Filtered Back-Propagation algorithms for one large and small circle with a dielectric of 1.01, and sizes of  $2\lambda$  and  $1.5\lambda$ , respectively.

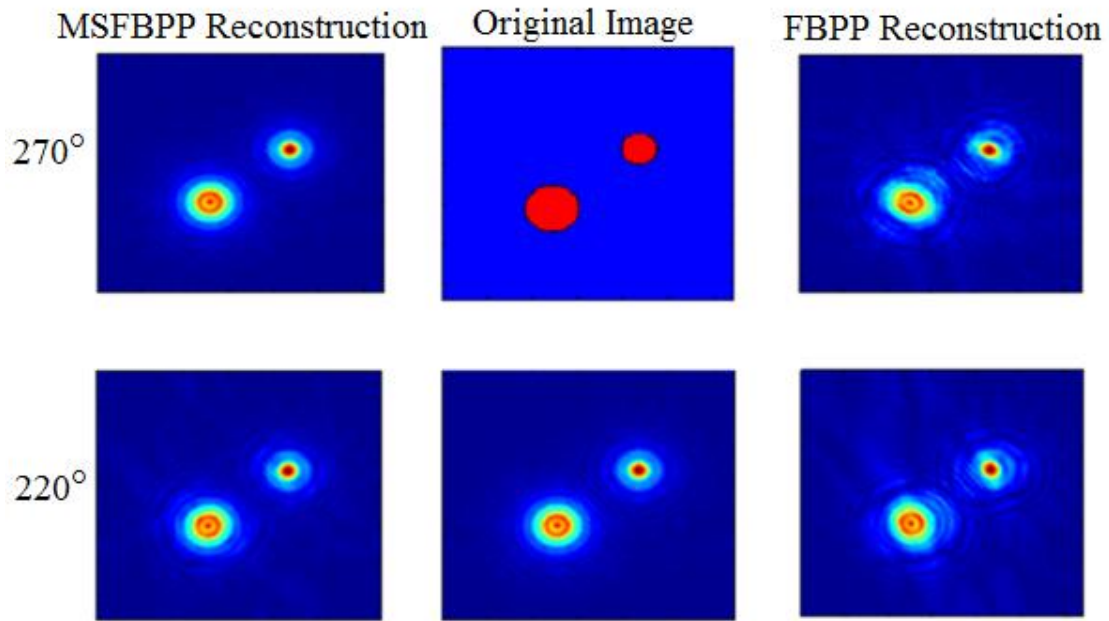


Figure 2.7 - Weighted and Un-Weighted Reconstruction Results for MATLAB Code

These reconstruction results clearly show the effect of the weighted-filters on the reconstruction process for simulated data, and this effect for experimental data is currently being studied, and will be discussed in the *Conclusions and Future Work* chapter of this thesis.

Another aspect of the code that has recently been added is that of Total Variation minimization, which enforces specific criterion on the reconstructed image, and is able to remove some of the ripples, as evident from the following images:

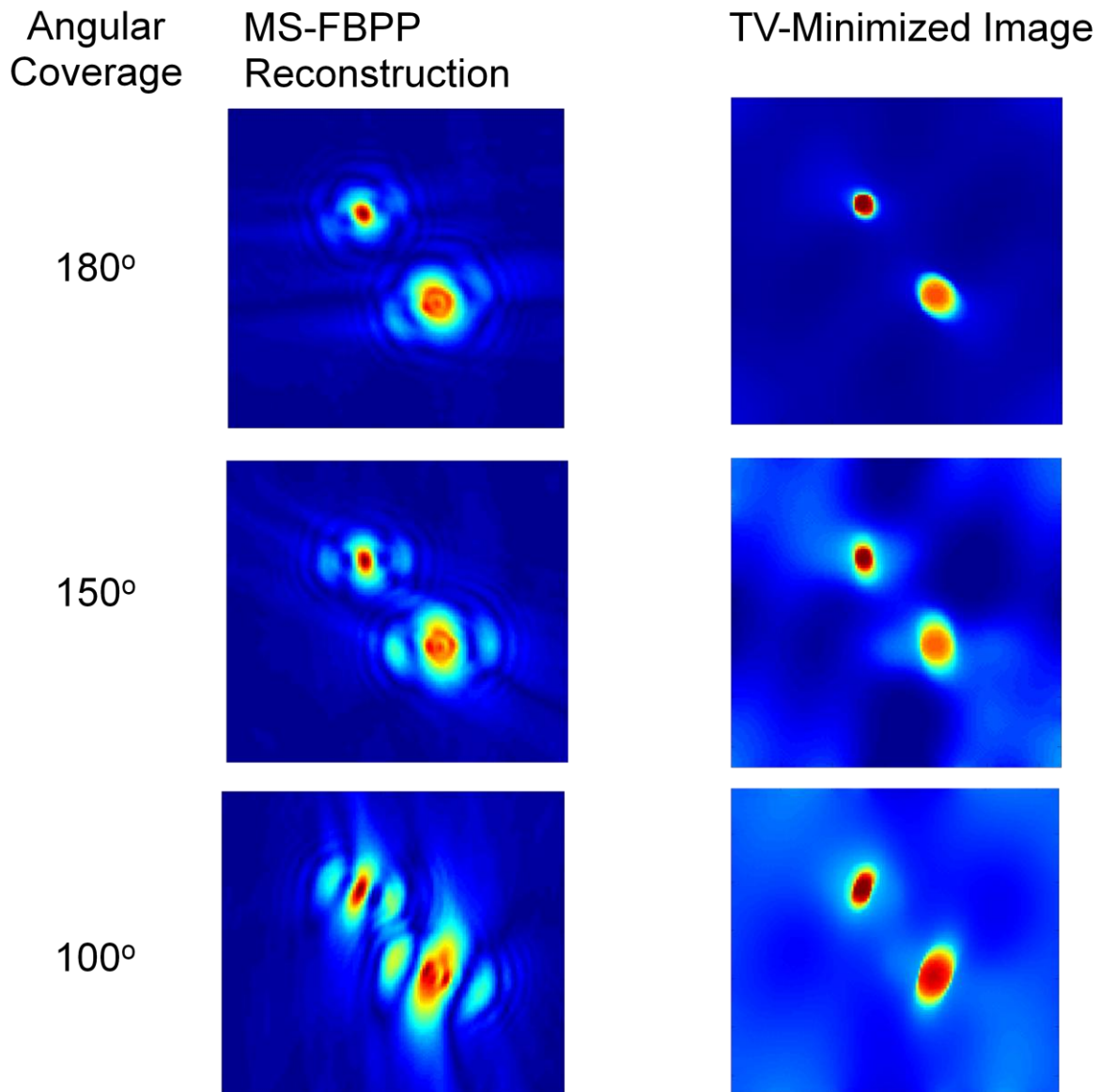


Figure 2.8 - Total Variation Regularization Applied to MSFBPP Images for Limited-Angle Views

Evident from these figures, it is clear that the method of Total Variation can reduce some of the noise that was added into the reconstruction process, and while this is a common technique in many image processing applications, the full impact has not been studied in-depth for diffraction tomography, let alone for experimental data. For a more-complete definition of the

method of Total Variation, the reader should refer to [6]. Both weight filters and total variation have been shown to work well with simulation data, but more studies need to be conducted to see the effect upon experimental data, and how these powerful post-processing applications can be used in reconstructed diffracted scattered fields.

WORKS CITED

## WORKS CITED

- [1] Kak, C. "Algorithms for Reconstruction with Non-Diffracting Sources." *Principles of Computerized Tomographic Imaging*, IEEE Press, 1987, Chapter 2.
- [2] Kak, C. "Tomographic Imaging with Diffracting Sources." *Principles of Computerized Tomographic Imaging*, IEEE Press, 1987, Chapter 3.
- [3] Kak, C. "The Fourier Diffraction Theorem." *Principles of Computerized Tomographic Imaging*, IEEE Press, 1987, Chapter 6.
- [4] Nyquist, Dennis. "ECE 835: Advanced Electromagnetic Fields and Waves Course Notes." Michigan State University. 2001
- [5] Pan & Anastasio, "Minimal-Scan Filtered Backpropagation Algorithms for Diffraction Tomography", *J.Opt.Soc.Am.A*, Vol.16,No.12,July2008.
- [6] Pan, X. and Sidky, E. "Image Reconstruction in Circular Cone-Beam Computed Tomography by Constrained, Total-Variation Minimization." 2008. *Phys. Med. Biol.* **53** 4777.

## Chapter 3 - Microstrip Antennas

### 3.1 - Introduction

In antenna design, the impedance of the antenna is designed to match that of the surrounding medium for maximum power transfer; for the case of free-space, the intrinsic impedance of air is approximately  $377\Omega$ , and proper impedance matching allows for the antenna to receive or transmit electromagnetic energy. When considering the design criteria for the antennas, many considerations must be taken into selecting the proper design that will not only allow for operation in the desired frequency range, but also including the important aspects of gain, beamwidth, polarization and radiation pattern, as well as the physical size of the antenna. Microstrip antennas were initially developed in the 1950's, but successful implementation was not fully achieved until the 1970's, which came about due to the more-recent availability of higher-quality substrates, modeling and fabrication. Defined as:

*"A conducting patch of any planar or non-planar geometry on one side of a dielectric substrate with a ground plane on the other."* [1]

Microstrip antennas are commonly used in areas such ranging from cellular and satellite communications to imaging and radar applications. This chapter will outline some of the theory, as well as different approaches taken in designing the receiver array using microstrip radiators. [2]

### 3.2 - Patch Antennas

Patch antennas have, generally, simple feeding techniques, are easy to fabricate and typically have wide beam-widths. The resonant frequency of a basic patch antenna can be determined, roughly, from  $\lambda/2$  for a rectangular patch, although the fringing fields actually make

the electrical size slightly larger, so, for design purposes, the length and width can be estimated as slightly less than half of a wavelength [1].

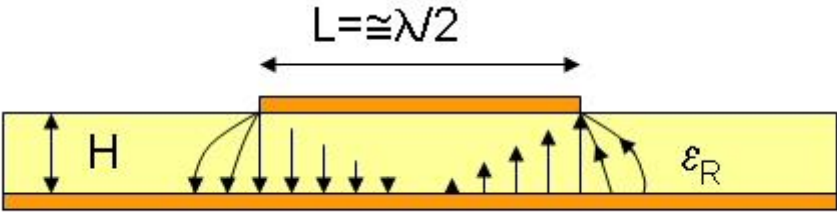


Figure 3.1 - Microstrip Antenna Fringing and Radiating Fields [3]

Charge build-up occurs from a distribution on the top and bottom sides of the patch, as well as the ground surface, and, from these charge densities, radiation occurs from the fringing fields at the end of the patch, where the magnitude of the current is greatest.

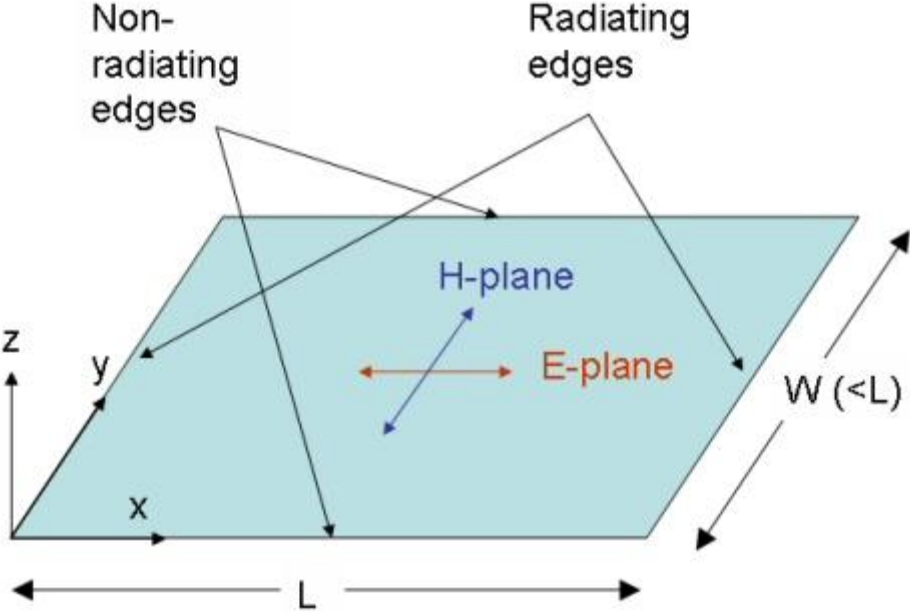


Figure 3.2 - Radiating Edges of Patch Antenna [3]

Likewise, for other patch antennas, discontinuities, open circuits and sharp corners also account for radiation, whether intended or unintended. In their simplest construction, a microstrip patch antenna consists of a radiating patch, made out of a conducting material, on one side of a dielectric substrate, and a ground plane on the other side of the substrate. When designing antennas, often the electrical size is a large factor that requires a good amount of attention; for proper antenna operation, a thick dielectric substrate having a low dielectric constant is desirable since this provides better efficiency, larger bandwidth and better radiation. However, such a configuration leads to a larger antenna size. In order to design a compact microstrip patch antenna, higher dielectric constants must be used which are less-efficient and result in narrower bandwidth, and, therefore a compromise must be reached between the electrical dimensions and the performance of the antenna.

While there are many advantages of patch antennas, such as their low cost of fabrication and ability to be integrated with RF circuitry, there are also many disadvantages, such as their low gain and bandwidth [2], which are two traits necessary for the imaging array. After these realizations, as well as the simulation results in the following chapter, the research went in a different direction to try and find antennas that fit the required criteria.

### **3.3 - Series and Corporate-Fed Antennas**

The next step in the research was investing what are called series and corporate-fed antenna arrays; they are combinations of patch antennas, but, compared to simple patch antennas, the gain and bandwidth is higher, and, from the previous section, these were two of the more-important antenna design factors that needed to be improved upon from previous designs.

Series-fed antennas are simply a connection of patch antennas, spaced  $\lambda/2$  apart, and fed by quarter-wavelength-long lines, and, because of this spacing, the radiation adds in-phase, allowing for higher a larger gain, due to the spacing of the patches. And, instead of using the same size of patches for, say, a 4x1 array, different sizes can be used, which also increase the bandwidth of the antenna, as the different sizes provide a slightly different resonant frequency [3].

Next, a corporate-fed array was developed, which basically acts as a power-divider for the array, splitting the power from the source evenly between the radiating patches (generally a power of two.) This setup is ideal for imaging and scanning arrays, as the amplitude and phase of the feed can be more-easily controlled [3]. To evenly divide the power from a 50 $\Omega$ -source, stepped-impedance lines are used, and the patches are then fed in-phase from the source. This setup lowers the presence of side-lobes, and generates a narrower, more-focused beamwidth.

Combining these two methods (see the subsequent chapter for pictures and results) allows for both a higher gain, as well as a larger bandwidth and narrow main beam, which are the parameters that were sought that were lacking in simple patch antenna design. However, two draw-backs to this approach are, one, for the stepped-impedance of the corporate feed, the impedance lines are matched to 100 $\Omega$ , which, for even frequencies in the 2-6GHz range, can become extremely narrow, around the neighborhood of less than 0.5mm, which can be difficult to accurately fabricate. On top of this, the size of these antennas, because of the nature of the corporate feed, are large in size, roughly two feet by one foot, for a 4x2 array, and, for the purposes of imaging, the scattered data that we are attempting to measure, will not be received by all of the patches on an individual antenna, but, rather, only one or two, at the most. Because of these draw-backs of fabrication tolerance and size of the overall antenna, this corporate and

series-fed design could not be used in this research, even though the parameters of a wider bandwidth and narrower beamwidth with high gain were present with this current antenna design.

### 3.4 - Microstrip Log-Periodic Antenna

Before delving into the main portion of this chapter, a brief note will be made on log-periodic microstrip antennas, pictured below in *Figure 3.3*.

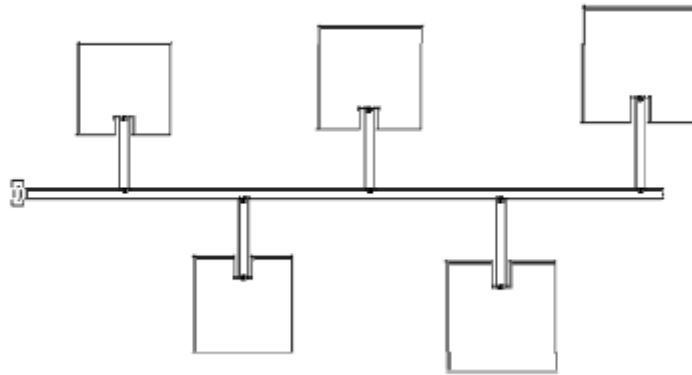


Figure 3.3 - Microstrip Log-Periodic Antenna with Inset-Fed Patches [4]

Similar to a log-periodic antenna, such as the Yagi, the microstrip version of the log-periodic consists of increasingly-larger inset-fed patches that are spaced roughly  $\lambda/2$  apart. These antennas provide large bandwidth and moderate gain, and were nearly considered for using in the receiver design, but the main lobe was too large, as well as size being an issue, but the bandwidth of these antennas was basically a summation of the bandwidth's of all of the elements connected to the main feed line of the antenna. And, as the simulations in the next chapter will show, the return loss was very good, when compared to the other types of antennas

researched up to that point, but, again, the gain and radiation pattern fell short of what was required for this receiver array.

### **3.5 - Tapered-Slot Antennas**

Several years after the successful implementation of the first microstrip antennas, Peter Gibson, in succession with several others, proposed the first idea of a tapered-slot antenna in 1978 [5]. Known as an end-fire radiator, electromagnetic waves propagate through the surface of the antenna substrate with a phase velocity less than the speed of light; antennas with phase velocity greater than the speed of light are referred to as leaky wave antennas, which do not experience end-fire radiation [6], i.e. patch antennas. Electromagnetic waves move along the increasingly-separated metallization until the separation is such that the wave detaches from the antenna structure and radiates into free space from the end of the substrate.

The E-plane of the antenna is the plane containing the electric field vectors of the radiated electromagnetic waves. For most tapered-slot antennas, as well as those discussed in this thesis, this is parallel to the substrate, with the electric field attached to the horizontally separated tapers prior to being radiated outwards [7]. The H-plane, which contains the magnetic component of the electromagnetic wave that is radiated, runs perpendicular to the substrate, which is also perpendicular to the radiated electric field [8]; hence, the tapered-slot antenna operates in the  $TM_{01}$  mode.

Many different types of tapered-slot antennas exist, and *Figure 3.1* shows several of the commonly-used designs:

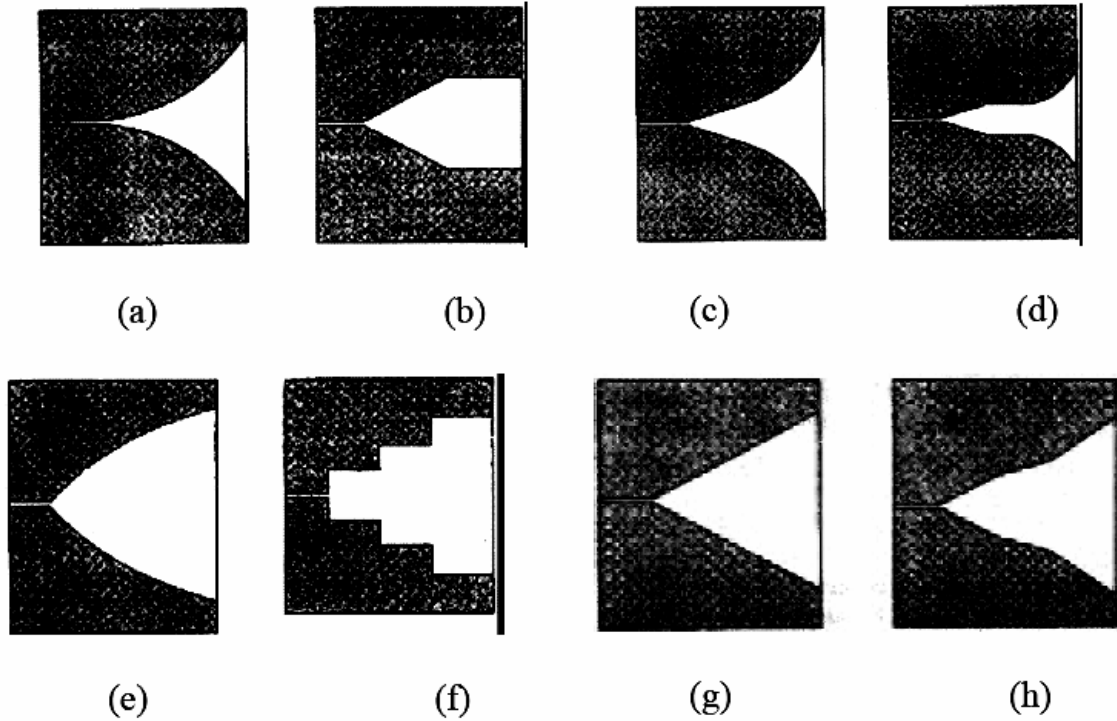


Figure 3.4 - TSA Types: (a) Vivaldi, (b) Linear-Constant, (c) Tangent, (d) Vivaldi-Constant), (e) Parabolic, (f) Stepped-Constant, Linear (g), Broken-Linear (h) [9]

One interesting note about the different flare profiles of these antennas is that the rate of the tapered-slot controls the input impedance; this was a key point of interest in this research, and, as will be seen in subsequent chapters, was a main contributing factor in selecting a type of Vivaldi antenna for implementation in the research.

Outside of the input impedance matching, there were several other benefits of the tapered-slot antennas, such as their larger bandwidth when compared to other microstrip antennas, as well as the tolerance in fabrication, and how this affects the performance of the antenna; when compared to, say, a patch antenna, a mis-calculation of 1mm on the dimension of the patch can greatly alter the radiation pattern, resonant frequency and input impedance, but, which tapered-slot antennas, dimensions may be altered by several millimeters, and the response of the antennas will remain roughly the same. This was also another key factor, as this research

required many antennas to be fabricated, and if a slight error was present, we would need to be assured that the negative impact would be minimal.

For feeding tapered-slot antennas, there are several different methods, with one of the more-common options being to use a microstrip line that is terminated  $\lambda/4$  away from the beginning of the slot as an open circuit, which causes the radiation, along with the short-circuit of the flare, to radiate to the right, as shown in *Figure 3.5* below.

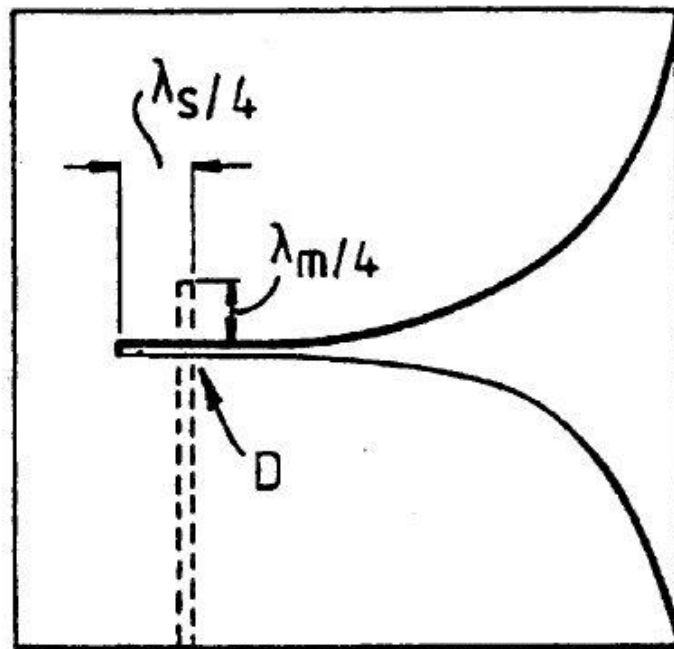


Figure 3.5 - Slot-line Radiation for Vivaldi Antenna [6]

One down-side to using this method, however, is that while impedance matching is easier, the bandwidth of the antenna is lowered; because of this issue, the quarter-wave stub was introduced, which allows for efficient power to be radiated from the antenna without a loss of bandwidth. *Figure 3.6* shows one of the possible methods for the stub, as well as the following chapter, which shows the simulation results for a Vivaldi antenna with this type of feed.

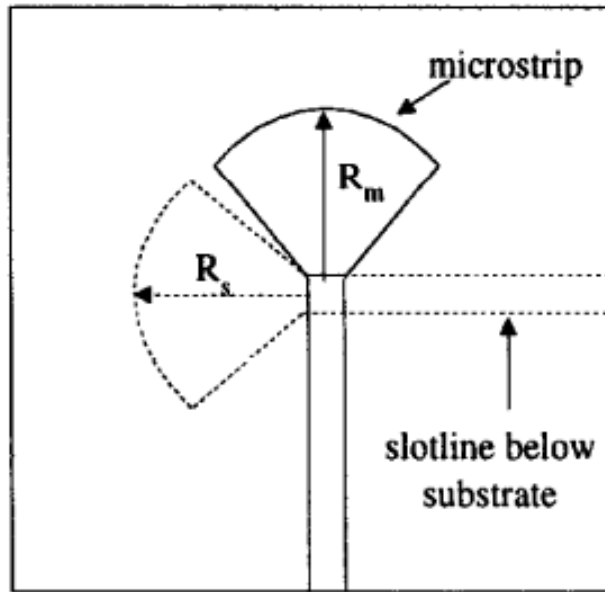


Figure 3.6 - Radial Stub for Feeding Vivaldi Antenna [11]

However, with the traditional Vivaldi antennas, one of the major drawbacks, outside of creating a impedance-matched stub, can be their size. While the simulated and measured return loss were what was required for the research, the size of these antennas was a hindrance, especially in an imaging array, where many antennas may need to be used; this restriction on size led to looking into a new design of the Vivaldi antenna called the anti-podal and balanced, anti-podal Vivaldi antenna.

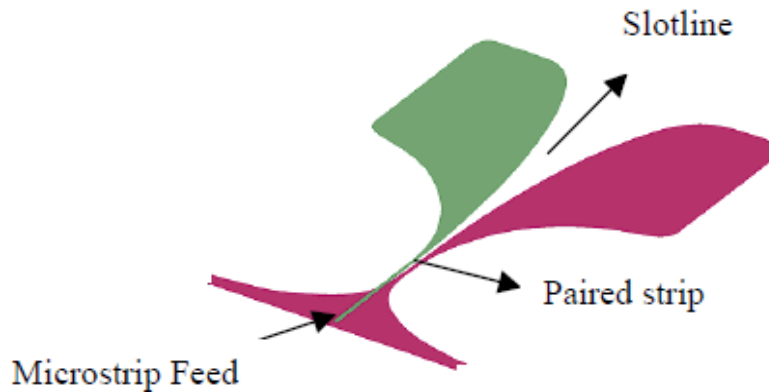


Figure 3.7 - Anti-Podal Vivaldi Antenna [11]

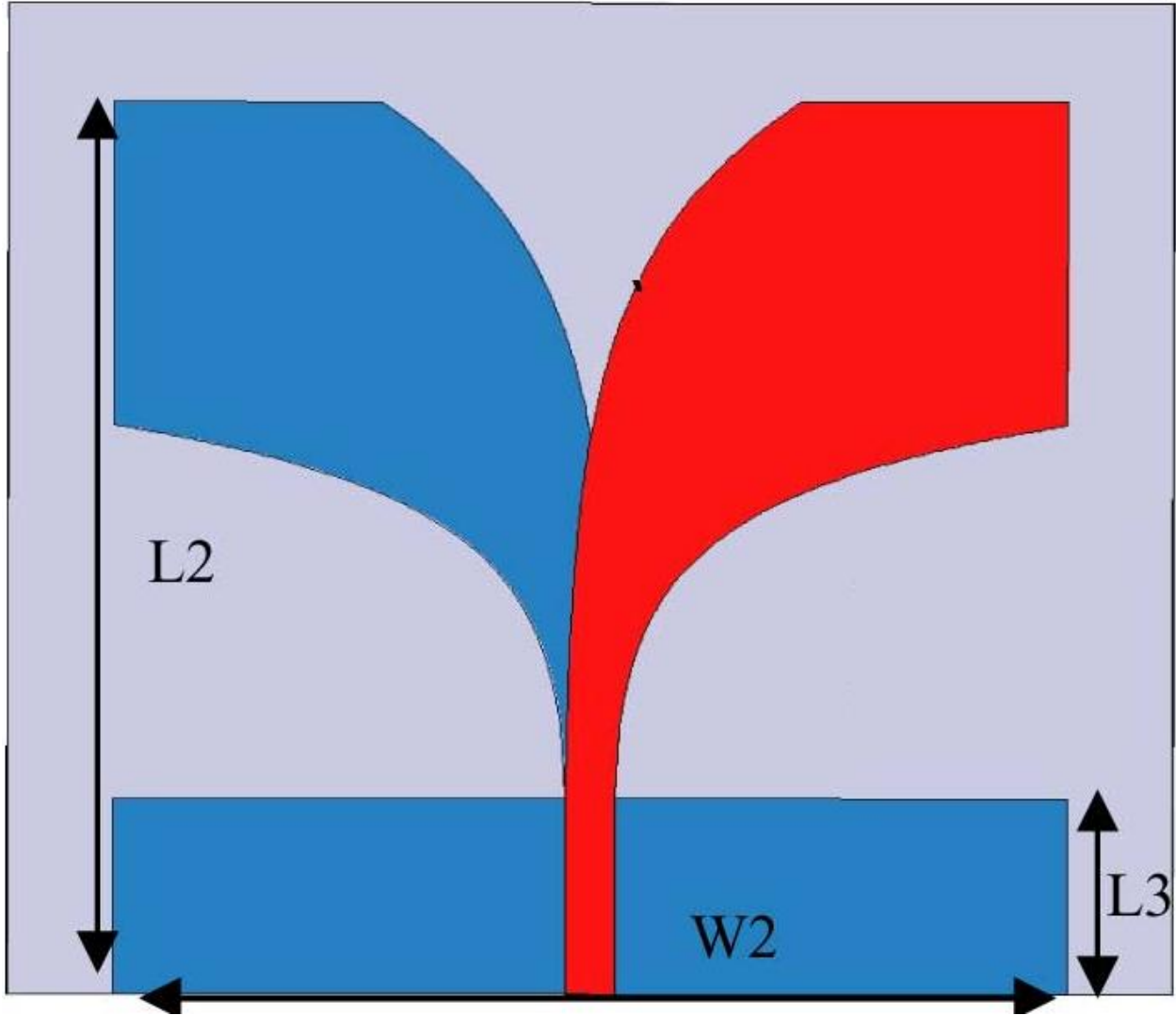


Figure 3.8 - Balanced, Anti-Podal Vivaldi Antenna [11]

The main advantages of both of the designed shown above is that they are smaller in size, and also have a slightly better bandwidth, in theory, than the traditional Vivaldi antenna. In *Figure 3.7*, the anti-podal Vivaldi is printed on one side, and both patches of metalization share the same feed line; this causes high levels of cross-polarization, so, to remove this, Langley in [12] proposed the balanced, anti-podal Vivaldi antenna, show in *Figure 3.8*, which consists of two layers of metalization, where the top yellow layer is connected to the feed of the SMA, and

the bottom, brown, layer is connected to the ground of the SMA connector. Doing so balances the electric field produced from the radiation [12].

The narrow microstrip feed on the top layer, matched to a  $50\Omega$  SMA connector, is able to provide a constant input impedance over a 3:1 frequency range [2], which is unlike most other antennas, as typically the feed length and width are very frequency-dependent. This factor, along with the ratio of the length of the antenna to the wavelength, provides the basis for the wide-band nature of the balanced, anti-podal Vivaldi antenna.

This chapter was intended to serve as a background into several types of microstrip antennas, and the following chapter will present simulation results from the different types of antennas discussed in this chapter, and show that the balanced, anti-podal Vivaldi antenna is very well-suited for use in a microwave imaging array.

WORKS CITED

## WORKS CITED

- [1] James, J.R., P.S. Hall, C. Wood. "*Microstrip Antennas: Theory and Design.*" Peter Peregrinus, London, UK. 1981.
- [2] Garg, Ramesh, Bhartia, Prakash, Bahl, Inder and Ittipiboon, Apisaket. "*Microstrip Antenna Design Handbook.*" Artech House, 2001.
- [3] Muhammad Mahfuzul Alam, Md. Mustafizur Rahman Sonchoy, and Md. Osman Goni. "Design and Performance Analysis of Microstrip Antenna Array." Department of Electronics and Communication Engineering, Khulna University of Engineering and Technology, Bangladesh. 2009.
- [4] Vibha Rani Gupta, Susanta Kumar Sahoo and Nisha Gupta. "*Design of Compact Microstrip Patch Array for Wide-Band Communication.*" Department of Electronics and Communication Engineering, Birla Institute of Technology.
- [5] "Microstrip Patch Antennas." Microwaves101.com  
<[http://www.microwaves101.com/encyclopedia/antenna\\_ustrip.cfm](http://www.microwaves101.com/encyclopedia/antenna_ustrip.cfm)> Last Accessed August 2013.
- [6] "Vivaldi Antenna." Microwaves101.com  
<<http://www.microwaves101.com/encyclopedia/vivaldi.cfm>> Last Accessed August 2013.
- [7] K.S. Yngvesson, T.L. Korzeniowski, Y.S. Kim, E.L. Kollberg, J.F. Johansson, "The Tapered Slot Antenna – A New Integrated Element for Millimeter Wave Applications," *IEEE Trans. Microwave Theory Tech*, vol. 37, Feb. 1989.
- [8] C. A. Balanis, "*Antenna Theory: Analysis and Design.*" Wiley Publishers, 2005.
- [9] Wood, Ian. "Linear Tapered Slot Antenna for Imaging Arrays." Master's Thesis, University of Victoria. 2005.
- [10] K.F. Lee, W. Chen. "*Advances in Microstrip and Printed Antennas.*" New York: John Wiley and Sons, 1997.
- [11] Rajaraman, Raviprakash. "*Design of a Wideband Vivaldi Antenna Array for the Snow Radar.*" Master's Thesis. Department of Electrical Engineering and Computer Science, University of Kansas.
- [12] Langley et al, "Novel ultrawide-bandwidth Vivaldi antenna with low crosspolarization," *Electronic Letters*, Vol. 29, No. 23, 1993, pp. 2004-2005.

## Chapter 4 - Antenna Simulation Results

### 4.1 - Introduction

Initially, the design procedure started out with using rectangular edge and inset-fed patch antennas at the frequency of 2.0GHz, as well as 2.7GHz, as the initial deformable mirror design was found to resonate best at those frequencies. However, after other prototypes of the mirror were designed, the resonant frequency deviated from 2.7GHz, which ultimately led to altering the requirements of the antenna design to a more wide-band model. Doing so also allows for use of imaging at different frequencies, which has become increasingly useful in this research as objects, such as cylinders with small notches, are being used as the back-propagation code becomes more robust; also, as the imaging is performed at higher frequencies, the defects in the material become larger in terms of wavelength, and are ultimately easier to detect. In these simulations, both Sonnet and HFSS were used to generate the figures that follow.

In the simulated work presented in this chapter, the results begin with what is known as an edge-fed patch antenna, and then are followed up with several different variations of antennas that use patches as the main source of radiation. From that point, the next few simulations are for several types of Vivaldi antennas.

### 4.2 - Simulated Results

First, shown in *Figure 4.1* is the standard edge-fed patch antenna with a quarter-wavelength,  $50\Omega$ -matched line that transfers the power to or from the patch with minimal loss. Initially designed to resonate at 2GHz, *Figure 4.2* shows that the resonant frequency has shifted by about 100MHz, which, as mentioned in Chapter 3, is due to the fringing fields on the sides of the patch making the antenna appear electrically larger, and the larger electrical size corresponds

to a lower frequency. Also, evident from *Figure 4.2*, the bandwidth of this patch is roughly only 40MHz, which is clearly not enough for use in this research.

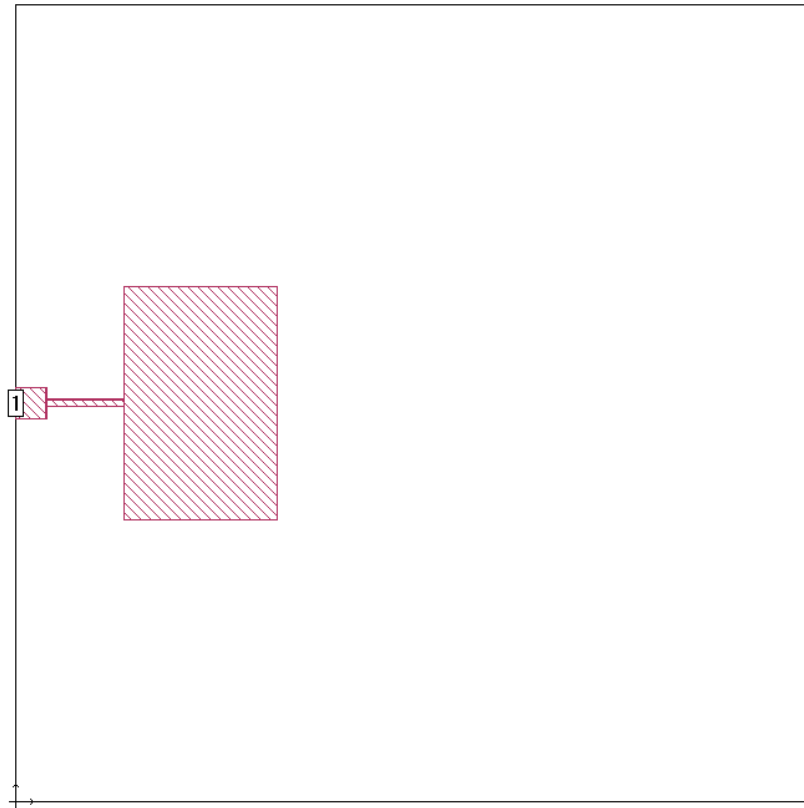


Figure 4.1 - Patch Antenna

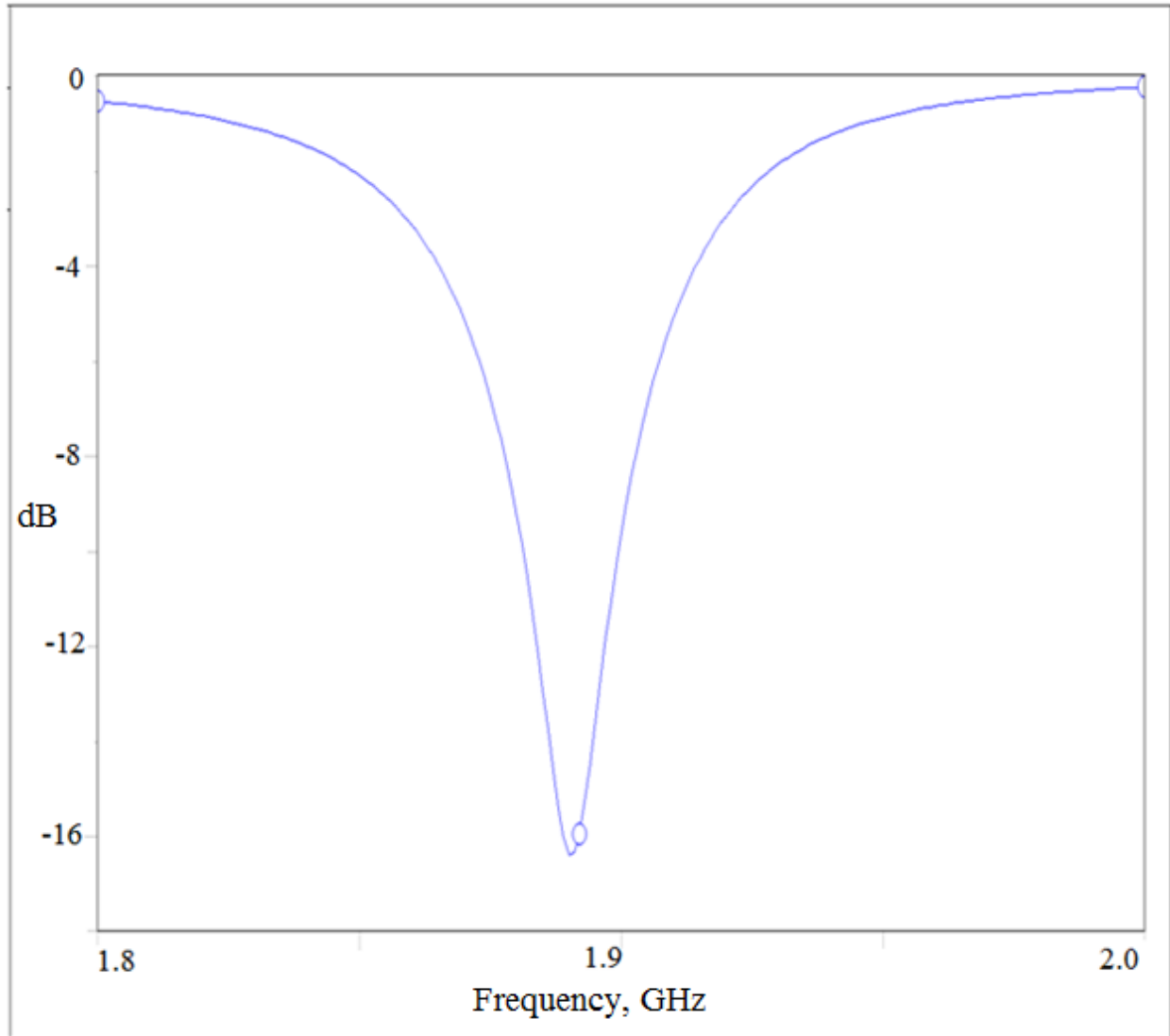


Figure 4.2 -  $S_{11}$  for Patch Antenna

After realizing that the single patch did not meet the needs required for our antenna array, the next step was looking into a 4x2 patch array; while the return loss had slightly improved, and the bandwidth was slightly larger at roughly 140MHz, these results were still not what was required, not to mention the size of the individual arrays was much larger than what would be useful for an imaging array.

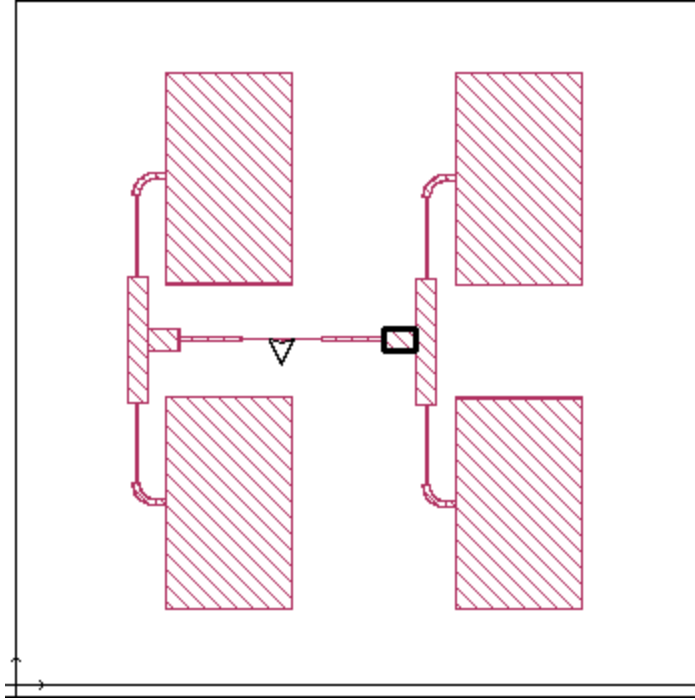


Figure 4.3 - 4x2 Patch Array

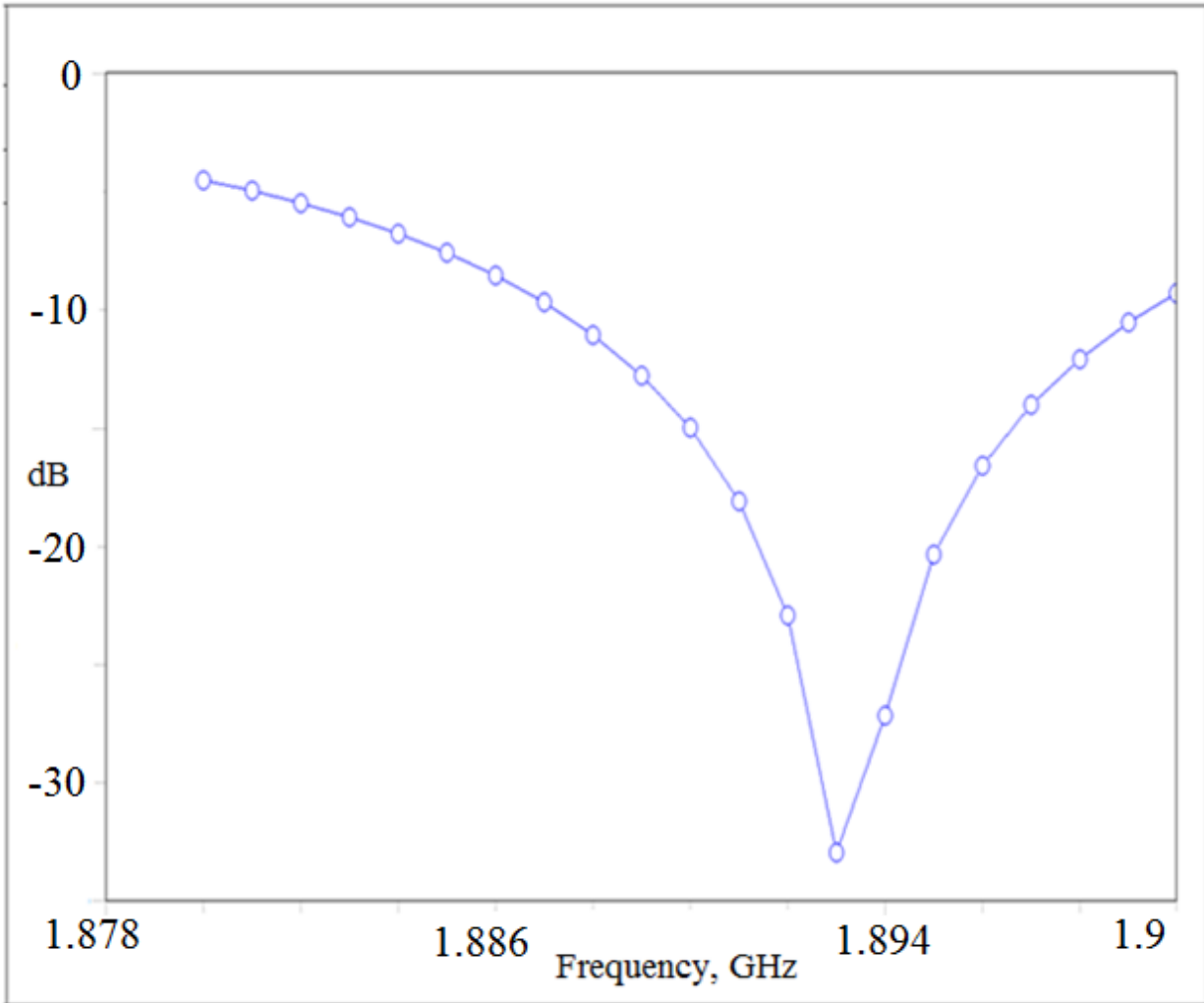


Figure 4.4 - Return Loss for 4x2 Patch Antenna Array

The next simulation that was run was for the 4x2 Corporate and Series-Fed antenna; while the return loss was strong, the bandwidth, again, was nothing near what was required. And, as pointed out in the previous chapter, the physical size of this antenna was much too large to employ in an imaging array.

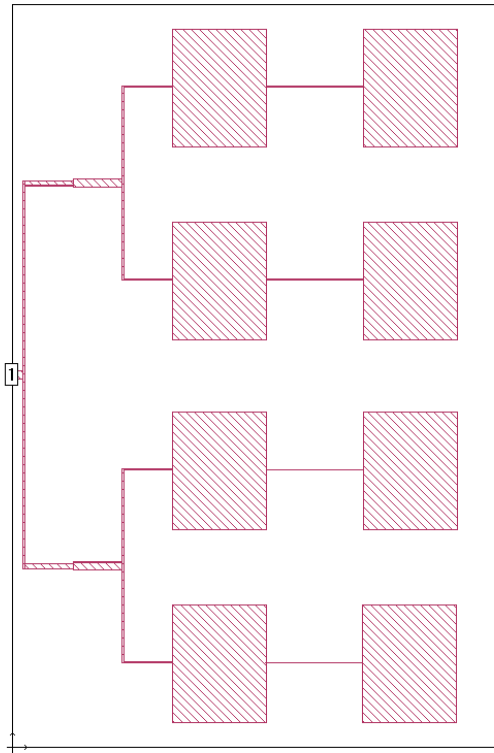


Figure 4.5 - Layout of Corporate Series-Fed Antenna

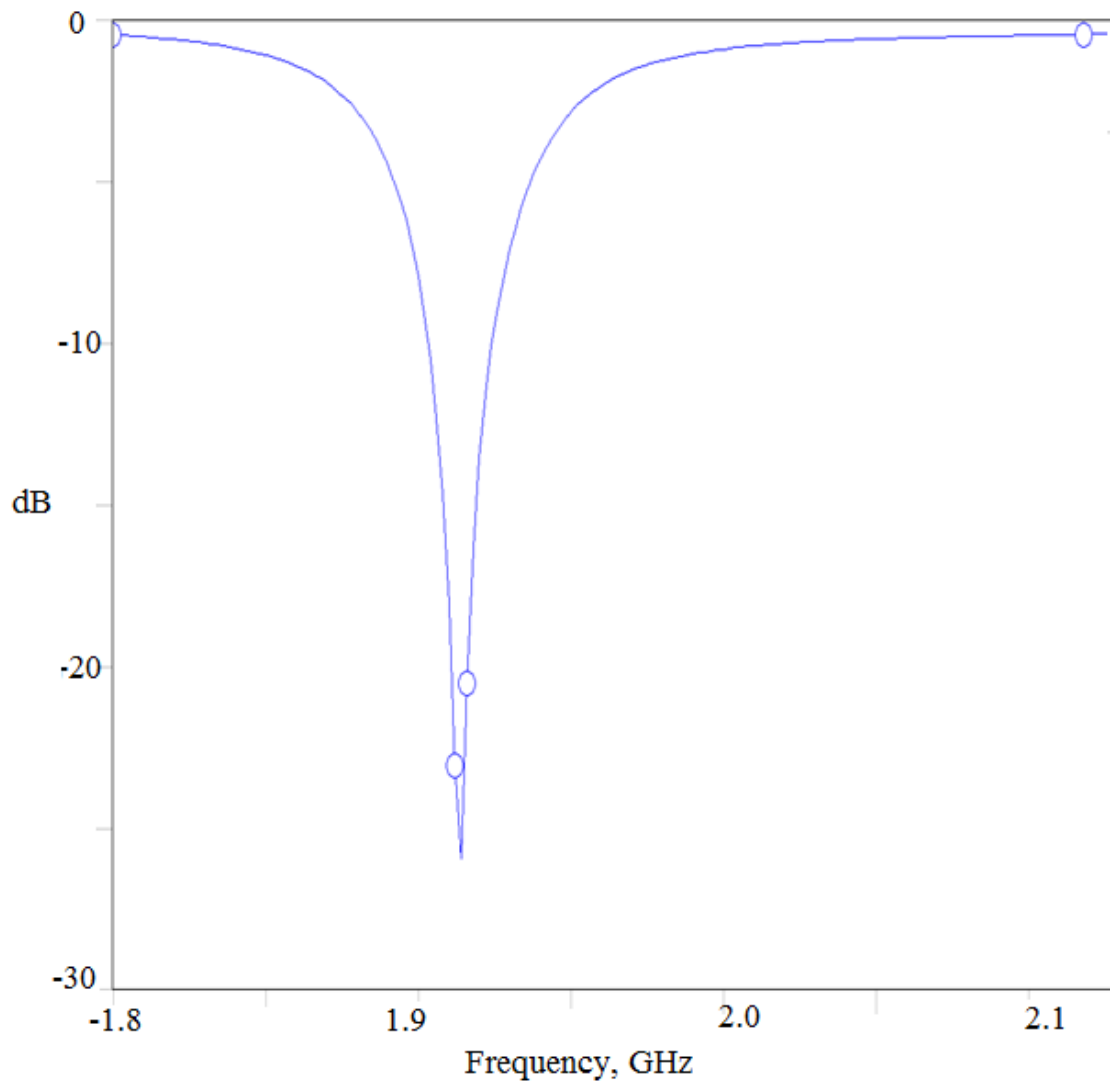


Figure 4.6 - Return Loss of Corporate Series-Fed Antenna

Next, the microstrip log-periodic antenna was simulated; here, inset-fed patches were used, and, beforehand, one of these single patches was fabricated that resonated at 2.7GHz, and it was used briefly in an array setting to capture the radiation pattern of a horn antenna. While this approach worked, the limiting bandwidth was what ultimately led in an attempt to design higher-bandwidth antennas. With the log-periodic, the resonances of the patches add up, so the points

on *Figure 4.8* where the  $S_{11}$  is dipping below -10dB is where the patches are resonating together. Similarly, in *Figure 4.9* and *Figure 4.10*, more elements were added, and while the performance of the antenna greatly improved, the radiation pattern was very sporadic, and did not have the narrow beamwidth that was required.

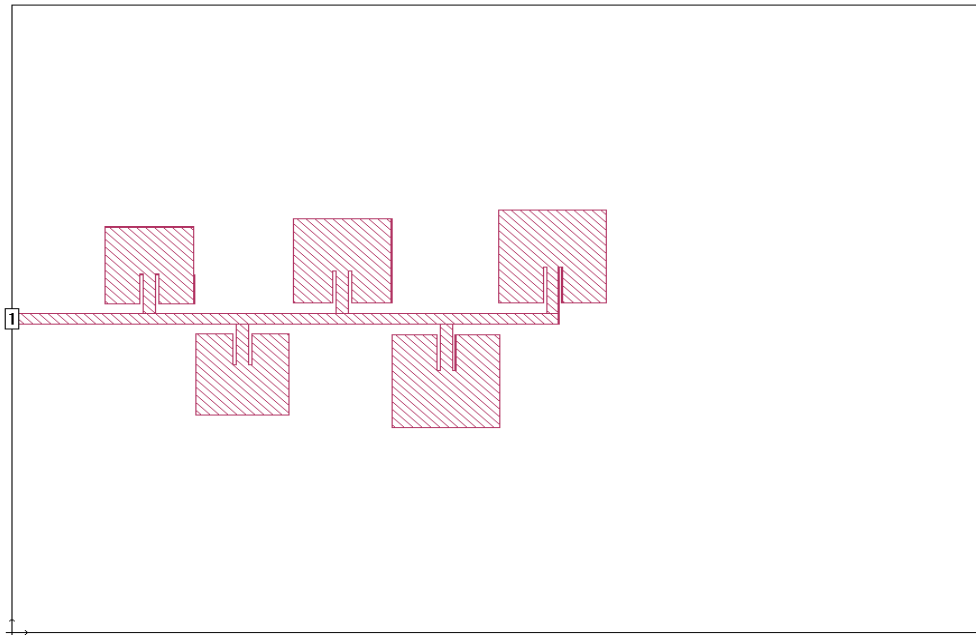


Figure 4.7 - Log-Periodic Microstrip Antenna

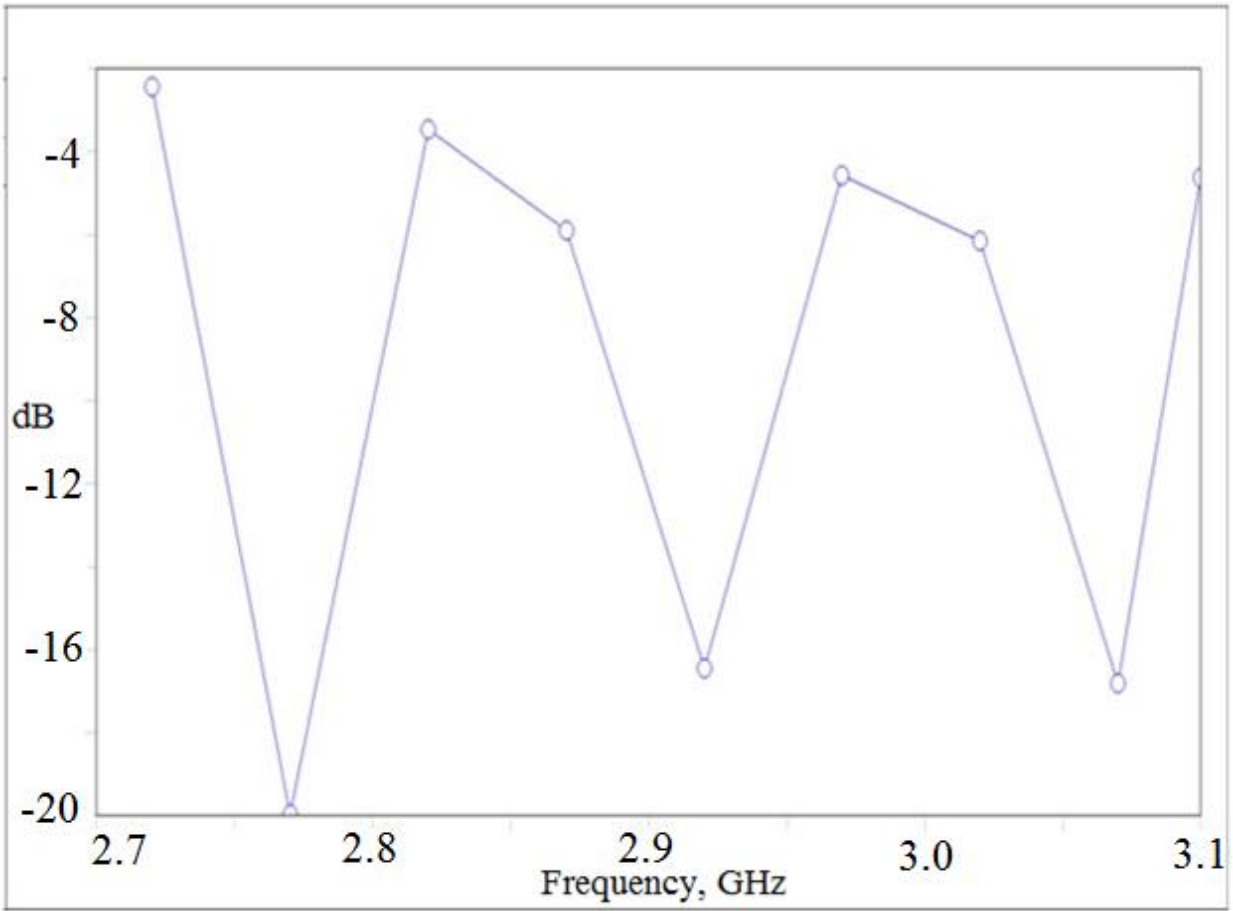


Figure 4.8 - Return Loss of 3-Element Log-Periodic Microstrip Antenna

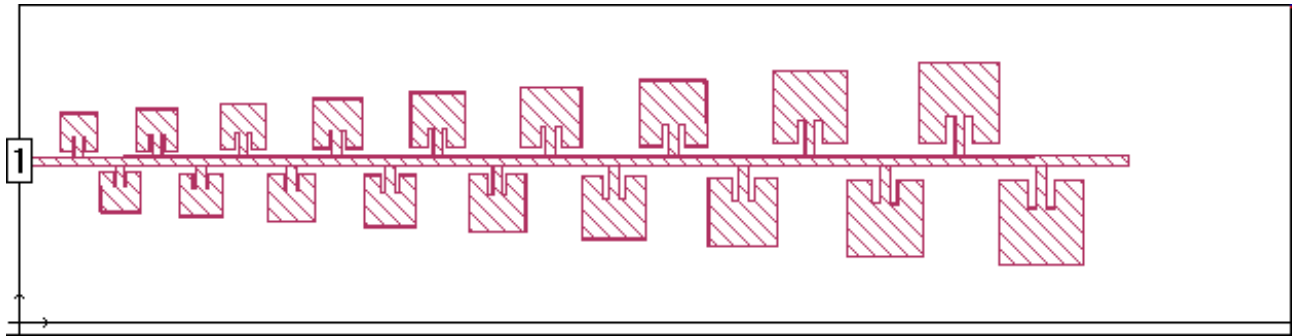


Figure 4.9 - More Elements in a Log-Periodic Microstrip Antenna

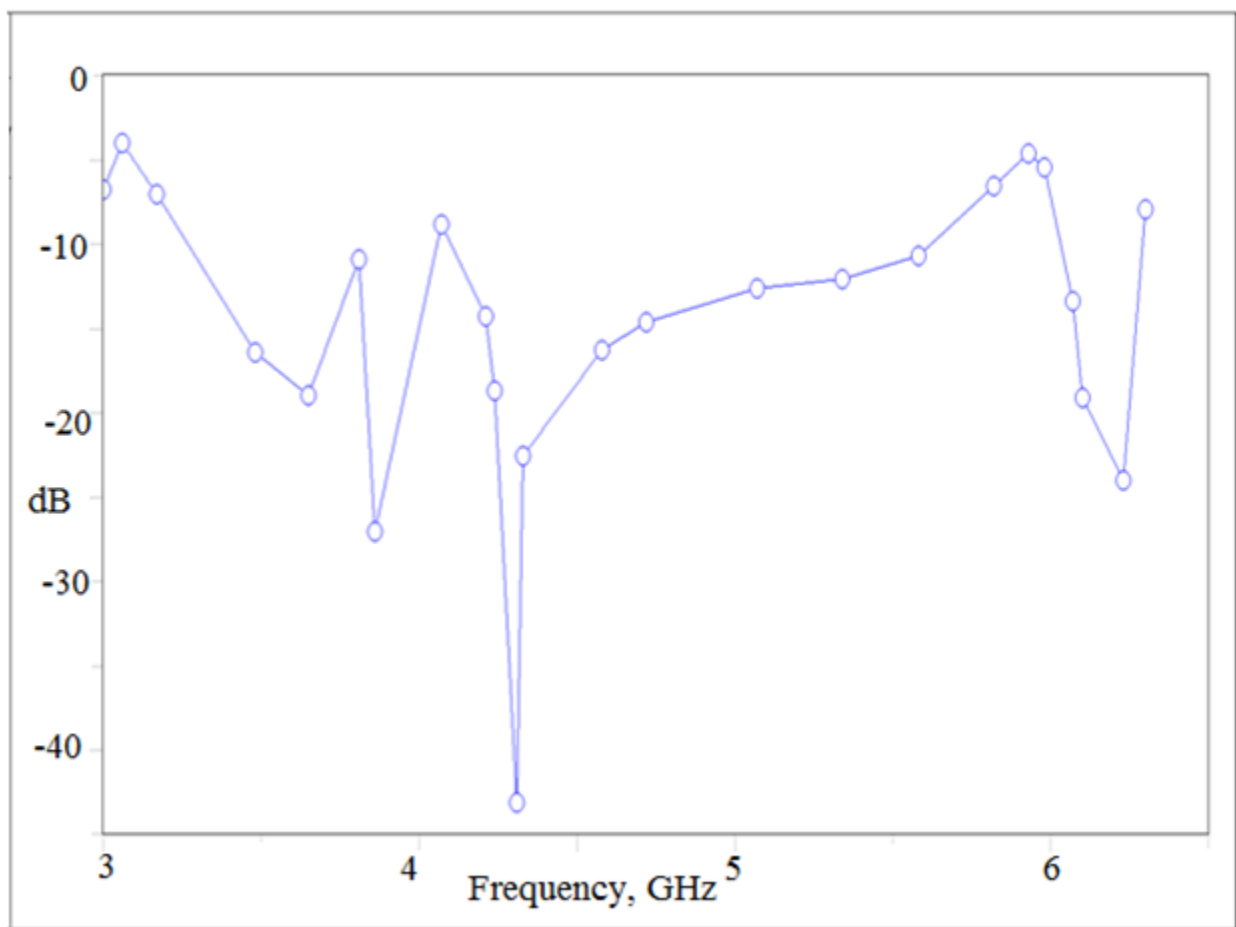


Figure 4.10 - Return Loss of 18-Element Log-Periodic Antenna

Because of the bandwidth and radiation pattern limitations of patch antennas, the next step was to find an antenna that would suit those needs, as well as be able to be fabricated on a

single dielectric board; Vivaldi antennas fit that need, and modeling of several designs in HFSS took place. The first design that was simulated was the traditional Vivaldi with the radial stub on the back-layer, as shown in *Figures 4.11* and *4.12*.

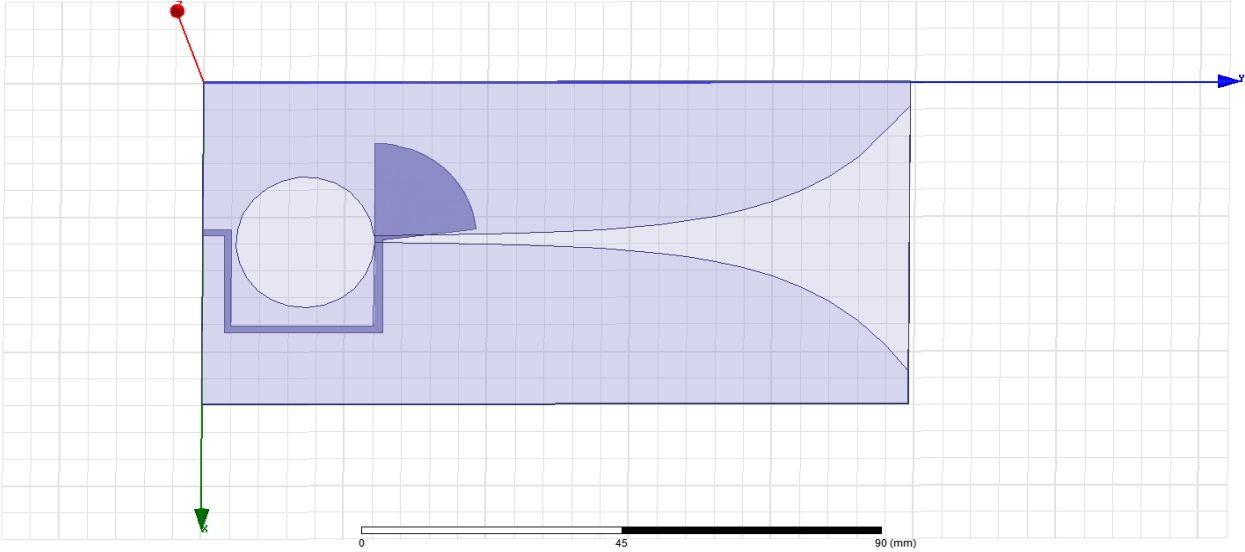


Figure 4.11 - Vivaldi Antenna Layout

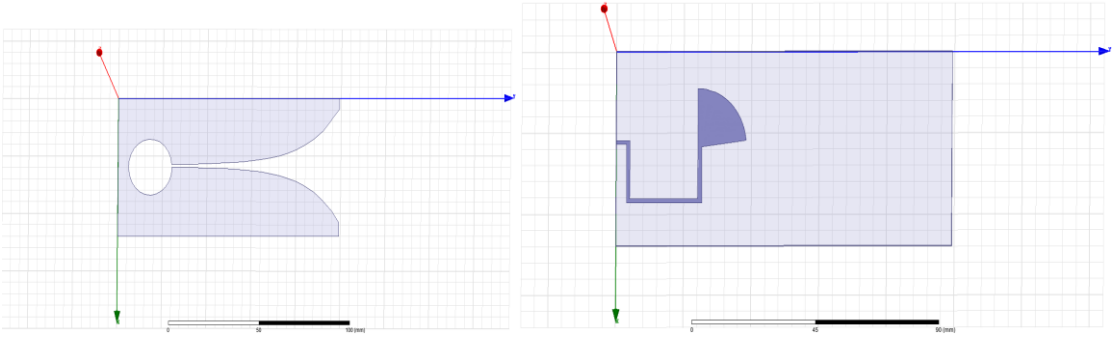


Figure 4.12 - Front and Back Layer of Vivaldi Antenna

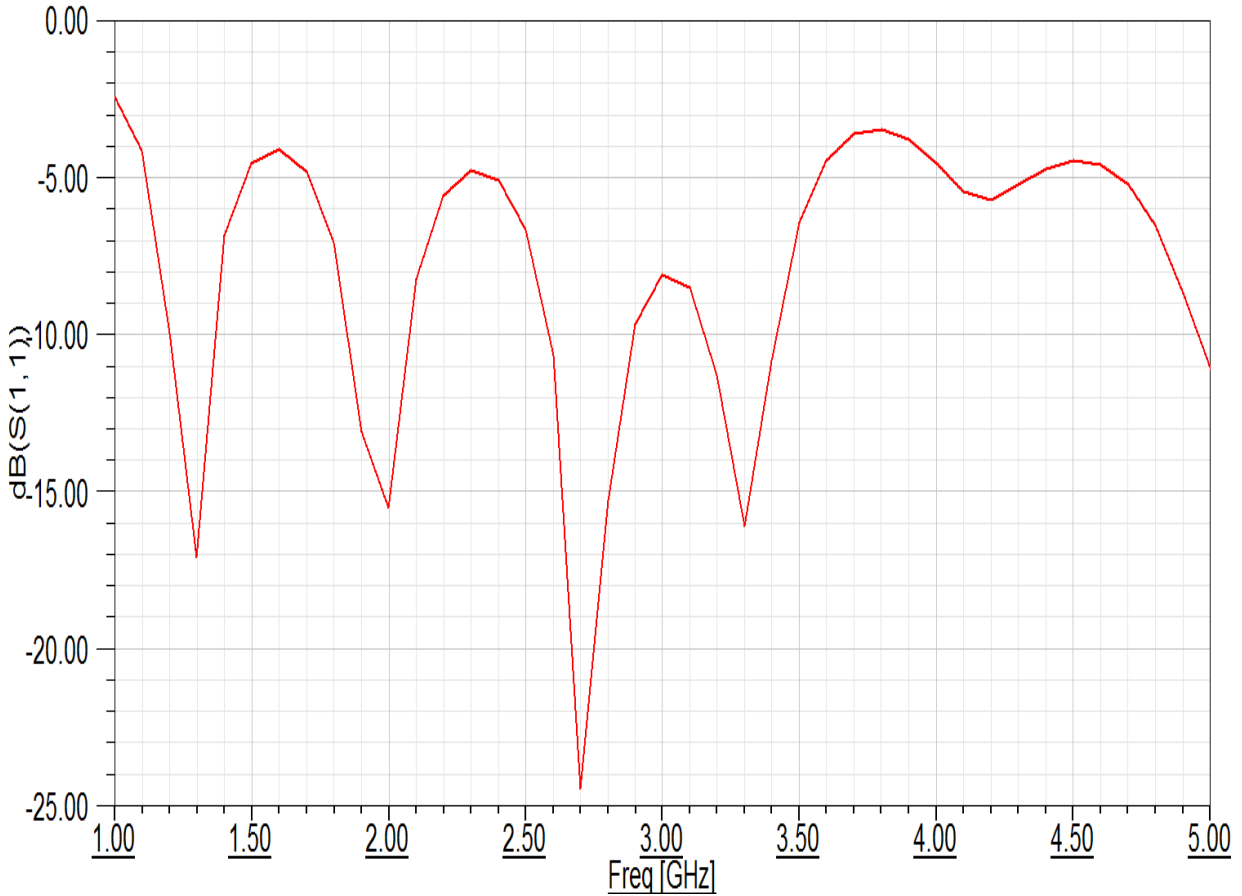


Figure 4.13 - Simulated Return Loss of Vivaldi Antenna

As can be seen in the figure above, the simulated return loss does drop below -10dB for certain frequencies, so this antenna was fabricated to see how well it would work as an array element. Upon testing the fabricated element, however, the measured return loss was much different than the simulation; the reason for this being is that while the flare rate of the antenna does not have to be exactly symmetric for proper radiation to occur, the radial stub on the back side was not directly lined-up with the opening of the flare on the opposite side, and this caused some of the radiation to not be sent down the flare. While this was something that could be fixed by fabricating another antenna, for an array of multiple antennas, it was determined that this low-tolerance to error in fabrication was not acceptable, as all antennas needed to operate in the same

manner so that accurate reconstructions would be possible. This is one factor that led to searching for a new design of Vivaldi antenna.

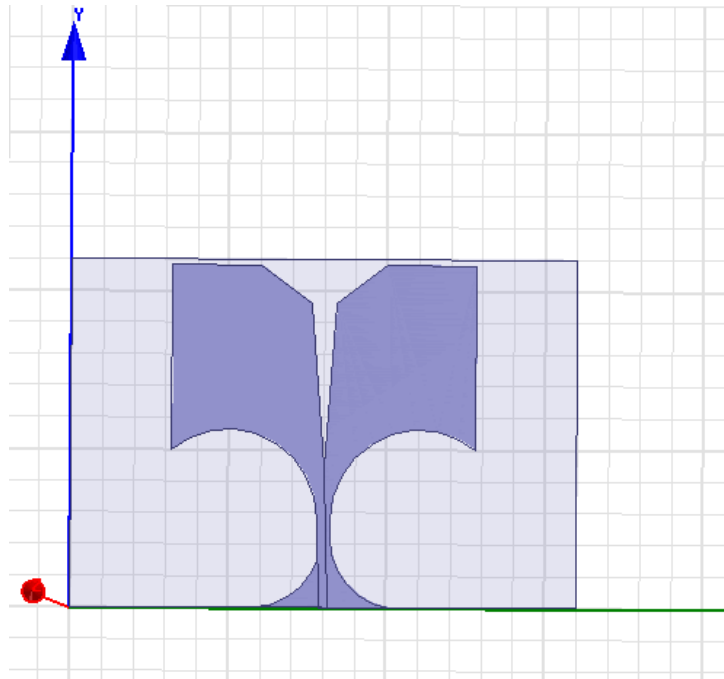


Figure 4.14 - Layout of Anti-Podal Vivaldi Antenna

As mentioned in the previous chapter, the Anti-Podal Vivaldi is an alternative to the traditional Vivaldi antenna, and does not require the radial stub on the back-side of the antenna for feed purposes; however, the simulated return loss, shown below, was not below -10dB for the desired frequency range, and, as also mentioned earlier, the cross-polarization issues with these antennas is often a large problem; this led to the next, and final, design of the balanced, anti-podal Vivaldi antenna, shown in *Figure 4.16* below.

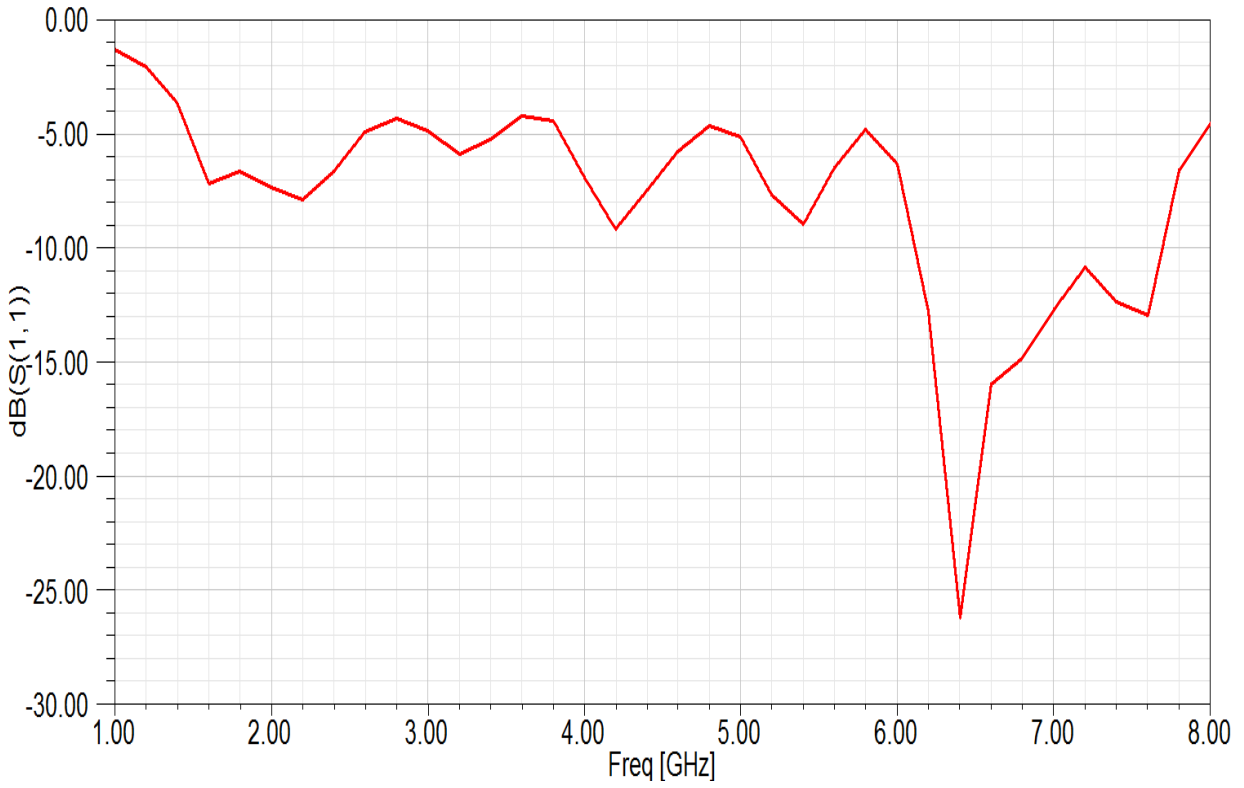


Figure 4.15 - Simulated Return Loss of Anti-Podal Vivaldi Antenna

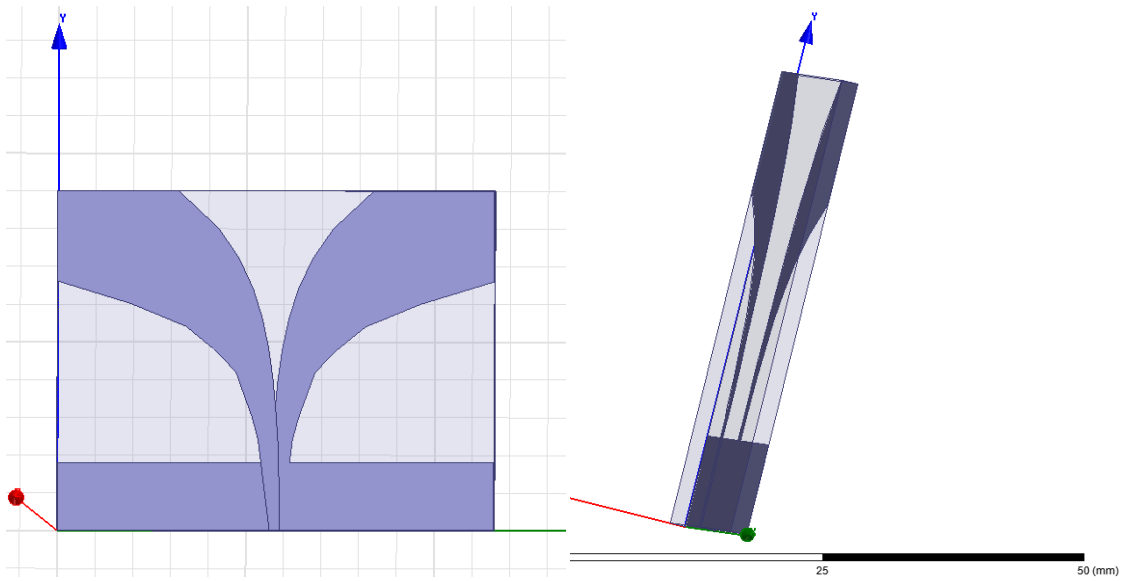


Figure 4.16 - Layout of Balanced, Anti-Podal Vivaldi Antenna (Top and Side-Views)

This design, once fabricated, had the dimensions of 8x6.5cm, which was much smaller than the initial Vivaldi antenna, which made designing the receiver arc and stands much easier. From *Figure 4.17*, the return loss shows that it is below -10dB for nearly the entire range of 2 - 8GHz, which is the range required for this research. As the following chapters will show, the measured return loss of the BAPV antenna is slightly better than that of the simulated values.

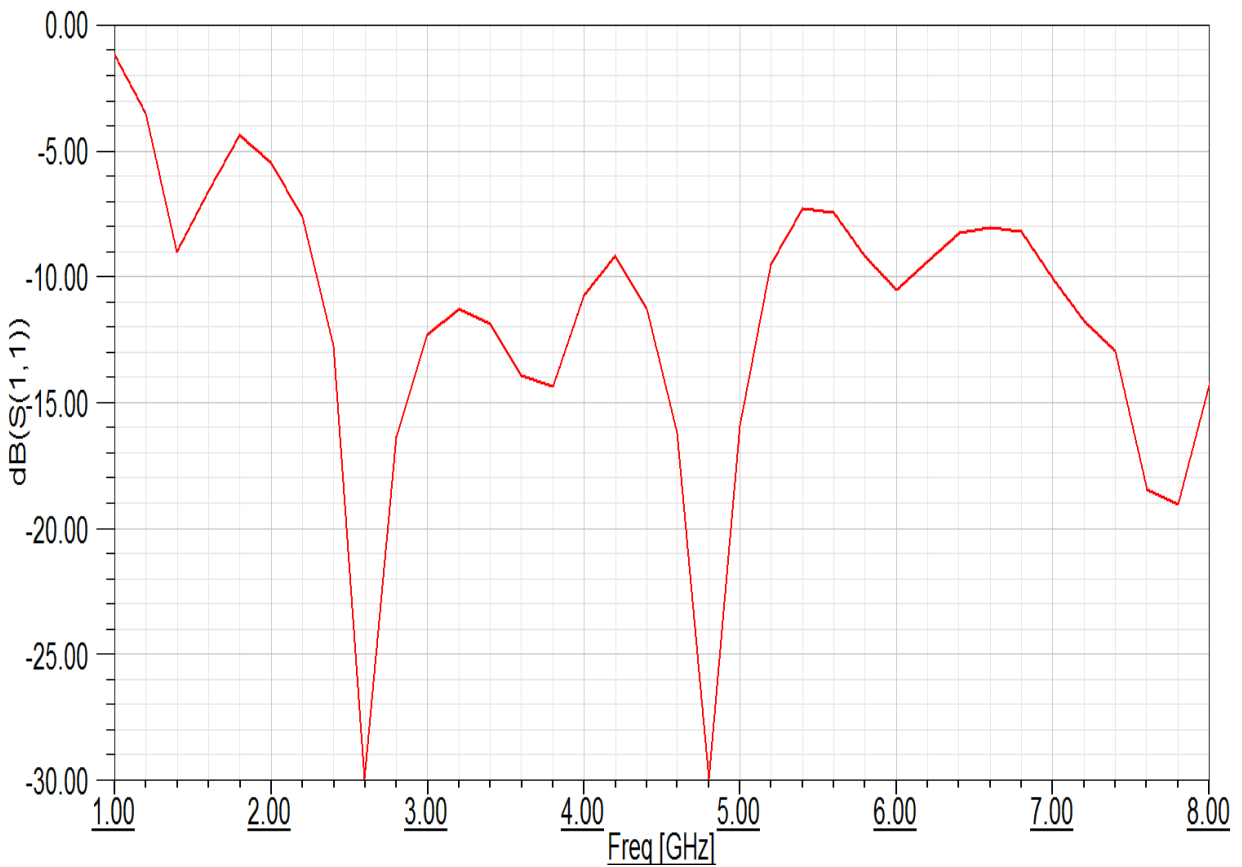


Figure 4.17 - Simulated Return Loss of Balanced, Anti-Podal Vivaldi Antenna

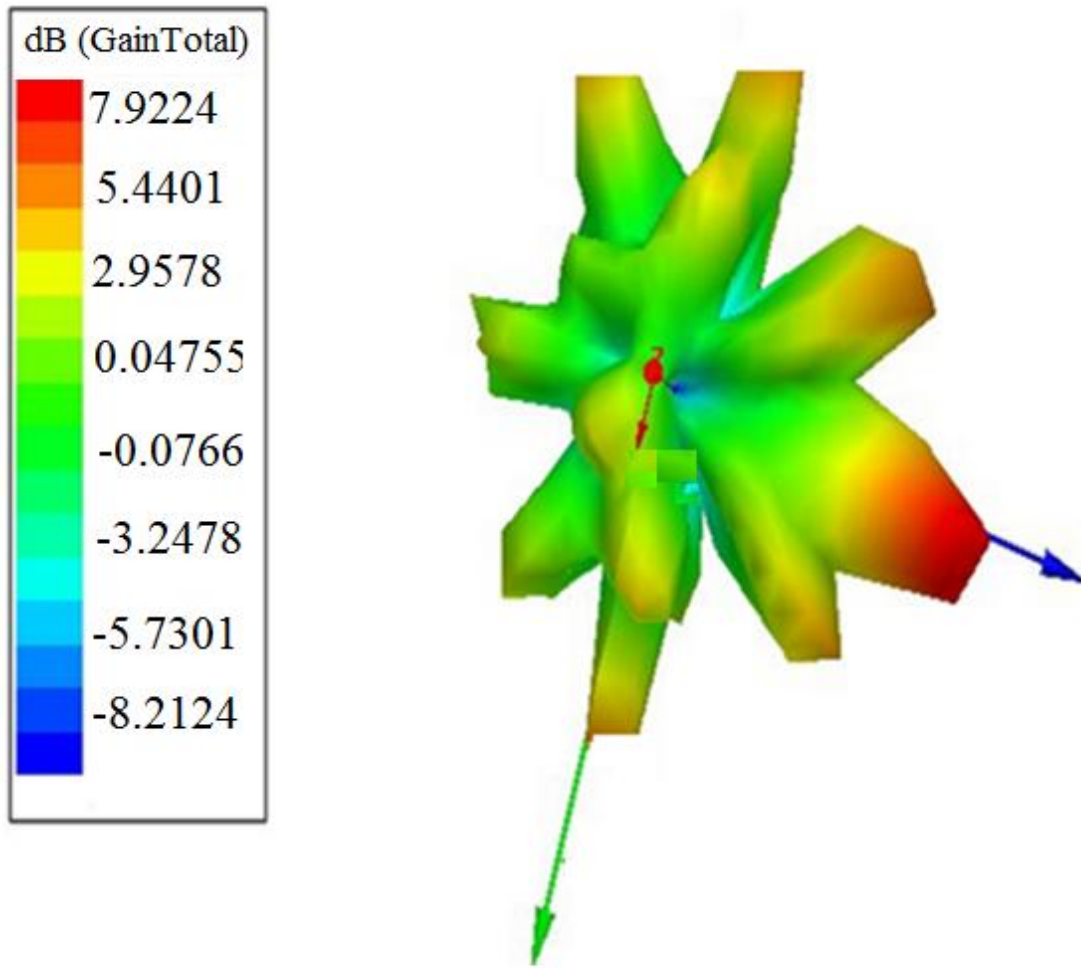


Figure 4.18 - Simulated Three-Dimensional Gain of Balanced, Anti-Podal Vivaldi Antenna at 6GHz

One of the criteria that none of the other antennas previously described in this paper were able to provide was a narrow beamwidth, and while this simulation does show some side-lobes that reach above 2dB, the main-beam reaches roughly 8dB in the simulation, and is narrow, around 15°, which is ideal for an imaging array [3].

WORKS CITED

## WORKS CITED

- [1] "The Basics of Patch Antennas." D. Orban and G.J.K Moenaut. Orban Microwave Products. <[http://www.orbanmicrowave.com/The\\_Basics\\_Of\\_Patch\\_Antennas.pdf](http://www.orbanmicrowave.com/The_Basics_Of_Patch_Antennas.pdf)> Last Accessed August 2013.
- [2] Garg, Ramesh, et. al. "*Microstrip Antenna Design Handbook*." Artech House, 2001.
- [3] Wood, Ian. "Linear Tapered Slot Antenna for Imaging Arrays." Master's Thesis, University of Victoria. 2005.

## Chapter 5 - Antenna Control

### 5.1 - Introduction

For a fully-automated receiving array, very few options are available for a low-cost system that involves a two-port VNA, and as such, to accomplish switching for large amounts of antennas, *Figure 5.1* shows a basic block diagram of how the switches are used with different levels of control logic that will route the data from a single antenna ultimately to the VNA and then to a PC, where the MATLAB code will take the input data.

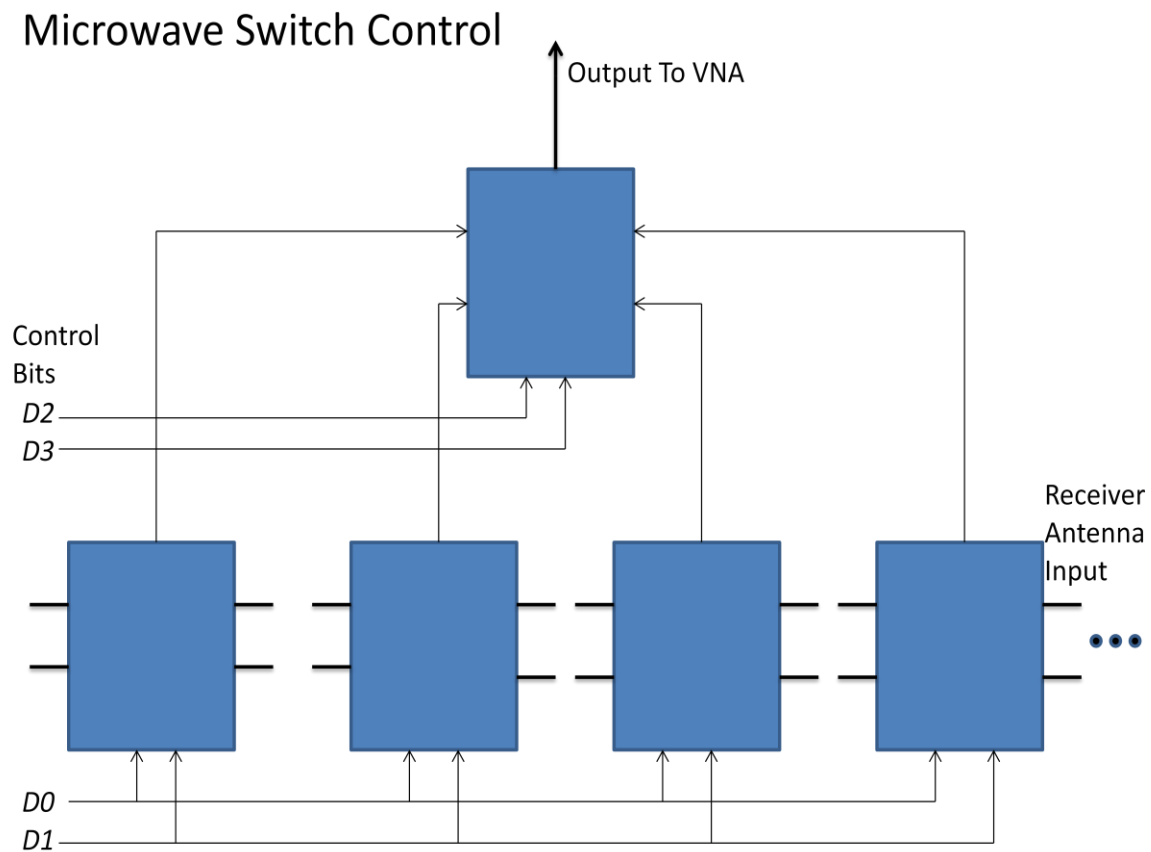


Figure 5.1 - Control for Multiple Switches

So, for example, *Figure 1* shows for 16 antennas can be controlled while using four control bits, which are generated from LabVIEW. The output of each of the switches are fed to

the switch on the next 'level,' which, by using a different sequence of control bits, will select one antenna to read the data from. As will be seen later in this paper, a two-level system operates very well, in terms of transmitted signal power, and many more levels could also be added on, when more antennas are required.

## **5.2 - Initial Designs**

For obtaining the data from the antennas, an automated system was sought that would allow for readings to be taken in a fast and accurate manner. Initially, HP 33312B switches were used, along with control circuitry that consisted of the switching transistor and damping diode, that would allow for fast switching between the different antennas of the receiver array. One of the main issues with this system, however, was the need for multiple 24-volt power supplies, as well as a need for many switches, as there were only two inputs and one output per switch. The inability to find similar switches for purchasing was also a factor that led the design down a different path. The method of switching the antenna elements to be read by the VNA by hand was also employed, but significant error came from this approach, in that the antennas were moved slightly out-of-place when attached to the VNA, but also in that this method was very time-consuming, for even a small number of antenna elements.

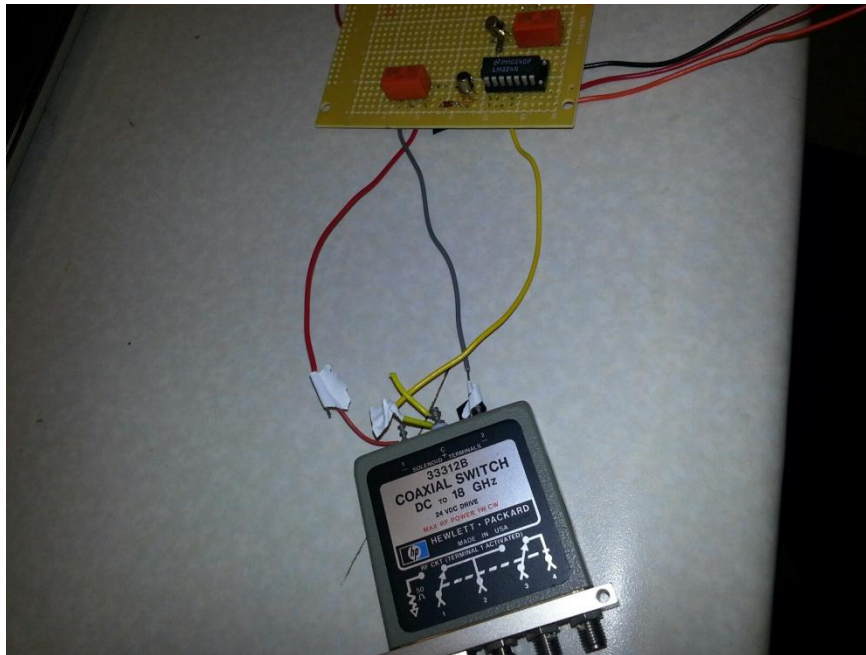


Figure 5.2 - Initial Switch Design with HP Coaxial Switch

As another option, and one that is rather inexpensive compared to other options, was to use PIN diodes as a mechanism of switching between antennas. A PIN diode can be thought of as a current-controlled diode, compared to a varactor diode, which is controlled by an applied voltage. In the context of switching, a PIN diode, along with a DC-blocking capacitor and an RF choke, can be used to either pass or block an RF signal if a control bias is applied; the PIN diode acts as a potentiometer, and when the control bias is applied, it maintains a very low value of resistance, allowing the signal to pass through. Likewise, when the control bias is not applied, the PIN diode will possess a very high resistance, which will block the incoming RF signal.

The main difference separating a regular diode and a PIN diode is that the depletion region existing between the P and N regions is larger. In PN junctions, the P region contains a large amount of holes, and the N region contains electrons. The region between the P and N

regions contains no charge carriers as any holes or electrons cancel and behaves as an insulator [2].

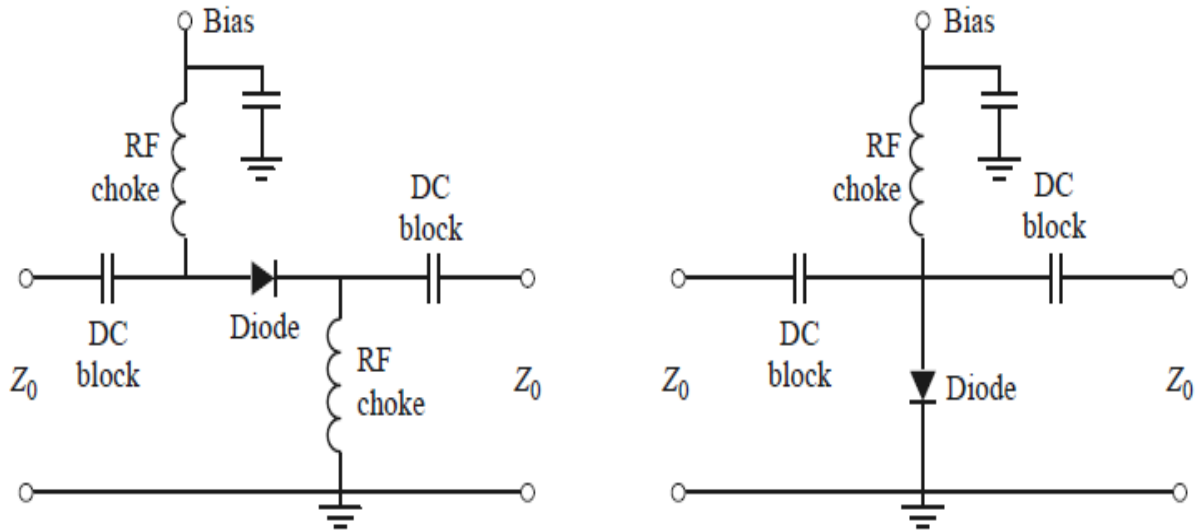


Figure 5.3 - Series and Shunt Configurations for PIN Diode Switches [1]

### 5.3 - Fully-Automated Switching System

In the previous designs, there were positives and negatives for each; the cost of the PIN diode switching option was much less-expensive than that of the HP Coaxial switch alternative, but the manufacturing and impedance matching of the PIN diode design was very sensitive. Likewise, if the final choice would have been to go with the coaxial switches, finding the same model of switches would have been difficult, as those are no longer in production. After these realizations, a need for a simpler switch with less room for error, such as altered phases from slightly different machined path lengths, was required. After looking for some time, the SP4T HMC345LP3 chip from Hittite Microwave Corporation was found, and the option was also available to purchase the evaluation board, pictured below, which has the chip, as well as the DC-blocking capacitors and SMA connectors already soldered on the PCB board, which, if we

were to manufacture these on our own, the cost would still be over half of what the switches cost, but there would still be room for error in the fabrication and soldering processes, so the final decision was to go with the evaluation boards.



Figure 5.4 - Hittite HMC345LP3 Microwave Switch

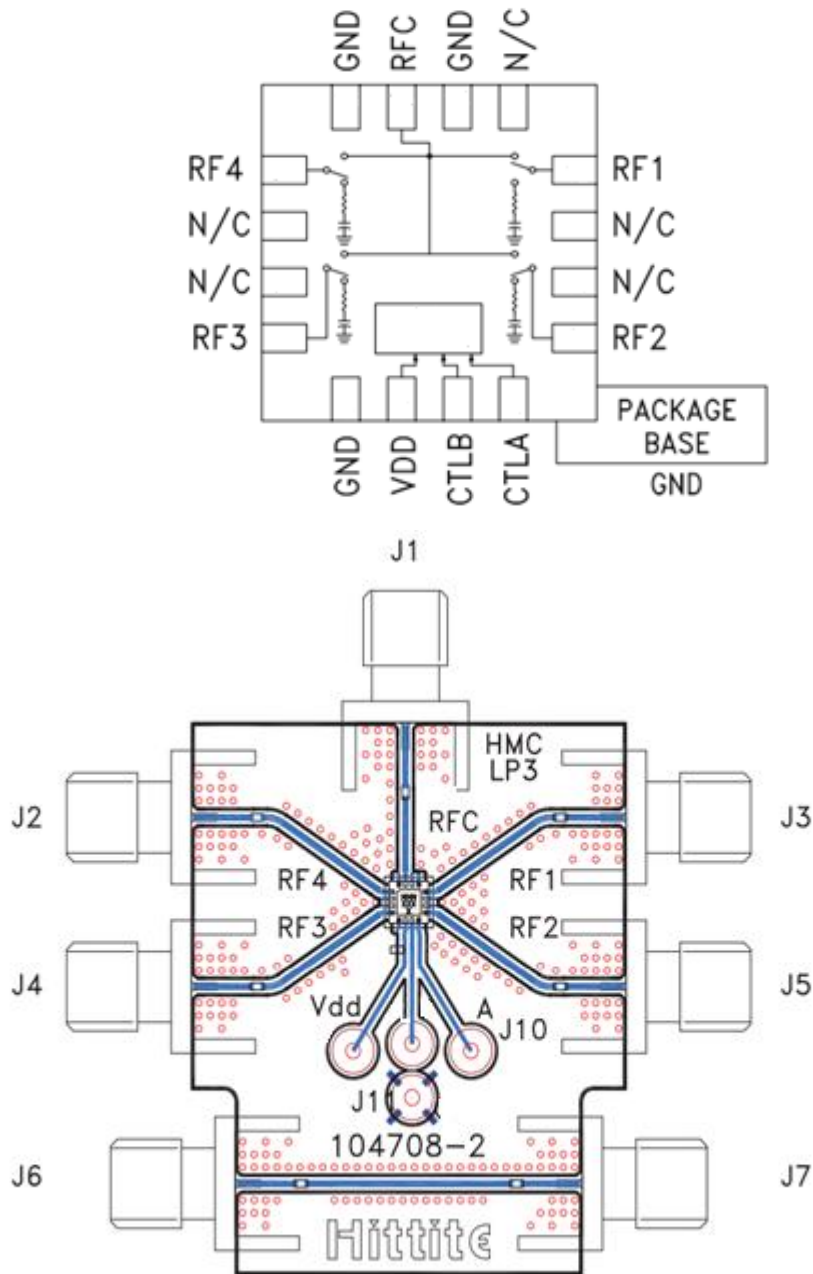


Figure 5.5 - Schematic of Hittite HMC345LP3 Chip and Evaluation Board

#### 5.4 - LabVIEW Control

As previously mentioned, in order to select the proper antenna to gather the necessary data, control logic sequences must be applied to the microwave switches that follow the truth table below:

A	B	Output
Low	Low	RF1
High	Low	RF2
Low	High	RF3
High	High	RF4

Table 5.1 - Truth Table for Antenna Control Via Microwave Switch [3]

So, for example, if (A, B) were set as (1, 0), then that specific microwave switch would 'select' the antenna connected via a coaxial cable, and send that data through the output port. As seen in *Figure 5.1*, there is a need for more than one switch when more than four antennas are used, as well as for multiple levels or stages to be implemented so that many antennas can be implemented in the imaging array. Initially, to provide these control bits, a microprocessor was used that could be programmed to send high and low bits; however, using this did not allow for changes during the run-time by the user, as the logic levels had to be programmed beforehand, so the need for a user-interface and run-time control was now the main priority.

While there were several options that would allow for control bits to be written with a user-interface, there was a need for up to eight control bits, which only LabVIEW provided through its In/Outport.32 VI (Virtual Instrument), which writes to, and reads from, a computer's parallel port, allowing the user to select which sequence of control bits are sent to the parallel port, and, ultimately, sent to the microwave switches to control which antenna the data is read from. With using different levels of switches in this design, we are able to send the same control logic signals to the same level, as can be seen in *Figure 5.1*; these eight control bits allow for up to 256 antennas to be used in the imaging array. How this works is that, for example, in a 20-element array, there are eight switches, and three levels of switches - five switches on the first level, two on the next and one on the final level. Again, every switch on the same level receives the same two bits of control logic, so for a sequence of (1, 0), the second antenna on each switch

is selected. For the next level of switches, two different control logic sequences are sent to the switches, which opens the path for the RF signal to go through, and, finally, the last switch, which is connected to the VNA, receives the final two control logic bits, and allows the data from the second antenna of the array to pass through to the VNA. *Table 5.2* shows the mapping of control bits for the 20-element array just described.

Antenna Number	D0	D1	D2	D3	D4	D5	D6	D7
0	0	0	0	0	0	0	0	0
1	1	0	0	0	0	0	0	0
2	0	1	0	0	0	0	0	0
3	1	1	0	0	0	0	0	0
4	0	0	1	0	0	0	0	0
5	1	0	1	0	0	0	0	0
6	0	1	1	0	0	0	0	0
7	1	1	1	0	0	0	0	0
8	0	0	0	1	0	0	0	0
9	1	0	0	1	0	0	0	0
10	0	1	0	1	0	0	0	0
11	1	1	0	1	0	0	0	0
12	0	0	1	1	0	0	0	0
13	1	0	1	1	0	0	0	0
14	0	1	1	1	0	0	0	0
15	1	1	1	1	0	0	0	0
16	0	0	0	0	1	0	0	0
17	1	0	0	0	1	0	0	0
18	0	1	0	0	1	0	0	0
19	1	1	0	0	1	0	0	0

Table 5.2 - Control Logic Sequence for 20-Element Antenna Array

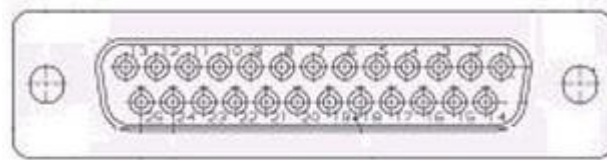


Figure 5.6 - Parallel Port Pin-Out [4]

As previously mentioned, the over-arching goal of the array is to have it fully-automated. The three figures below show a brief glimpse of how that is accomplished, but more description is needed to detail the entire process. For the LabVIEW portion of antenna control, several virtual instruments were combined into one that allows for the user to simply input the number of antennas that are in the imaging array and what the file name that the data to be stored for each element should be called. Once the program starts, the control bits are initially set all to zero, and for that corresponding logic sequence, the data from that antenna is passed through the microwave switches to the VNA, which averages and reads the data for the given antenna. After the data is read, it is then transferred by a sub-VI that gathers the data from a GPIB (General Purpose Interface Bus) to the PC, where it is stored as a text file. After this is completed, the control bits will increment by one, and the process of reading, averaging and passing the data will continue, until the number of antennas specified by the user have been read from.

Because of the need for multiple projections to be taken in order to obtain a more-complete representation of the object being imaged, a rotating stage was developed that, by use of a stepper-motor, allows for small (or large) angle rotations of the object. *Figure X.9* and *Figure 5.10* show the stepper motor with stand and some of the LabVIEW control, respectively, that, along with some simple op-amps and 555-timing circuits, allow for precise rotation of the stage. As was made clear in the Introduction of this thesis, and will become more evident in the Results section, since we do not have a rotatable source and receiver array, rotating the object is a replacement for not having that setup, that is commonly found in microwave or X-Ray tomography.

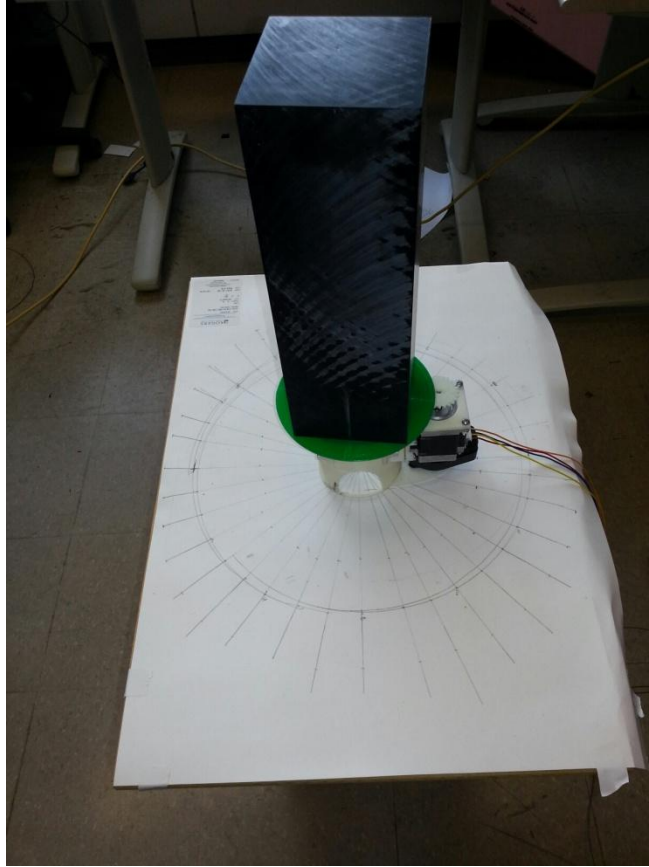


Figure 5.7 - Stepper Motor

WORKS CITED

## WORKS CITED

- [1] Poole, Ian. "PIN Diode Variable RF Attenuator Circuit." Radio-Electronics.com  
<<http://www.radio-electronics.com/info/rf-technology-design/attenuators/rf-variable-pin-diode-attenuator.php>>
- [2] "PIN Diodes". Microwaves 101.  
<[http://www.microwaves101.com/encyclopedia/diodes\\_PIN.cfm](http://www.microwaves101.com/encyclopedia/diodes_PIN.cfm)>
- [3] Hittite Microwave Corporation. "HMC345LP3 Data Sheet." v04.0805.
- [4] "Using the Parallel Port in LabVIEW." National Instruments Corporation, 2004.

## **Chapter 6 - Simulations for Antenna Control**

### **6.1 - Introduction**

The purpose of this chapter is to show simulation results that served as a test to see how the SP4T switches from Hittite Microwave would operate, based on simulations performed in Agilent's Advanced Design Software (ADS). Where ADS separates itself from other electromagnetic simulation software, such as HFSS or Sonnet is that it has many drag-and-drop features for transmission lines, filters, diodes, capacitors, etc, that do not have to be designed from scratch, but, rather, can be added to a circuit by specifying a few values. From the data sheet provided by Hittite Microwave Corporation for the SP4T microwave switch, there was no detail given about the device as to what was actually used for the switching mechanism, so, based on reading from [1], and from prior knowledge, PIN diodes were used in the simulation as the switch, with one of the main reasons being that they possess very fast switching times, and, based on whether they are in forward or reversed-biased mode, can provide either high or low impedance, which acts as either blocking or allowing a signal to pass through. PIN diodes act as essentially current-controlled resistors, and the larger amount of DC current in the intrinsic region, the lower the resistance [2].

### **6.2 - Design Procedures and Results**

Before purchasing the switches from Hittite Microwave, it was decided to model the devices to see if they would operate as demonstrated in the data sheets.

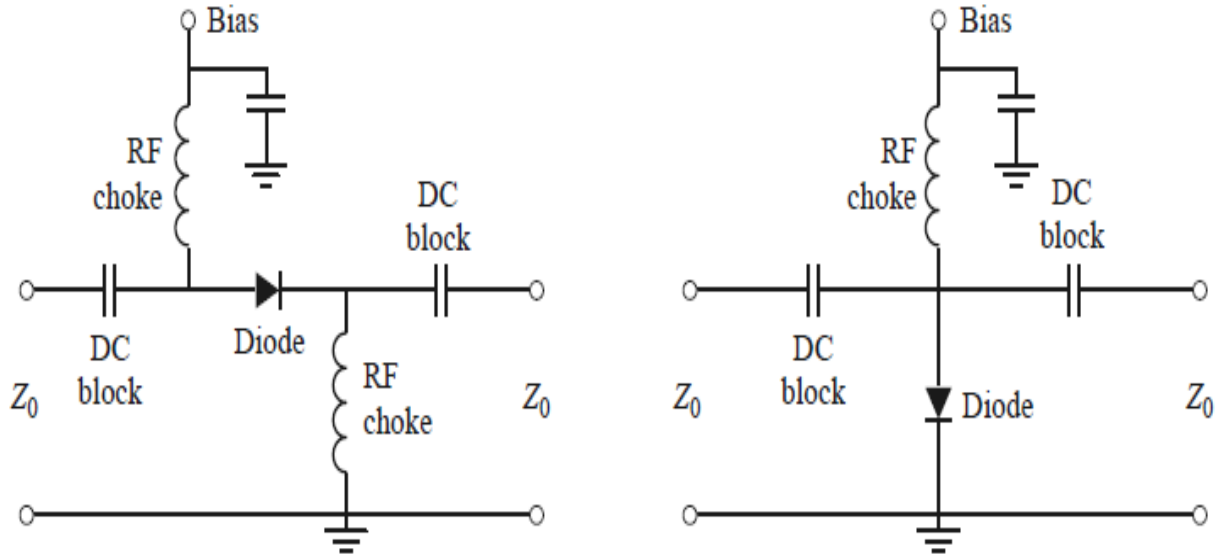


Figure 6.1 - Series and Shunt PIN Diode Switches [1]

From *Figure 6.1*, the two different configurations can be seen for a PIN diode switch: either the series or shunt method, and, for this research, the shunt configuration was chosen due to the fewer components required, and, if this were to be made into a physical circuit, the ON state, which in this research is only one switch at a time, requires -5V, while the high-impedance OFF state requires +5V; the positive power supplies are much easier to obtain, and therefore influenced the decision greatly.

In beginning the simulations, 3GHz was chosen as the center frequency, as that is roughly the frequency where most of the research on this project takes place, as well as being near the middle of the range of this switch; Hittite rates them as ranging from DC-8GHz switches. To first see if this idea would work in ADS, the first model that was simulated was a SPDT, and the results of this can be seen in the following figures. To obtain these results, PIN Diode default

values given by [3], some standard capacitor and inductor values,  $\lambda/4$  lines and the Rogers 4350 Laminate, specified by [4] were used.

From *Figure 6.3*, we can see that for the reverse-biased mode, the  $S_{21}$  values indicate that the data is being transmitted from Port 1 to Port 2, and, from *Figure 6.4*, the forward-biased mode, it is seen that the  $S_{21}$  has a low value, meaning that the data is not being transmitted from Port 1 to Port 2. Clearly, these results show that for the proper bias voltage applied, -10V for reverse-biased and +10V for forward-biased, the SPDT switch operates correctly, and from this, the basis for a SP4T were constructed.

For expanding the design to a SP4T, several different layouts were tried that would fit the criteria that each path for the RF signal needed to travel a distance of  $\lambda/4$  from the input of the antenna, and then, if the antenna was selected based on the control logic, would travel another  $\lambda/4$  distance to the output of the SP4T, which, in the case of these simulations, is Terminal 1 in the ADS model. To accomplish this, cross and tee-joints were used in the ADS model, which allowed for four different PIN diode switches to be created with equal pathways, as can be seen in *Figure 6.5*.

dB ( $S_{21}$ )  
dB ( $S_{11}$ )

### SPDT in Forward-Bias Mode

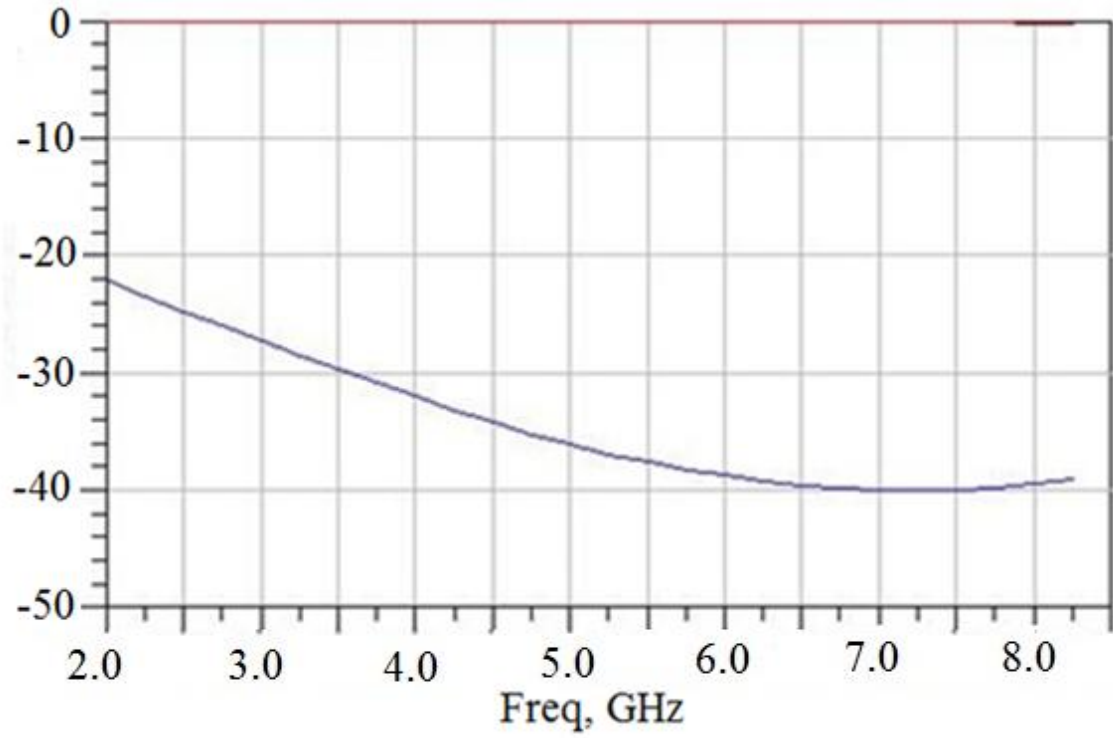


Figure 6.2 - S-Parameters for SPDT in Reverse-Biased Mode

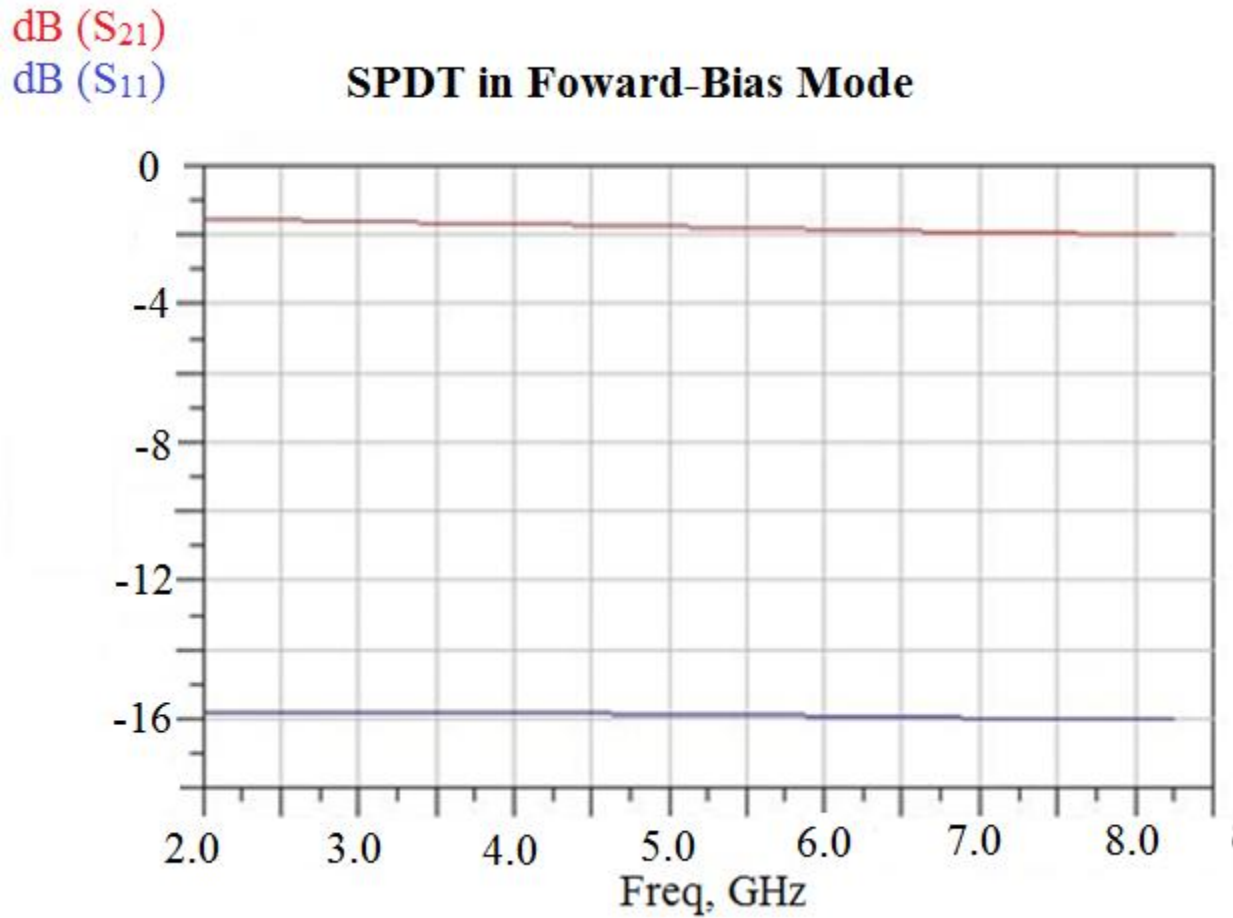


Figure 6.3 - SPDT in Forward-Bias Mode

Very similar to the previous SPDT, the SP4T will route a signal to Terminal 1 if the bias voltage is -5V; otherwise, the switch will resemble an OFF, high-impedance state that will block the incoming RF signal from the antenna. The S-parameter results are shown in *Figure 6.6 and 6.7*, and demonstrate how a reverse-bias voltage at Port 4 and Port 3 will alter the transmitted signal.

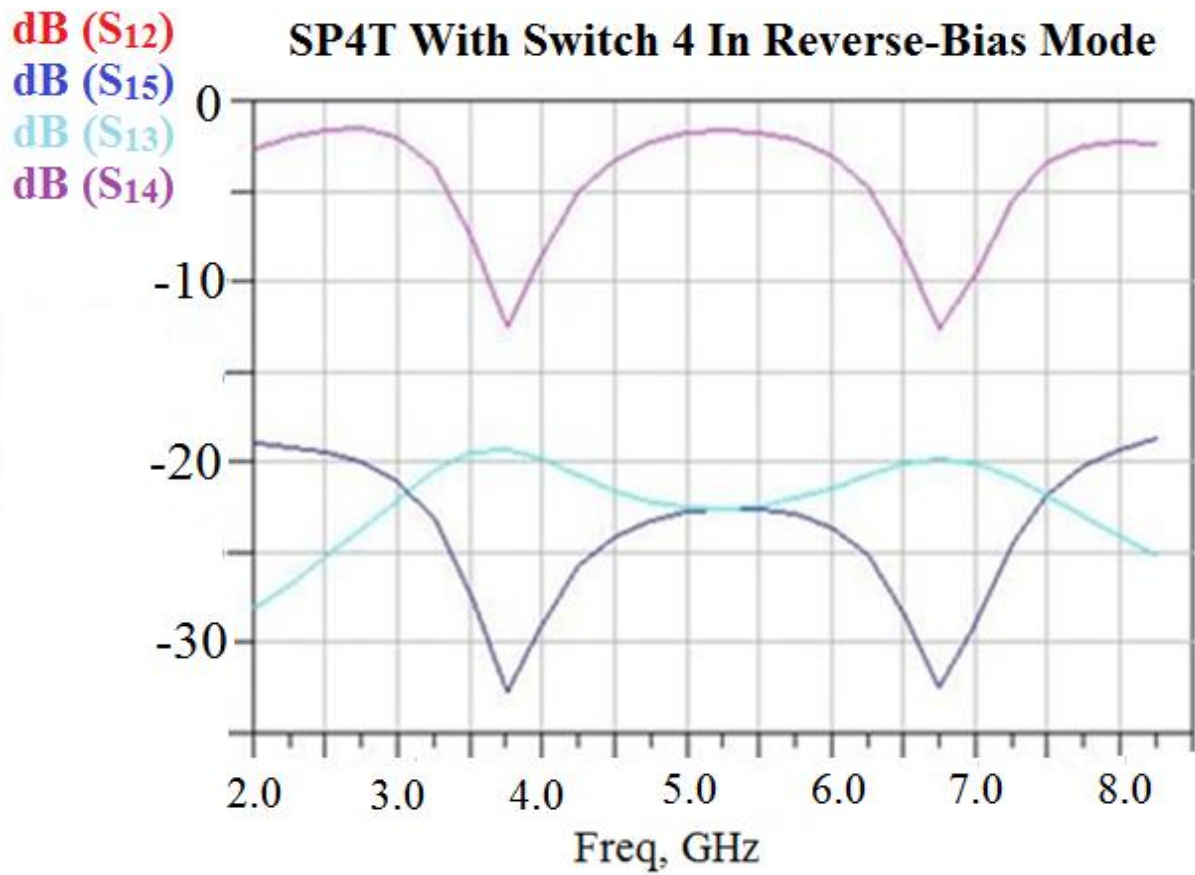


Figure 6.4 - SP4T for Switch 4 Selected

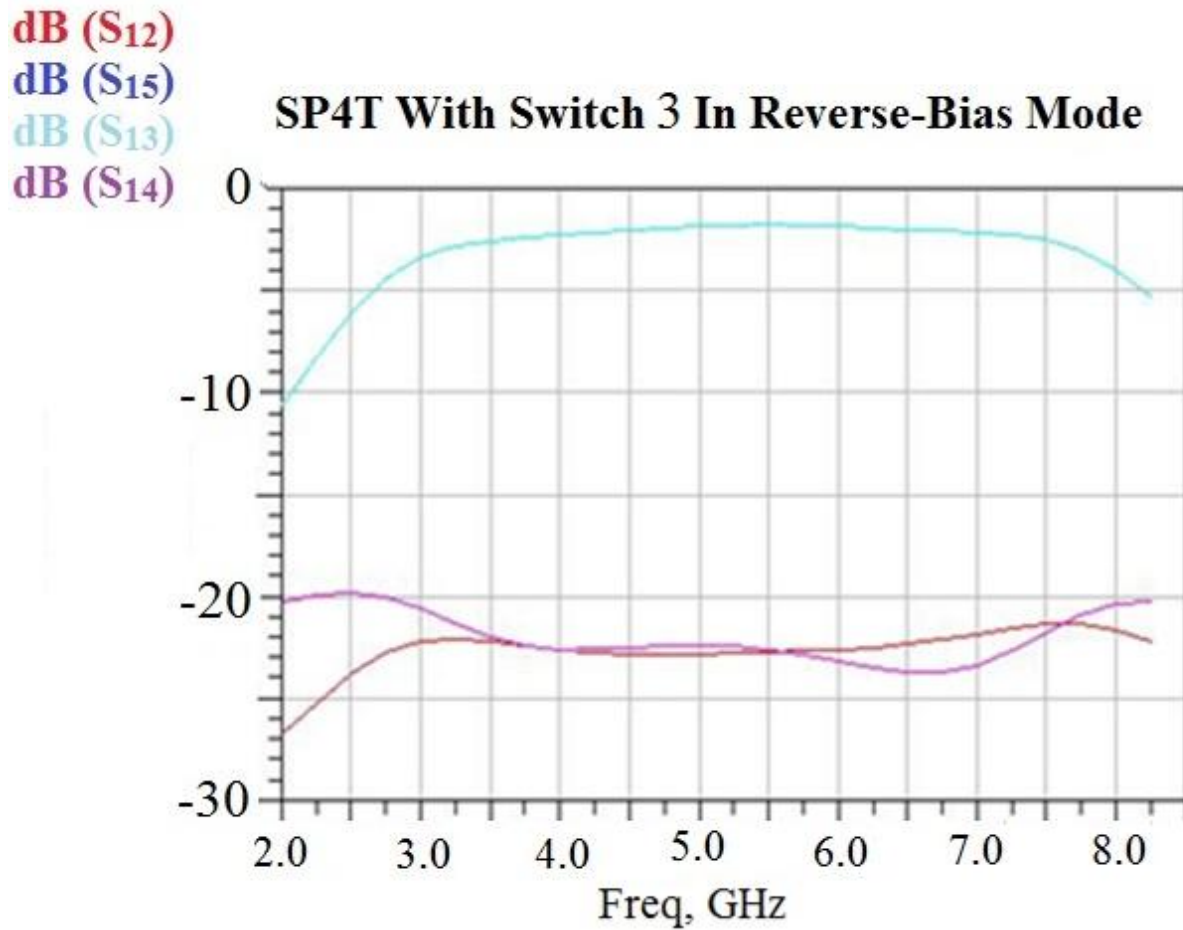


Figure 6.5 - SP4T For Switch 3 Selected

From these figures, it is clear that the SP4T works very well for the desired range of DC through 8 GHz; when the switch connected to Port 4 is selected with the -5V DC bias, the S<sub>41</sub> shows transmission of the signal, while all others are suppressed, and, likewise for the switch at Port 3. In *Figure 6.8*, the data from the HMC345LP3 data sheet shows similar results to the simulations.

# Return Loss

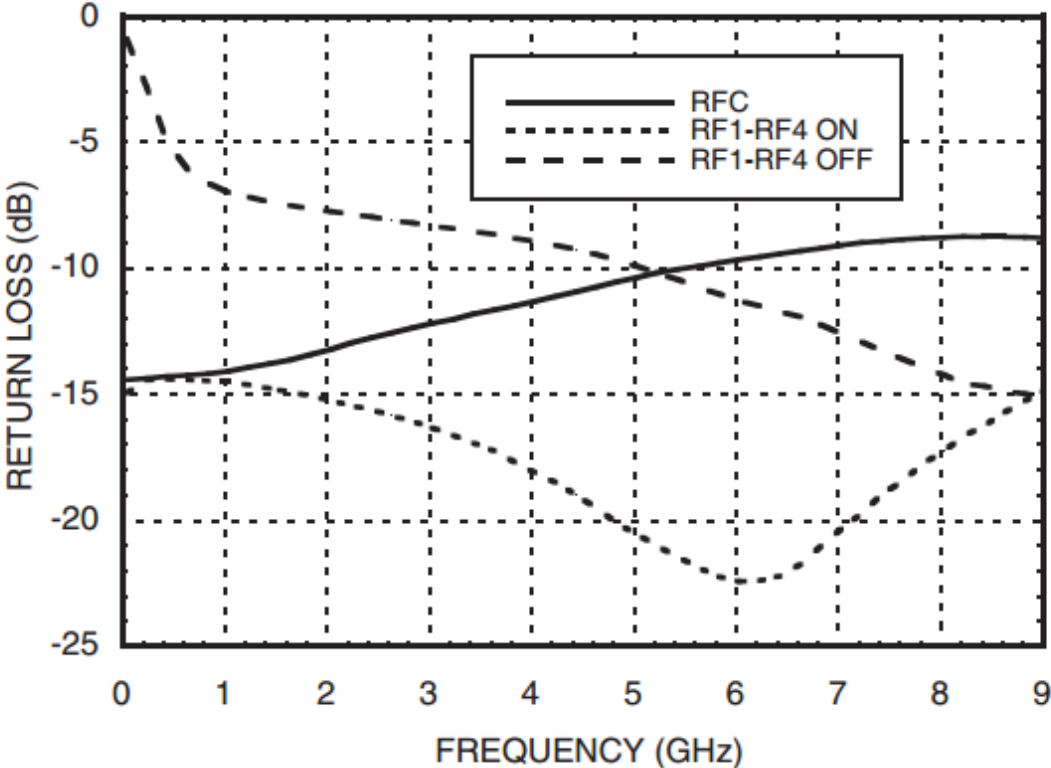


Figure 6.6 - HMC345LP3 Return Loss Parameters from Hittite Microwave Corporation [4]

WORKS CITED

## WORKS CITED

- [1] Pozar, David M. Microwave Engineering, 4th Edition. John Wiley and Sons, 2012.
- [2] Poole, Ian. "PIN Diode Variable RF Attenuator Circuit." Radio-Electronics.com  
<<http://www.radio-electronics.com/info/rf-technology-design/attenuators/rf-variable-pin-diode-attenuator.php>>
- [3] "PIN\_diode (PIN Diode)"  
<[http://edocs.soco.agilent.com/display/ads2009/PIN+diode+\(PIN+Diode\)](http://edocs.soco.agilent.com/display/ads2009/PIN+diode+(PIN+Diode))> Agilent Technologies.
- [4] Hittite Microwave Corporation. "HMC345LP3 Data Sheet." v04.0805.
- [5] "PIN Diodes for Microwave Switch Designs." Macom Technology Solutions. V2.  
<<https://www.macomtech.com/Application%20Notes/pdf/AN3021.pdf>>

## Chapter 7 - System Measurements

### 7.1 - Introduction

After the simulations were completed, the Balanced, Anti-podal Vivaldi (BAPV) antenna was fabricated on Rogers Duroid 6010LM Laminate, which possesses a dielectric constant of 10.2 [1]; such a large dielectric allows for smaller electrical size of the fabricated antenna, which was 8cm x 6.5cm after fabrication. For the initial proto-type of the receiver array, the individual antennas were placed on wooden stands and secured with nylon screws and bolts. To fasten the antenna stands to the array, curved, wooden arcs were cut, along with a linear array, which allows for ease of installation of the antennas. See *Figure 7.1* below for a picture of the initial receiver array. As will be discussed further in the final chapter of this thesis, there is currently a new design almost completed for making the actual array and the antenna stands out of HDPE plastic, which causes slightly lower scattering than the wooden counterpart.



Figure 7.1 - Array Setup

## 7.2 - Antenna Measurement Results

Once the antennas were fabricated, gold-plated SMA connectors provided by Lighthouse Technologies, which has a frequency range of DC-18GHz [2], were soldered onto the feed of the antenna, and then connected to the 8207B Hewlett-Packard Network Analyzer, which operates from 130MHz - 20GHz. Once calibrated, the  $S_{11}$ , or return loss, of the antenna was measured. *Figure 6.2* below shows the results, which very closely match those of the simulated results in the Antenna Simulations chapter of this thesis. From the figure below, the antenna has a return loss lower than -10dB for nearly the entire frequency range from 2.2 to 8.2GHz, or, in other words, nearly a 4:1 bandwidth, outside of a few data points that reach above the -10dB level.

From research, most Vivaldi antennas are designed for much-higher frequency ranges, typically above 8GHz, due to the complexity of the antennas working for a lower frequency. However, using the Rogers/Duroid 6010LM Laminate allowed for this a-typical success in the Vivaldi antenna working at lower frequencies.

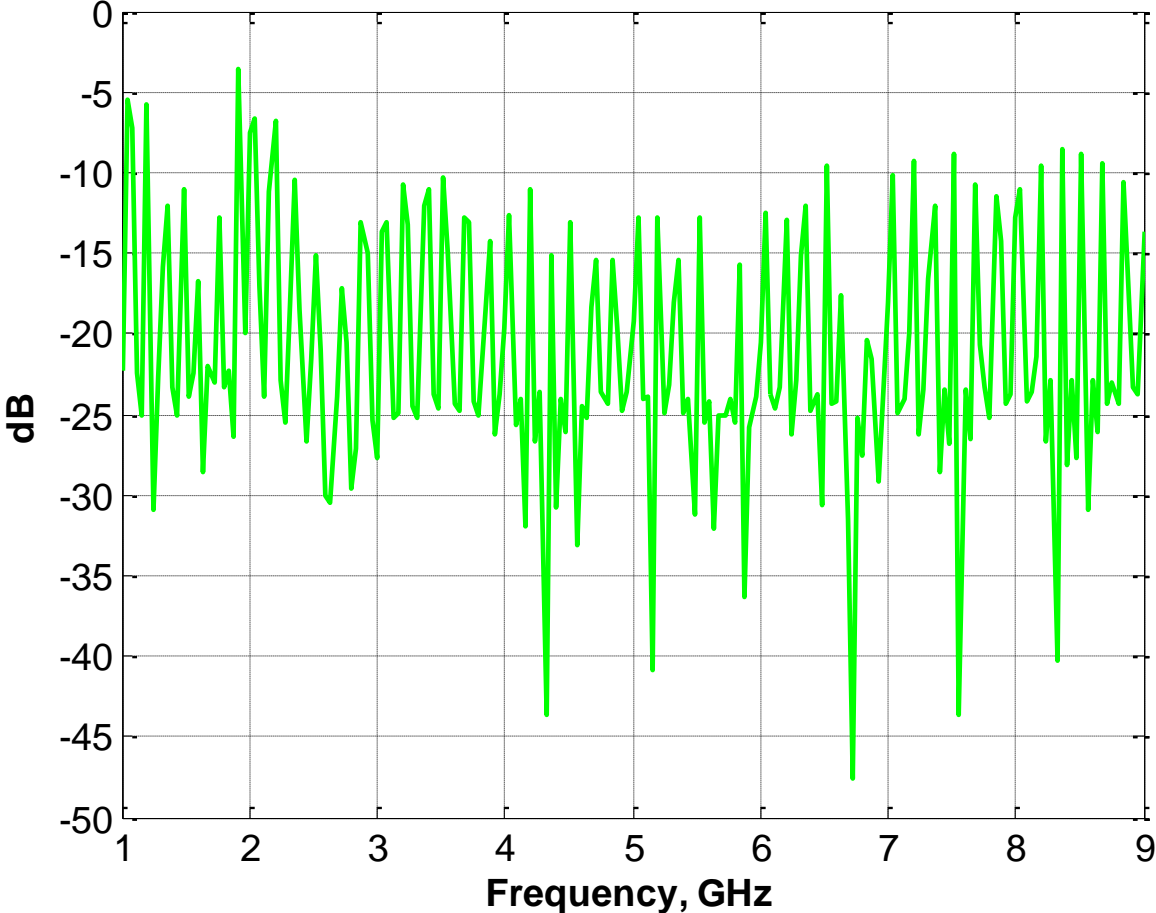


Figure 7.2 - Measured Return Loss of BAPV Antenna

Next, the gain of the antenna was measured by using the Two-Antenna Method; this method is only valid for two antennas that are identical, so several BAPV antennas were used to

ensure that the readings were accurate, in case there were slight differences in the antennas. For the Two-Antenna Method, the following equation is used to determine the gain:

$$G(dB) = \frac{1}{2} \left[ 20 * \log_{10} \left( \frac{4\pi R}{\lambda} \right) + 10 * \log_{10} \left( \frac{P_r}{P_t} \right) \right] \quad (1)$$

Where  $R$  represents the separation between the antennas,  $P_r$  is the power received by the receiving antenna and  $P_t$  is the power transmitted [3]. The following was performed at intervals of 0.5GHz from one through nine gigahertz; the maximum gain occurs at 6GHz, and is 5.2dB, as seen in *Figure 6.3*, which is acceptable for such a small antenna, and is somewhat close to the simulated value of slightly over 7dB, which is common for simulations to not have accurate values for the overall gain of the antenna.

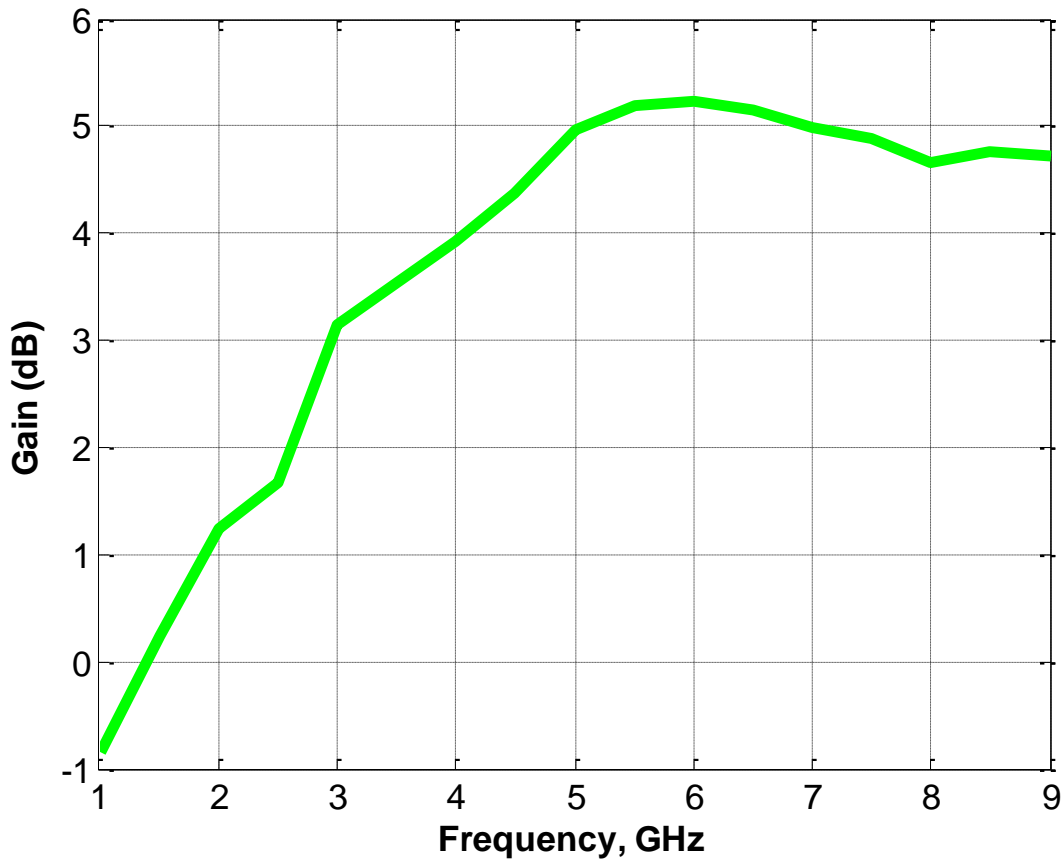


Figure 7.3 - Measured Gain of BAPV Antenna versus Frequency

The next step was to measure the radiation pattern to see how closely it matched the simulated pattern. To do this, the BAPV receiver array was used to measure the transmitting antenna, and then a polar plot was created through MATLAB. At 6GHz, the radiation pattern was captured in *Figure 6.4*; while only a limited-number of receivers were used to capture the radiation pattern, it very closely matches that of the simulated radiation pattern presented in Chapter 3, in that there is one main side-lobe, and several side-lobes, but with much lower levels of power. The measured beam pattern is also nearly symmetric. One option that has been briefly explored with this receiver array is to use it for the purpose of beam-scanning, which, based on the phase applied to the antenna at the receiver end, would allow the beam to be moved

over an area. Doing so would require phase-shifting circuits which can be created from PIN diodes, and would allow for fewer antennas to be used in the array, as well as less angular coverage. With the narrow beam, this ensures that in our current set-up, we would only be obtaining the scattered field that is closest to the desired antenna, instead of obtaining a much-wider range; hence, this is one of the main reasons why a Vivaldi-type antenna was chosen over something like a patch antenna, which has a very wide beam-width, and can therefore receiver unwanted data and clutter.

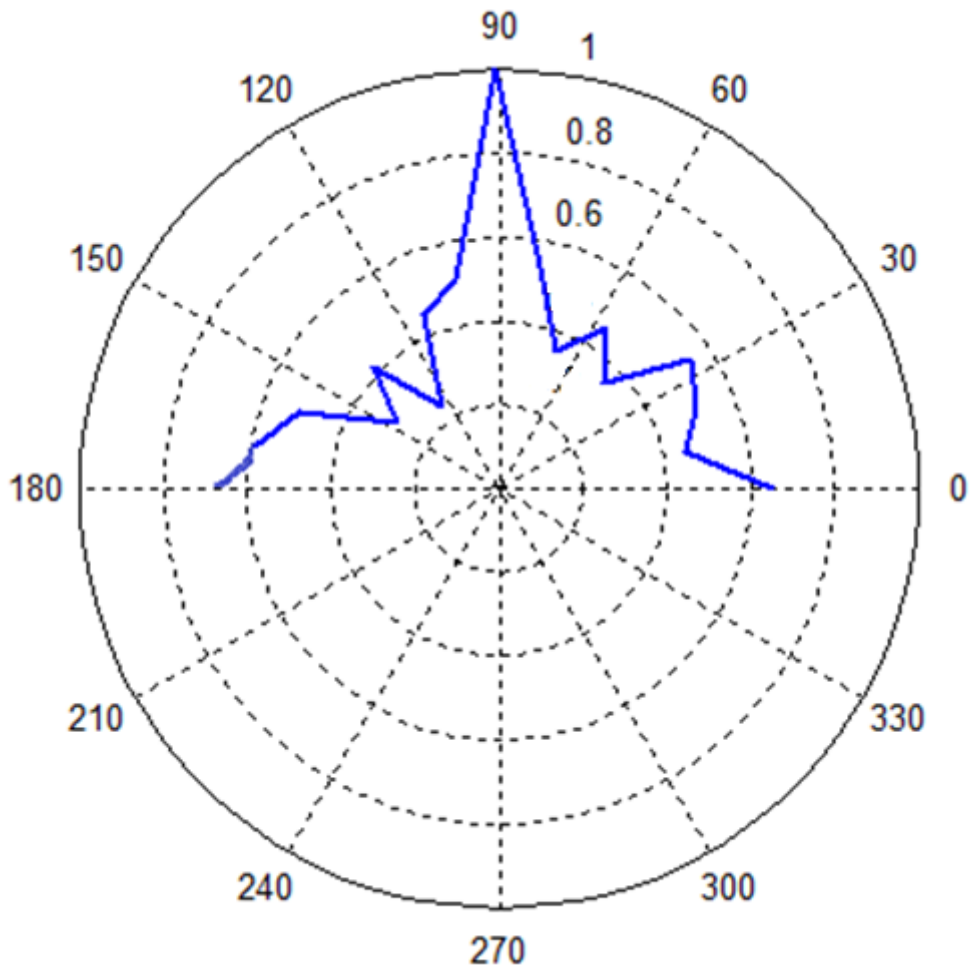


Figure 7.4 - Measured Radiation Pattern of BAPV Antenna

### 7.3 - System Measurements of Microwave Switch

The next step in the measurement process was to measure, without an antenna, the transmission, or  $S_{21}$ , of the signal from the source through the network of the microwave switches. In *Figure 7.5* below, the green data points indicate the signal that was transmitted through the level of switches when the specific antenna and switch were selected. (Note, the antenna was selected, but instead of having the coaxial cable connected to the antenna, it was connected from the output of the first microwave switch that was joined Port 1 from the VNA to Port 2.) And the blue data points represent the transmitted signal through the system of microwave switches when a different antenna was selected; one of the largest concerns of this system was how the data read from other antennas would interfere with each other when only one antenna at a time is being read from. Clearly, the low-levels of power transmitted through show that there is little interference from the antennas that are not selected when the data is being transmitted to the VNA. *Figure 7.6* shows the results provided by Hittite Microwave for the isolation from one antenna to another when one antenna is selected. One step that can be taken to reduce this level even further, however, is to purchase EMI-shielding devices, which is discussed in the last chapter of this thesis.

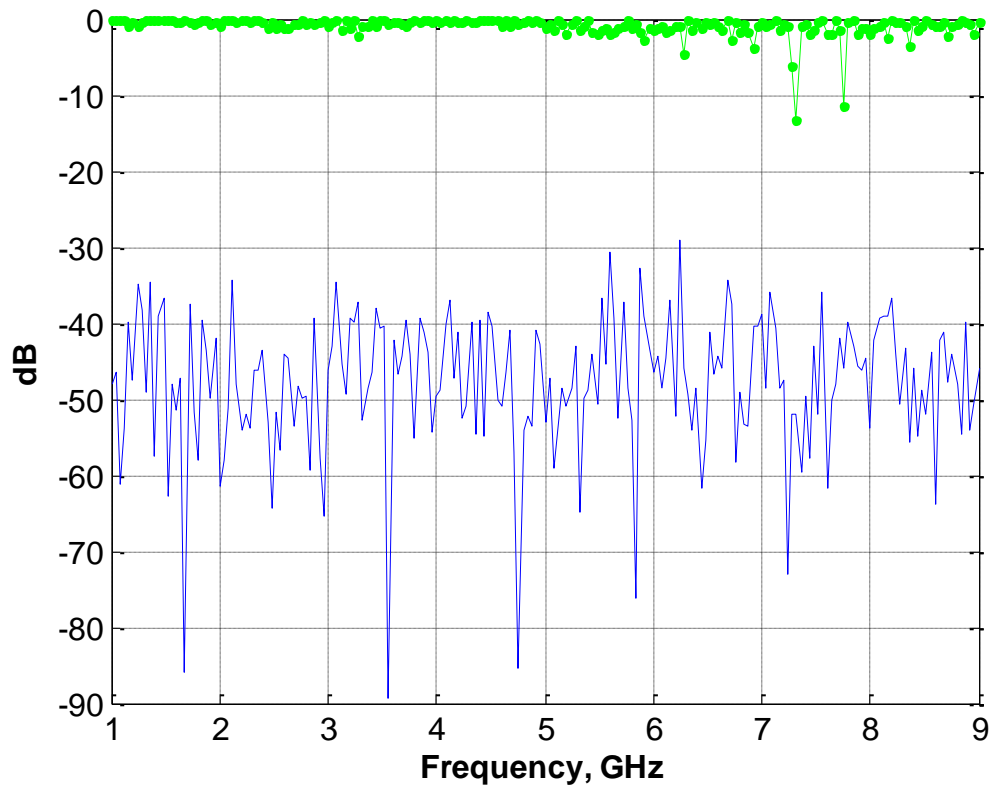


Figure 7.5 - Transmitted Signal through Selected and Un-Selected Series of Microwave Switches

## Isolation

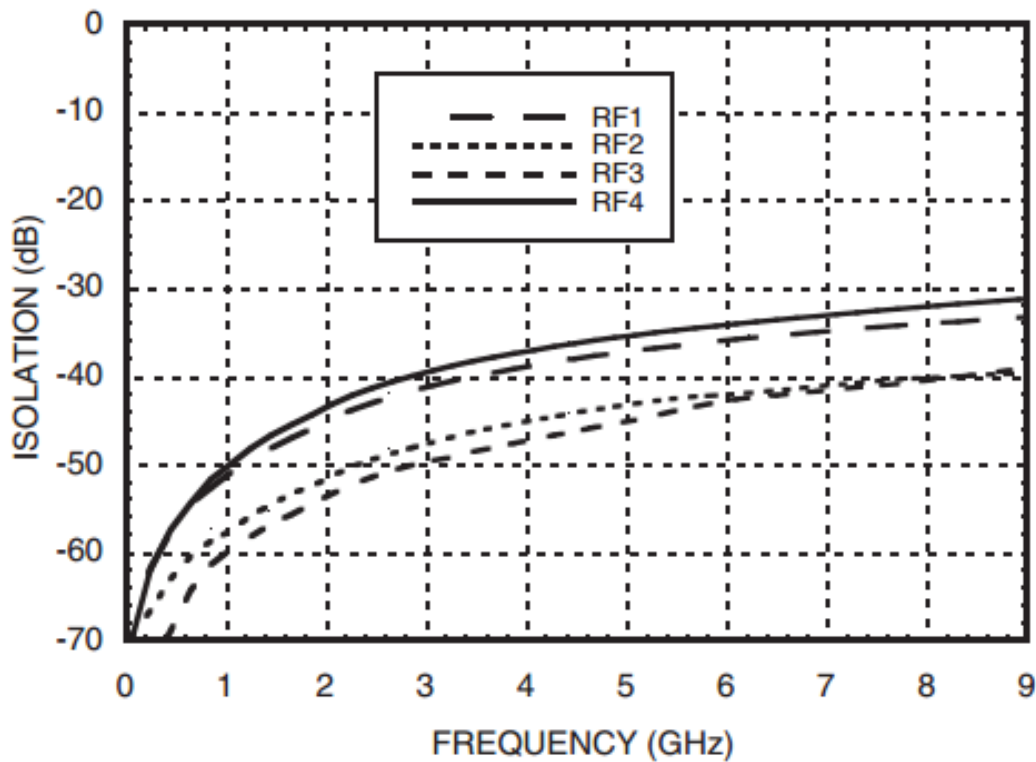


Figure 7.6 - Isolation Between Switches from Hittite Microwave Data Sheet [4]

### 7.3 - Polarization Measurements of Receiver Array Antennas

Before beginning the process of using the antennas for the purpose of imaging, the polarization of the antennas was to be tested to ensure that the electric and magnetic fields were not interfering with each other, in other words, that the cross-polarization levels of the antennas were low. From Chapter 3 of this thesis, it was mentioned that one of the reasons for choosing the balanced, anti-podal Vivaldi design over other Vivaldi antennas, such as the anti-podal Vivaldi, was due to the fact that the shared feed-line of the anti-podal Vivaldi created large levels of cross-polarization. While the balanced, anti-podal Vivaldi antennas inherently possess low levels of cross-polarization [5], a polarizing filter was built, see *Figure 7.7* below, to test how

well this system was working. To build an electro-magnetic polarizer, thin wires need to be placed at least  $\lambda/10$  apart from each other. Then, the filter is placed in front of either the source or receiving antenna. Doing so will, based on the rotation of the filter, block the electric-field radiation from the antenna, and, if rotated by  $90^\circ$ , will allow transmission of the electric field of the source to the receiver. In *Figure 6.8* below, the solid (blue) line represents the signal where there is no filter placed in front of the source, the dashed (red) line represents the signal with the polarizer placed in front of the source and the dot-dashed (green) line represents the signal with the polarizer rotated by  $90^\circ$ . From this figure, it is seen that the signal obtained by the receivers, the solid line, is nearly the same as the signal obtained with the filter placed in front of the source, but this does not block the electric field from propagating, as the wires do not obstruct their propagation due to the polarization of the electrical field aligning with the direction of the wires. However, for the dot-dashed (green) line, the polarizer was rotated by  $90^\circ$ , and the level of the transmitted signal is much lower, hence the rejection of the electric field by the filter, based on the orientation of the wires being smaller in electrical size, and therefore able to block the E-field from propagating. In taking the average value of both signals, there is roughly 12dB of polarization contrast between the electric and magnetic fields of the antennas, which proves the research completed in [5] that balanced, anti-podal Vivaldi antennas have very low cross-polarization.

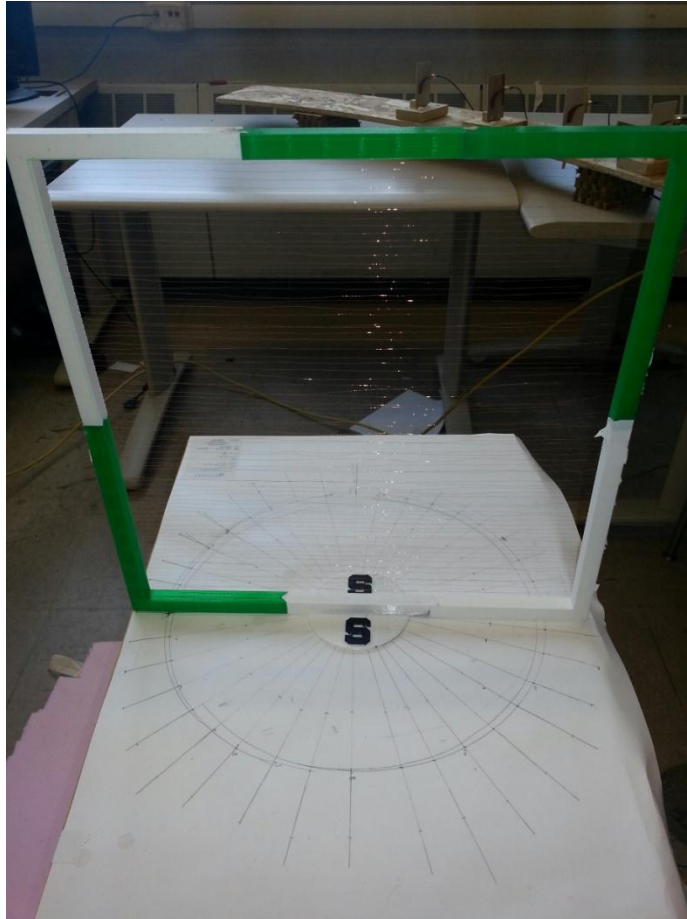


Figure 7.7 - Polarizing Filter

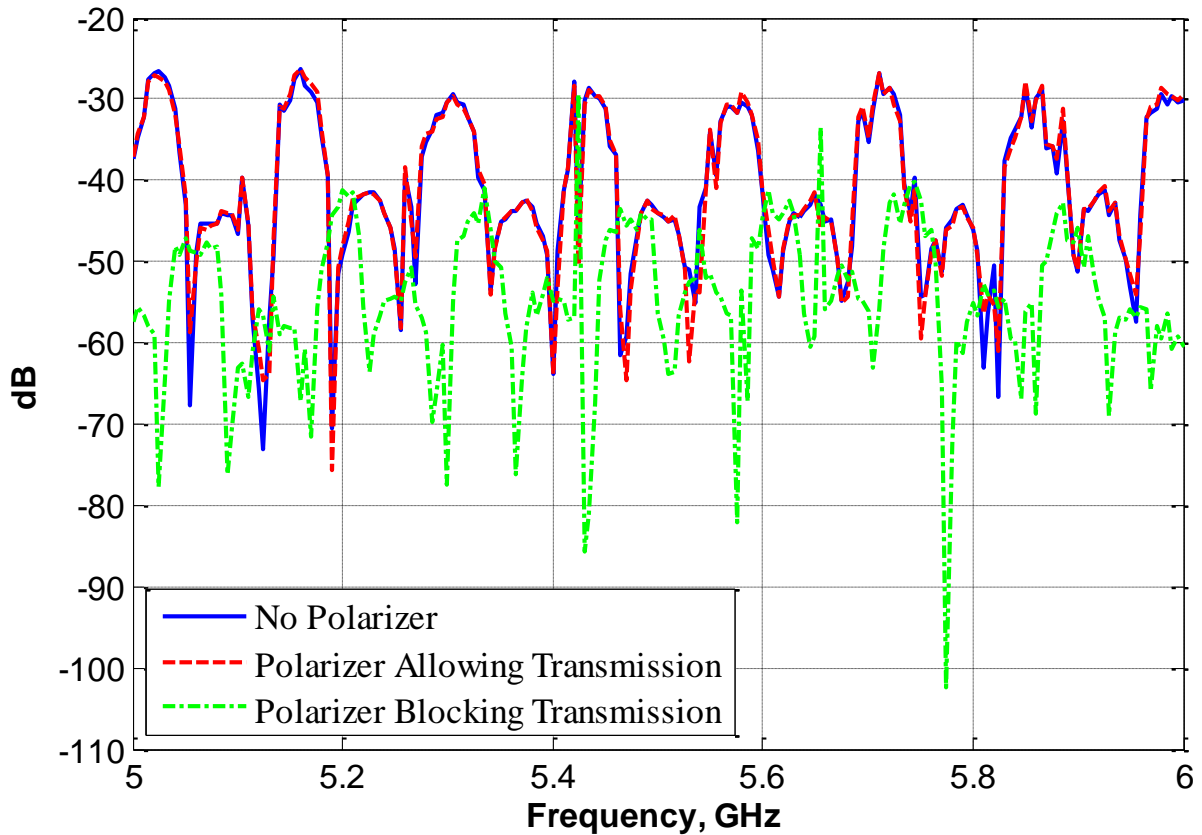


Figure 7.8 -Polarizing Filter Effect on Signal Transmitted from Source

#### 7.4 - Complete System Measurements

With the system function as intended, the next step was to test the entire system with the goal of limited-angle reconstruction in mind. While this is currently still being resolved, as will be discussed in the final chapter of this thesis, initial results show that the antenna array is able to distinguish between different dielectric materials, which is the requirements that this array needs; the only step keeping this array from obtaining being able to use the MSFBPP code to reconstruct more-complex objects outside of cylinders, is more antenna readings. Once we are able to operate at a higher sampling rate, we can combine the weakly-scattering dielectric materials and try to reconstruct them and observe the differences in contrast in the reconstructed

image; for example, we could use the cylinder with defect, and place an object with different dielectrics inside of the defect, and with the reconstruction, see how the contrast ratio differs between the boundary of the two objects. This would be very applicable to something along the lines of cancer detection, as the material difference between healthy and malignant tissues would need to be detected. After showing some scattered field readings for simple objects, a comparison will also be shown that will demonstrate the ability of the receiver array to distinguish between two different dielectric materials; some that present a very high contrast, and some that have very close values of permittivity.

Initially, readings were taken of a dielectric cylinder made of out delrin, which possesses a dielectric constant of around  $\epsilon = 3$ ; the object was placed slightly less than half-way between the source and the receivers, meaning that it was slightly closer to the receiver array, so that the entire scattered field would be able to be captured. First, however, since we are finding the scattered field, which, again, is based off of the following equation:

$$\mathbf{E}_{scat} = \mathbf{E}_{tot} - \mathbf{E}_{inc} \quad (1)$$

Where  $\mathbf{E}_{tot}$  is the total electrical field, which is measured without the cylinder in place, which allows us to account for the stand and the other objects that are included in the imaging array that we do not wish to consider for reconstruction purposes, and then the  $\mathbf{E}_{inc}$  field is the data that is being collected with the scattering object in-place.

For the simple dielectric cylinder, *Figure 6.7 and Figure 6.8* below show the absolute values of the scattered field; as can be seen from these figures, they are very symmetric about the center sensor position, indicating that the object being imaged is itself symmetric. Also, the highest peak of both of the plots occur at the middle sensor position, which indicated that the

highest level of scattering occurred at this point, and that the scattering tapers off as the receivers are placed farther away from the cylinder. This cylinder is roughly two-wavelengths in electrical size, at 6GHz.

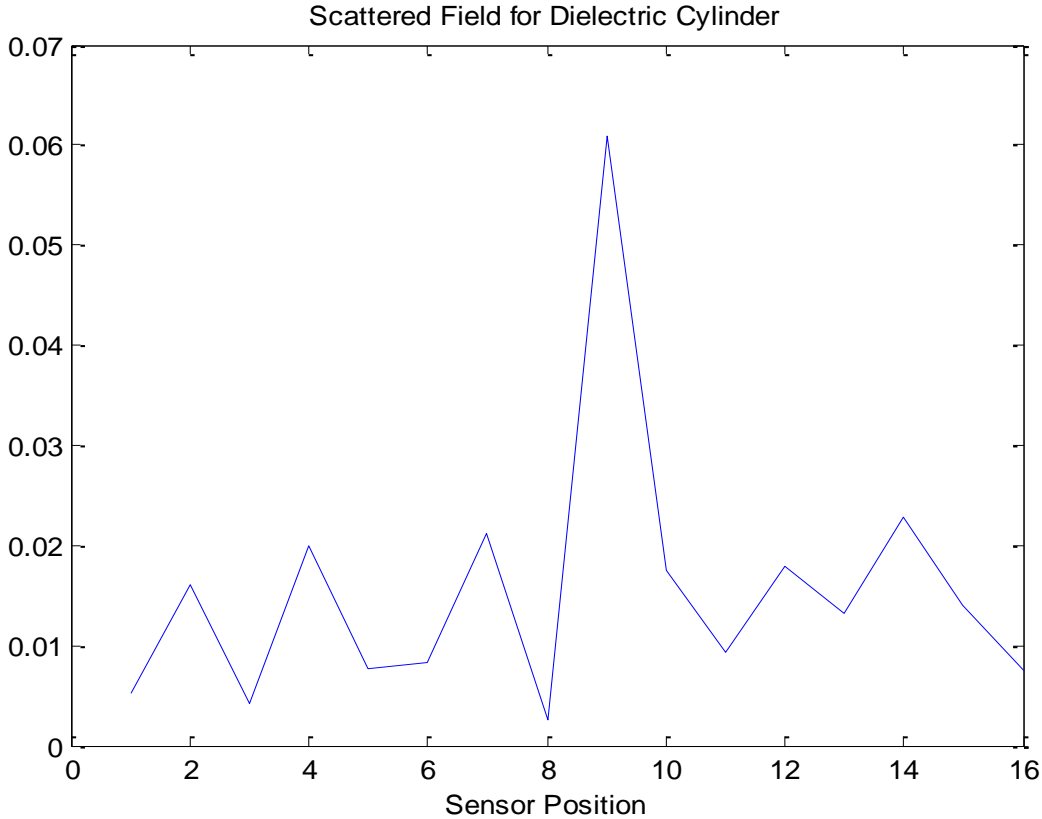


Figure 7.9 - Scattered Field of Dielectric Cylinder for 0°-Rotation

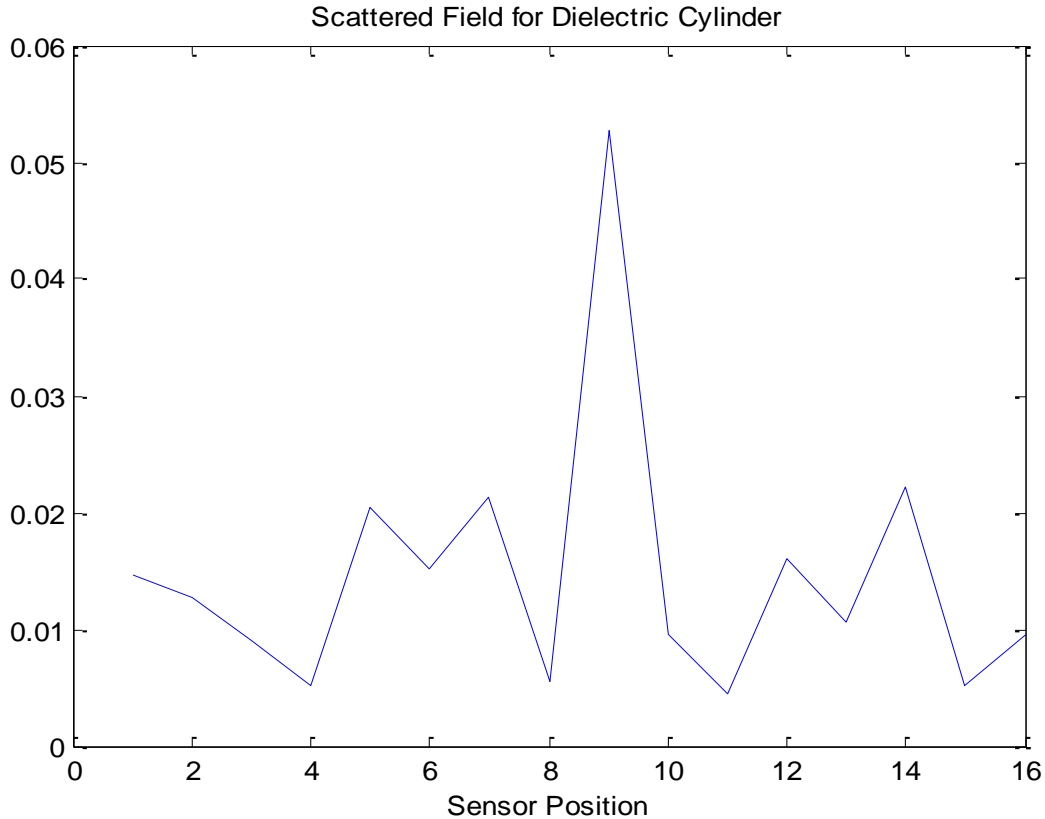


Figure 7.10 - Scattered Field of Dielectric Cylinder for 90°-Rotation

In the research process, before it was determined that more receiver positions were required, the MSFBB was yielding very similar results in reconstructing circles, squares and cylinders with defect. Because of this, one approach to ensure that the antennas were actually obtaining the correct data was to obtain the scattered fields for the cylinder, but in this case, the cylinder would be off-centered, and rotated around a point for 10° increments. The scattered field measurements are presented below in *Figures 7.11 and 7.12*, and the reconstructed results will be presented later in this chapter, as a verification that we are indeed able to detect the location of an object that is not directly in-between the path of the source and middle receiver position.

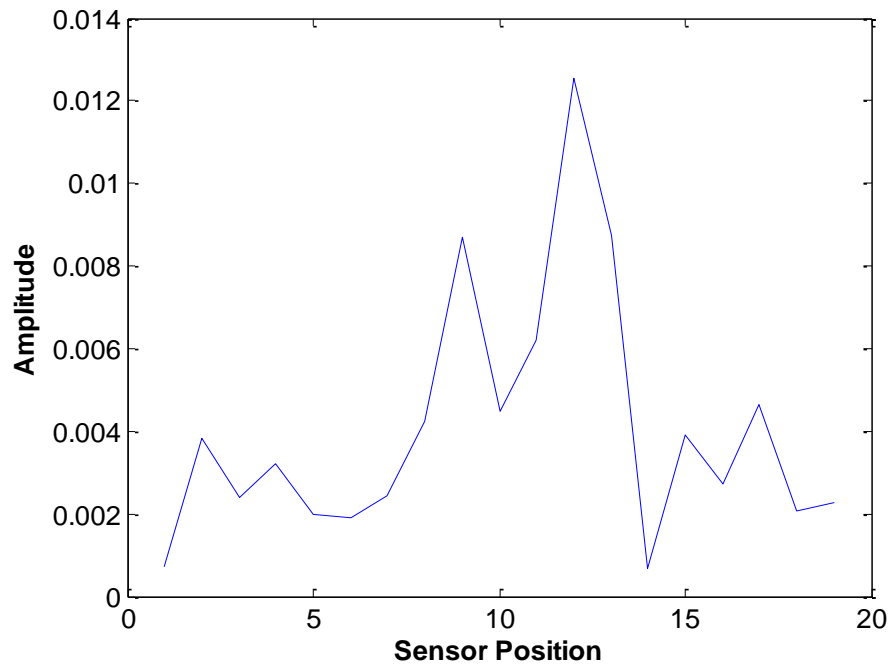


Figure 7.11 - Scattered Field of Off-Centered Circle 0° Rotation

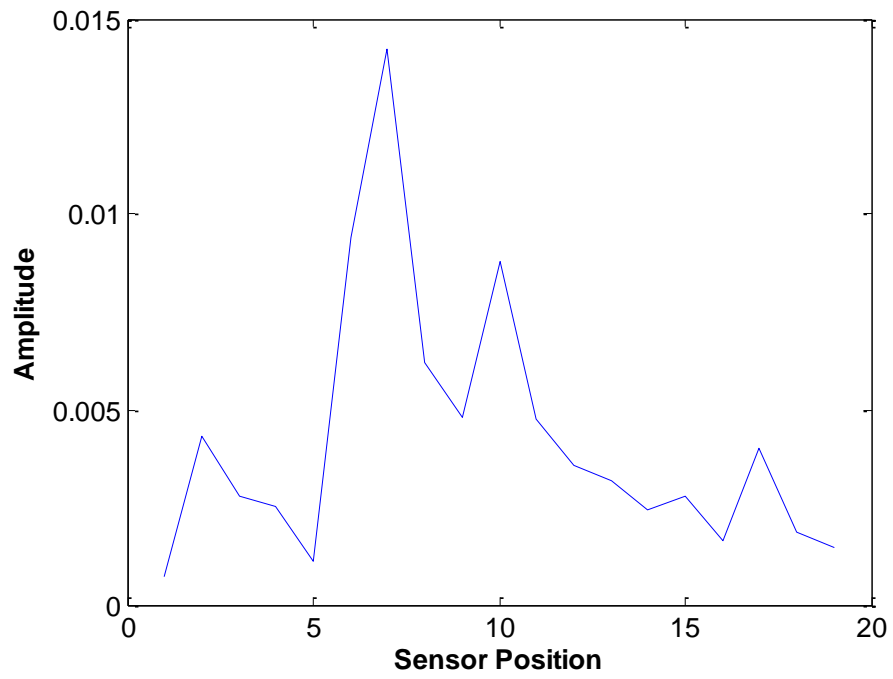


Figure 7.12 - Scattered Field of Off-Centered Circle 180° Rotation

Clearly, these scattered-field plots are nearly symmetric around the center sensor position, and show that the array can not only detect an symmetric object located in the center of the source and receiver array, but also one that is located off-center.

The next step was to obtain the scattered-field plots for a dielectric square cylinder, roughly two-wavelengths in electrical size at 6GHz; while the reconstruction results via the MSFBPP algorithm need more data points because of the un-symmetric nature of this object, the scattered field plots show that for symmetric angles, namely  $0^\circ$  and  $90^\circ$ , and, with a square exhibiting  $90^\circ$ -symmetries, one would expect that the scattered-field plots are identical, and, as *Figures 7.13 and 7.14* show, that are nearly the same.

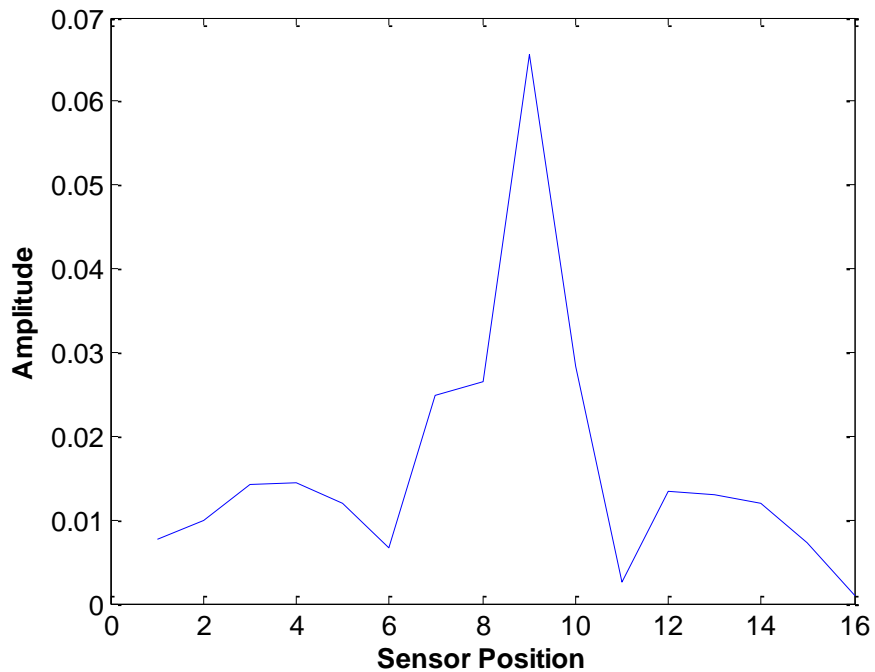


Figure 7.13 - Scattered-Field Plot for Dielectric Square at  $45^\circ$  Rotation

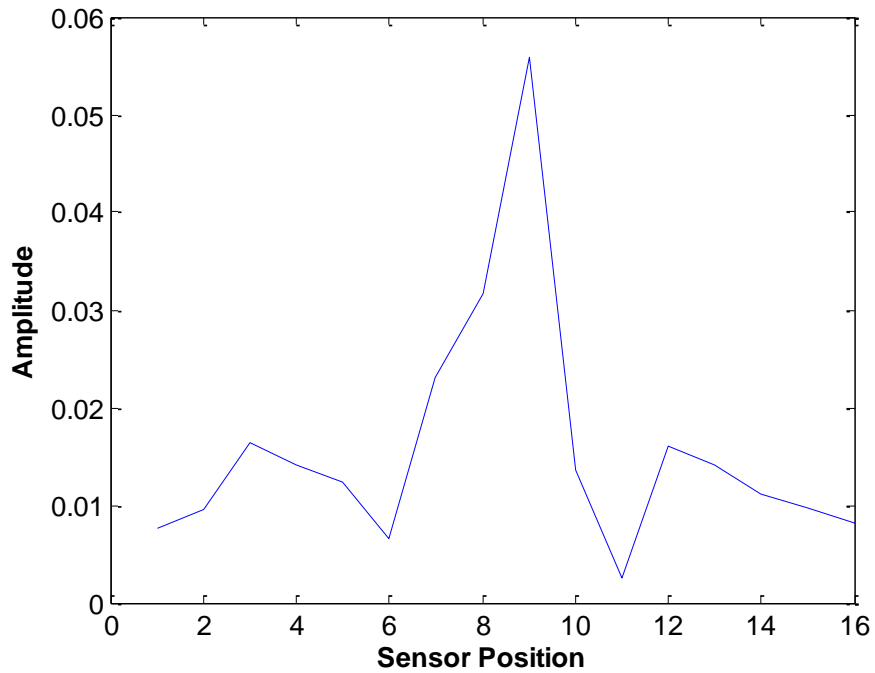


Figure 7.14 - Scattered-Field Plot for Dielectric Square at 135° Rotation

With the array able to detect larger objects, such as the circle and square cylinders, the next step was in seeing what smaller objects the array could detect. To do so, a circular cylinder with a notch in it, as seen in *Figure 6.15* below, was used to see how the scattered field would differ from that of the regular circle. The dimensions of the notch are (at 6GHz), roughly one-wavelength wide by half-wavelength deep. If able to detect the differences between these two objects, the array could justifiably be used to find cracks in materials, among other non-destructive evaluation tasks.

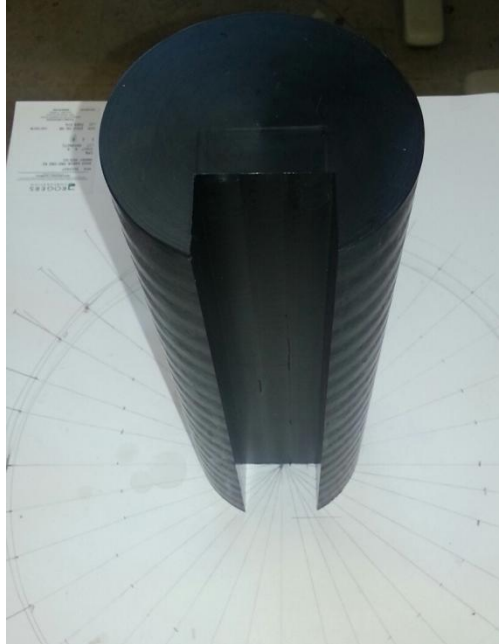


Figure 7.15 - Cylinder with Defect

*Figure 7.16 and 7.17* below show the measured scattered fields for an incident beam with the cylinder rotated at  $0^\circ$  and  $180^\circ$ ; at  $0^\circ$  the defect, which causes scattering, is on the left-side of the cylinder, and closer to the receiver positions that are less than the ninth element. For the cylinder rotated to  $180^\circ$ , the defect is on the right-side of the cylinder, which is closer to the receiver elements that are the tenth receiver element and higher. From the two figures below, it is clear that the defect causes the scattered field to be higher on the left side of the receiver arc if the defect is on the left side ( $0^\circ$ -rotation) and likewise for the defect located on the right side of the cylinder ( $180^\circ$ -rotation).

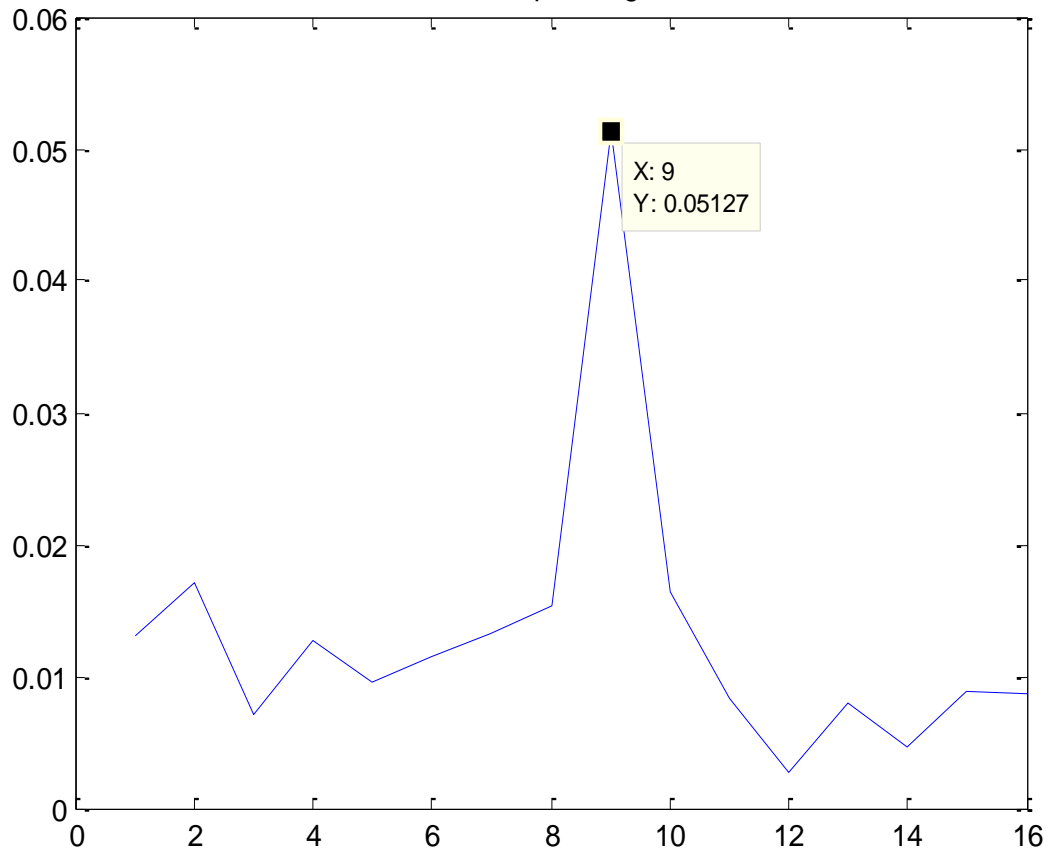


Figure 7.16 - Scattered Field Plot for Cylinder with Defect at 0°-Rotation

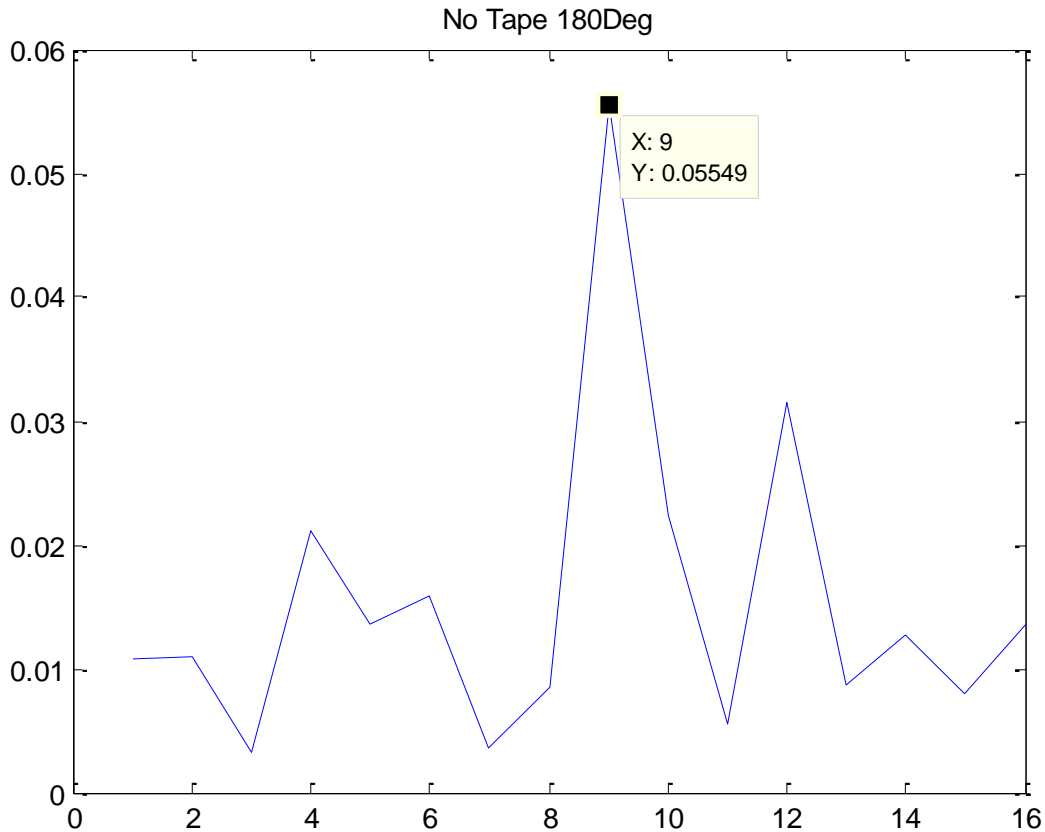


Figure 7.17 - Scattered Field Plot for Cylinder with Defect at 180°-Rotation

Now that it was confirmed that the array was able to detect defects in a material, at least in terms of comparing the scattered fields, the next step was to determine what different dielectrics the array could detect. With human tissue, for example, the dielectric differs between that of healthy tissue versus cancerous tissue, so the next step with the array was to see what different dielectrics could be detected by the receiver array.

First, copper sheet metal was placed inside the defect of the cylinder, and several measurements at different angular rotations were taken. While this data is not able to be used in the image reconstruction process, because the Born Approximation only holds for weakly-

scattering objects, it was done to see what scattered field, if any, was detected. *Figures 6.18 and 6.19* below show the difference in the absolute plots of the scattered fields, and show that there is a difference of roughly 25% between the amplitude of the two plots. From this, it is evident that the array does not obtain the scattered field, as it is reflected away from the receivers.

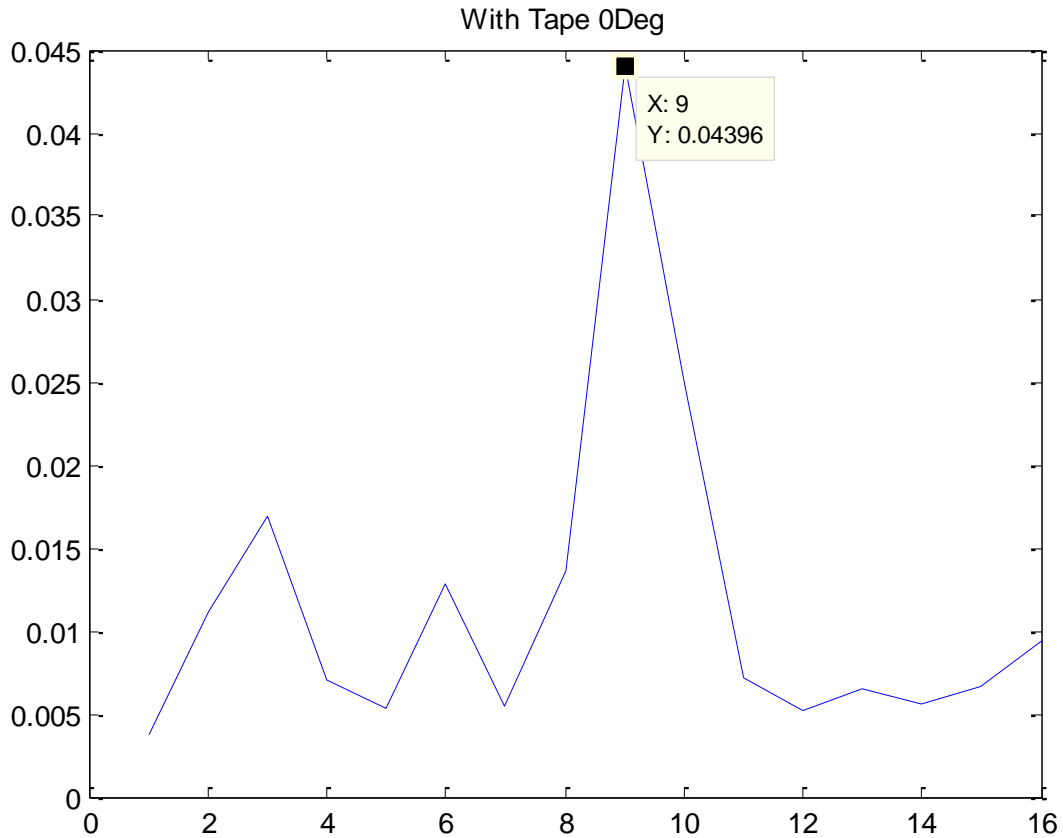


Figure 7.18 - Absolute Plot of Scattered Electric Field for Cylinder with Copper Sheet Metal

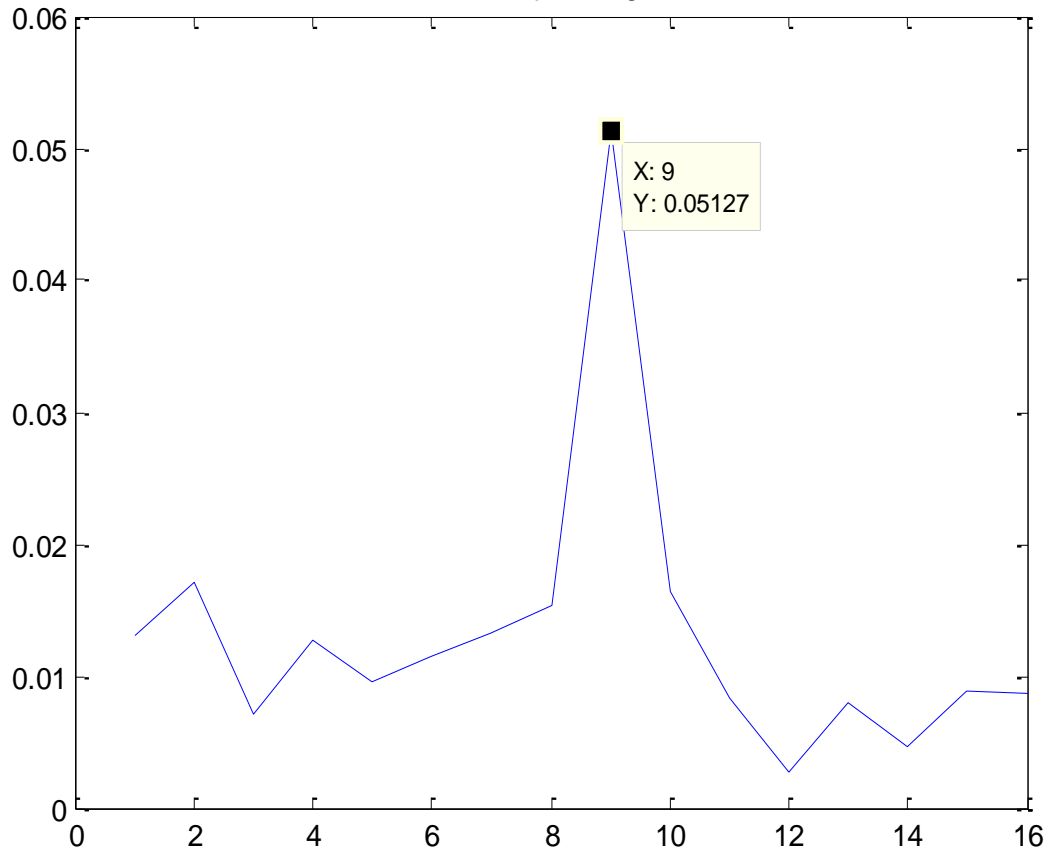


Figure 7.19 - Figure 6.18 - Absolute Plot of Scattered Electric Field for Cylinder

For water, which has a dielectric constant of around 80, the same experiment was conducted, and *Figures 6.20 and 6.21* show the plots of the scattered field with and without water. A relative difference of 4.9% difference was obtained.

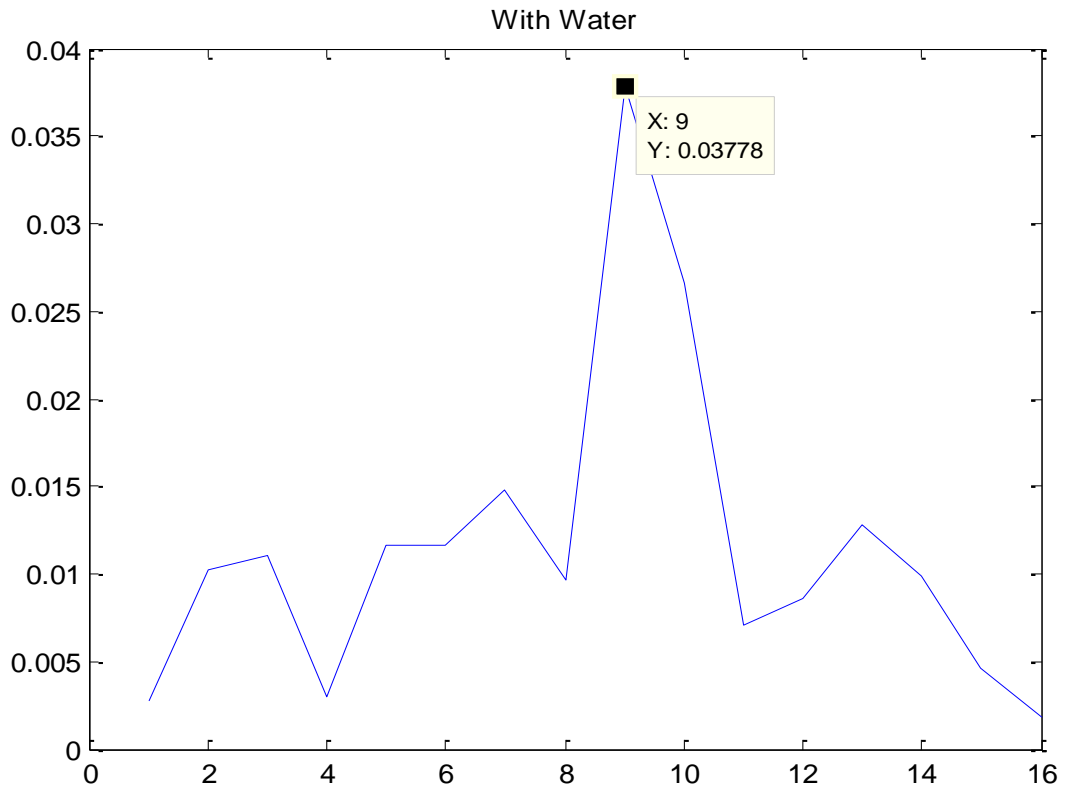


Figure 7.20 - Scattered Field of Cylinder with Water in Defect

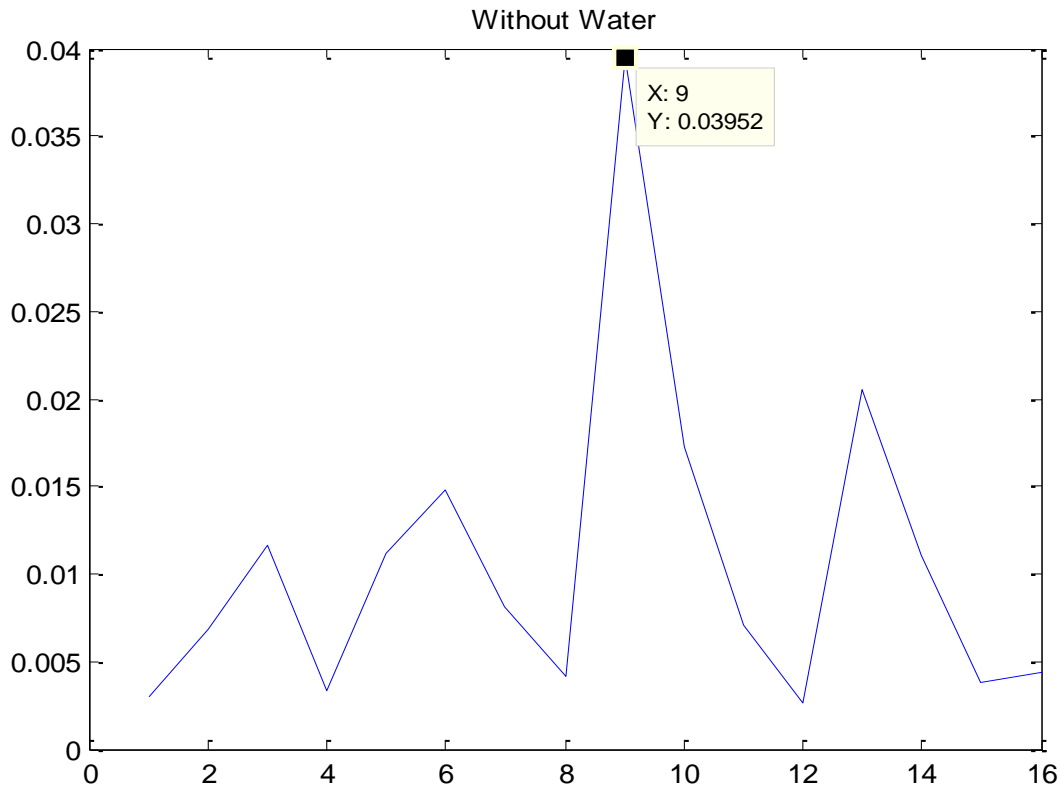


Figure 7.21 - Scattered Field of Cylinder

Following the same method, plexi-glass and wet wood, which have dielectric constants of 3.2 and 20, respectively, the scattered fields with the material coupled with the cylinder and without the material, were measured. *Figure 6.22* shows the differences scattered field detected by the receiver array. Again, these plots are using the absolute data, a combination of the real and imaginary parts, to describe the difference in the fields obtained. So, in the plots where the peak is present at the ninth antenna position, since this is the absolute value being shown, actual value is a negative complex number that actually shows that there is very little scattered field measured at that point. Viewing a plot without it being displayed in absolute format is difficult to understand, so that is why these have been presented in this form.

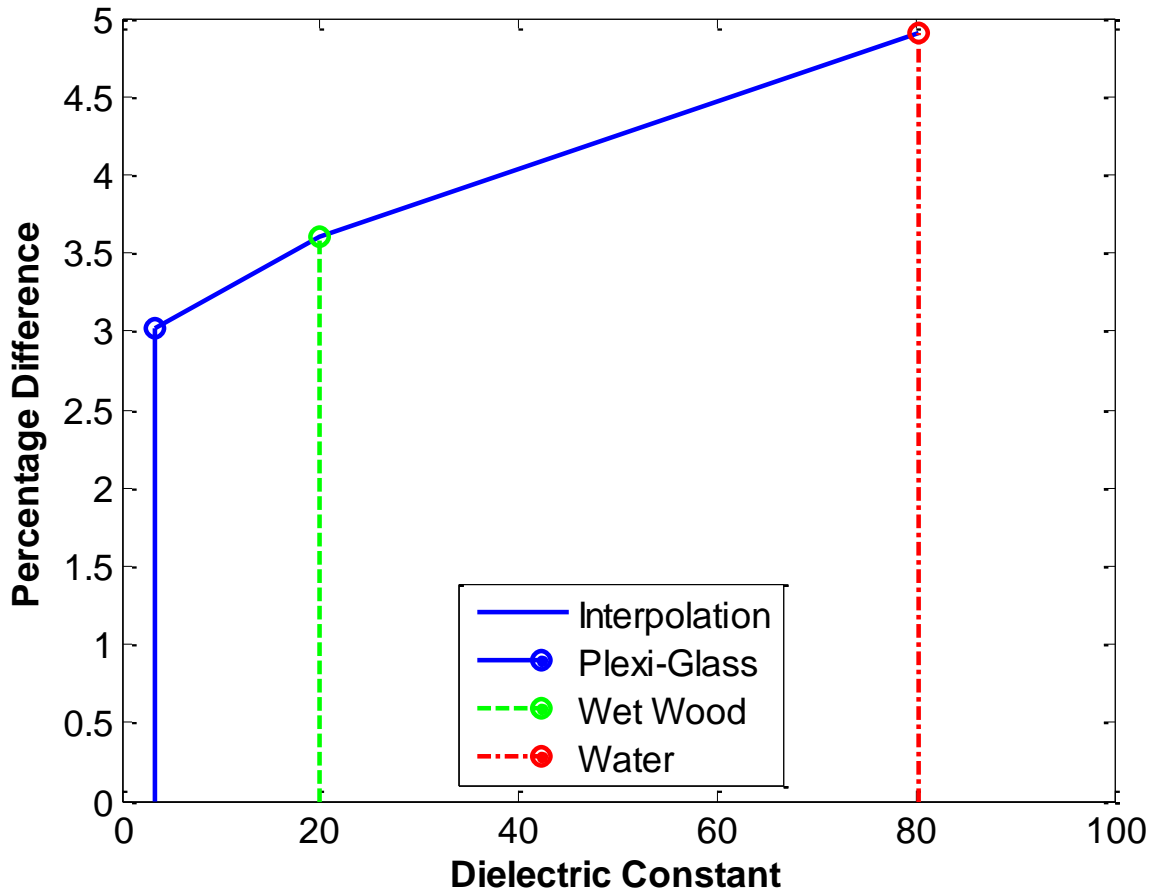


Figure 7.22 - Plot of Permittivity Versus Percentage Difference of Scattered Fields

### 7.5 - Initial Reconstruction Results

As mentioned earlier in this thesis, the reason that the reconstruction code, the MSFBPP algorithm, did not work very well with this data was due to the fact that the data was collected with a number of antennas that was too small. However, for objects that are symmetric from every angle, namely a circle, the image reconstruction results showed some initial results that are very in shape and size to the original object. In *Figures 7.9 - 7.12*, the scattered field results were presented for a dielectric cylinder and an off-centered dielectric cylinder, and here, the reconstructed results will be shown. To obtain *Figure 7.23*, projections were taken at  $20^\circ$

increments for a coverage of  $270^\circ$ . To verify that this results was accurate, the dimensions in terms of pixels of the reconstructed image were converted to into a wavelength, and the size of the reconstructed cylinder was found to be less than 1cm different than that of the physical cylinder. The ripples that are prevalent in the image disappear as more samples are taken per angle.

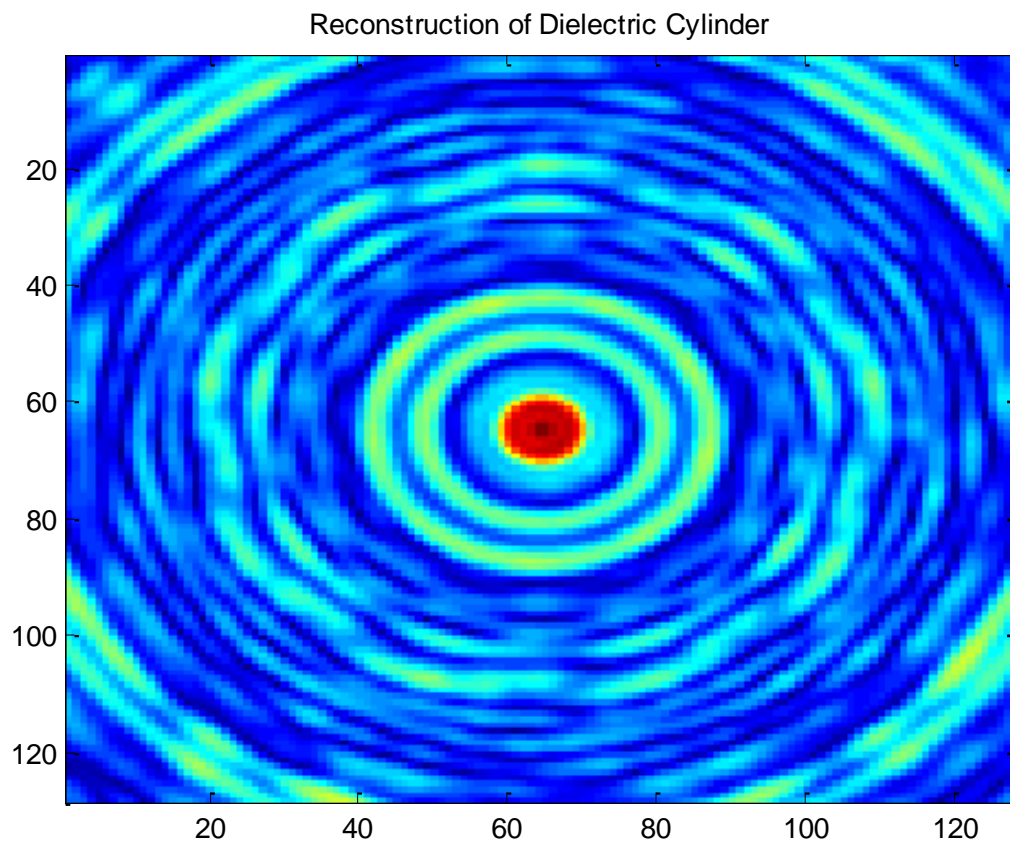


Figure 7.23 - Initial Reconstruction Results of Dielectric Cylinder

For the off-centered circle, as outlined above, the cylinder was rotated around a central point, and a projection was taken every  $10^\circ$  for a total of  $270^\circ$  of coverage. While the image does appear to be washed-out, the center of the cylinder was found to be 20 pixels away from the origin, and converting those pixels to wavelengths, the distance from the origin to the

reconstructed cylinder was very close to the physical distance from the central point to the location of the actual cylinder.

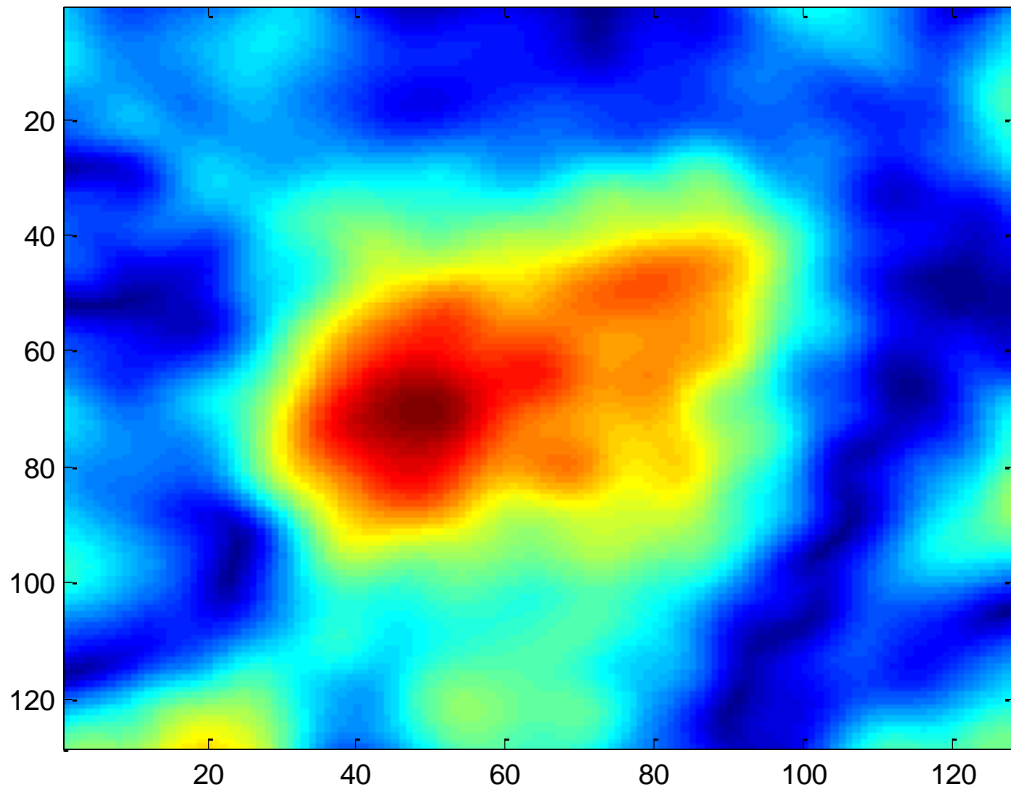


Figure 7.24 - Initial Reconstruction of Off-Centered Cylinder

WORKS CITED

## WORKS CITED

- [1] RT/Duroid® 6006/6010LM High Frequency Laminates. Rogers Corporation. Data Sheet 1.6000 < <http://www.rogerscorp.com/documents/612/acm/RT-duroid-6006-6010-laminate-data-sheet>> Last Accessed August 2013.
- [2] Lighthouse Technologies. "*SMA Vertical Thru-Hole Jack Connector*." <<http://www.rfconnector.com/sheets/SASF54GT.pdf>> Last Accessed 2013.
- [3] Caverly, Robert. "*Antenna Measurements*." Villanova University. <<http://rcaverly.ee.vill.edu/crcd/ant-measure/measure.pdf>> Last Accessed August 2013.
- [4] Hittite Microwave Corporation. "*HMC345LP3/345LP3E Data Sheet, v04.0805*." <[http://www.hittite.com/content/documents/data\\_sheet/hmc345lp3.pdf](http://www.hittite.com/content/documents/data_sheet/hmc345lp3.pdf)> Last Accessed August 2013.
- [5] Garg, Ramesh, et. al. "*Microstrip Antenna Design Handbook*." Artech House, 2001.

## Chapter 8 - Conclusions and Future Work

### 8.1 - Summary

As made clear in the results presented in this thesis, the antenna array system works well for identifying different contrasts in materials and objects, but further steps need to be taken to allow for the minimal-scan filtered back-propagation code to be fully-integrated with the system. From generating simulated scattered electromagnetic field data, and subsequently running that data through the MSFBPP code, it was determined that the present number of antennas that are used in the system, 19, are not enough to fully reconstruct more-complex objects with limited-angle coverage. Simple object with symmetry, such as a cylinder, are able to be reconstructed with recovering almost exactly the correct dimensions, but objects such as cylinders with defects or squares simply need more antennas per reading to collect the scattered data.

At a frequency of 3GHz, the spacing between the antennas of the array was roughly two wavelengths, while the objects being imaged were one-wavelength in electrical size. Likewise, when the frequency of imaging was set to 6GHz, while the electrical size of the objects became near to two wavelengths, the spacing between each antenna rose to four wavelengths. And, based upon the Nyquist criterion, sampling must occur at intervals of at least  $\lambda/2$  to avoid aliasing. With the linear array, up to 64 readings per view were taken, but this was done shifting the array manually, and introduced error from doing so. At 6GHz, at least 128 readings per reading must be taken, and since placing the antennas that close to each other will cause loading effects which will drastically alter the data obtained, a linear shifting array is currently being fabricated that will allow for motor control via LabVIEW that is capable of shifting the array in small, accurate increments, which will allow for the full number of sensors to be obtained per

reading. The results below from the generated scattered data show that more antenna readings are required.

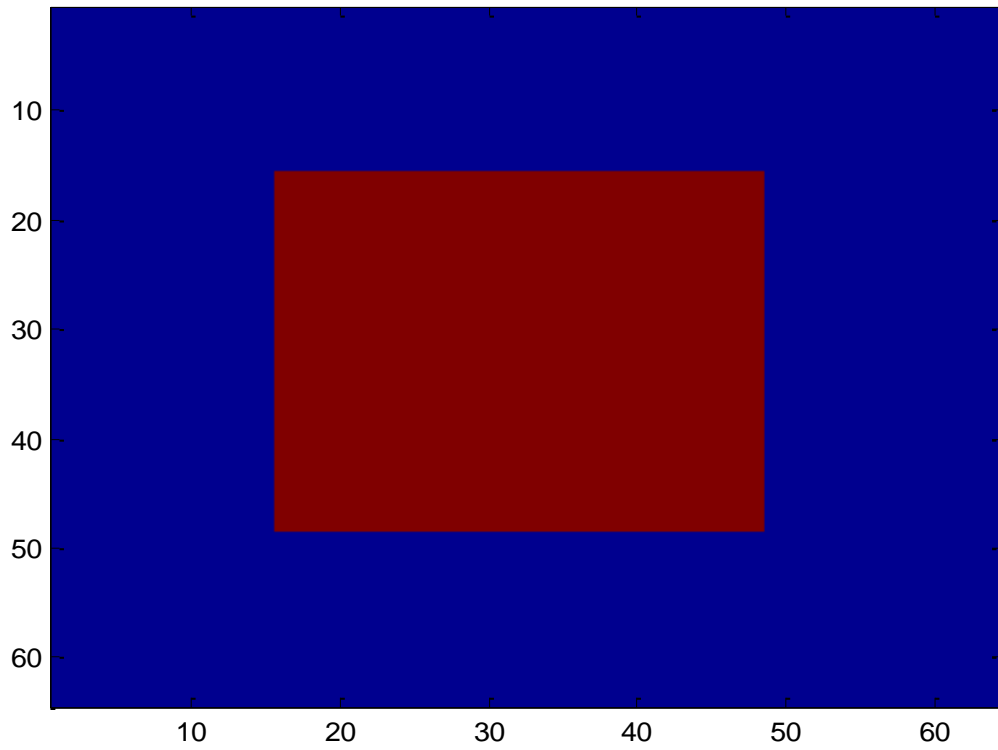


Figure 8.1 - Original Image of Square with Electrical Size of  $2\lambda$

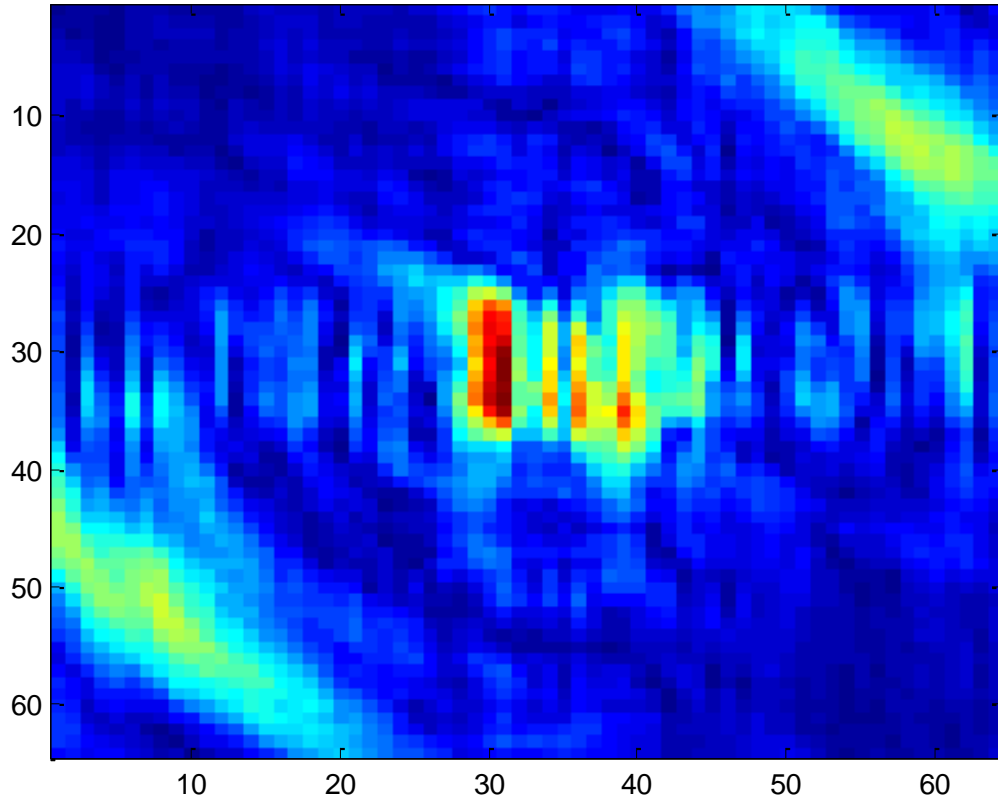


Figure 8.2 - Reconstructed Image with 64 Sensors at 5° Projection Increments

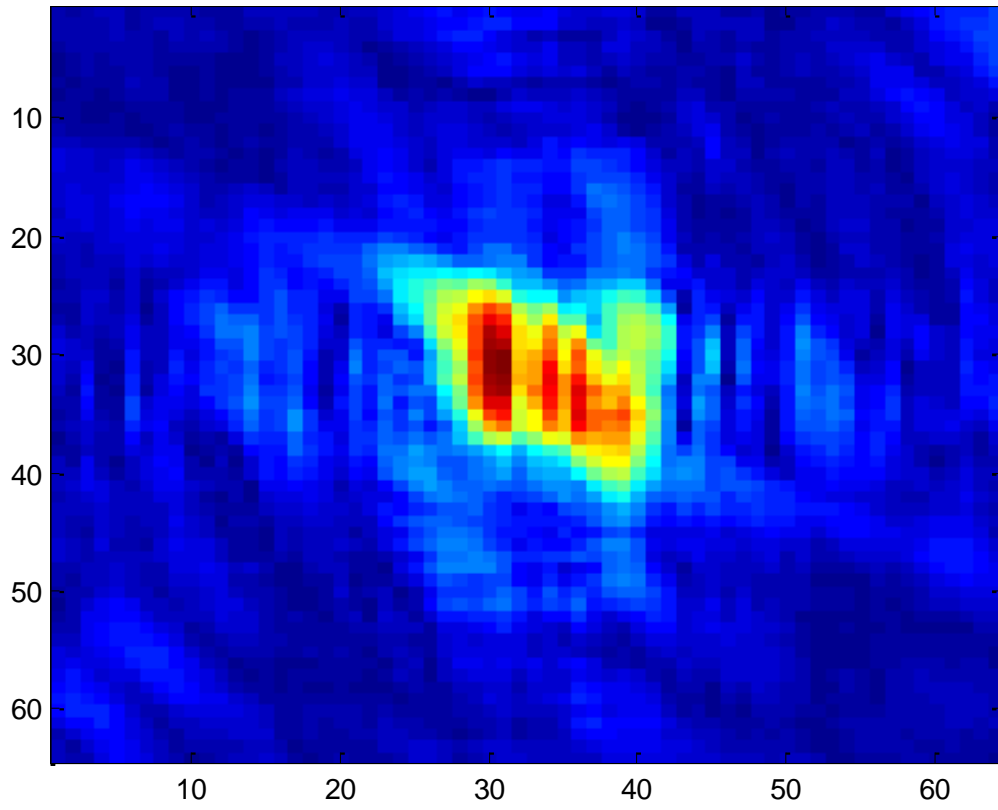


Figure 8.3 - Reconstructed Image with 128 Sensors at  $2^\circ$  Projection Increments

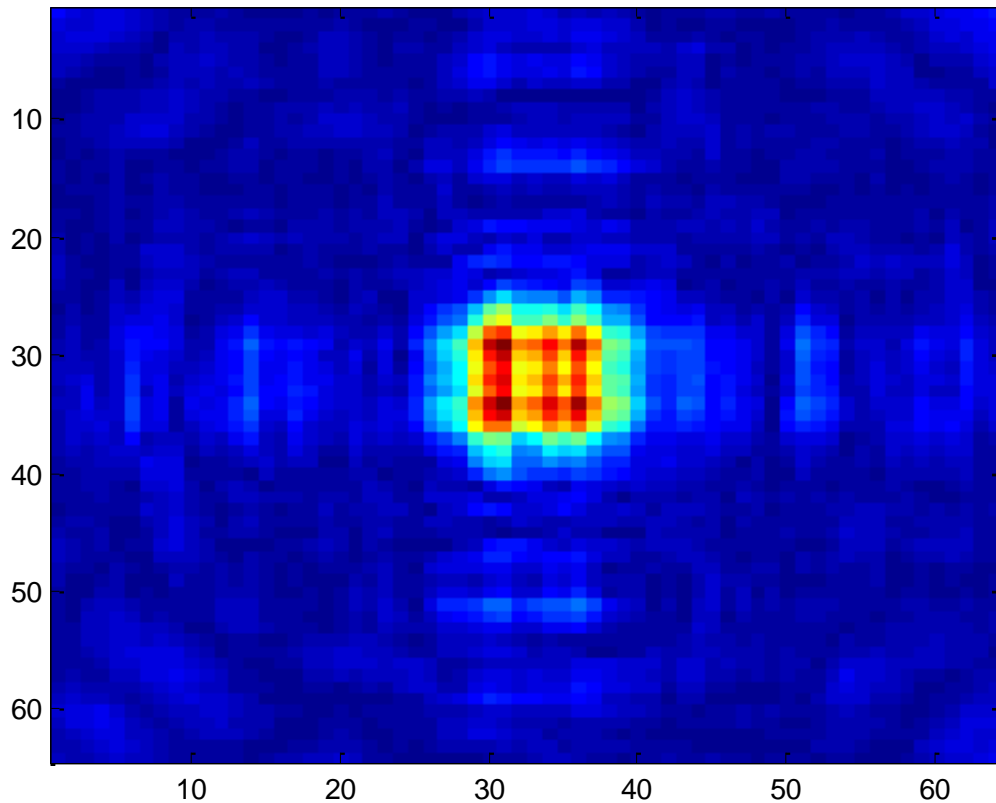


Figure 8.4 - Reconstructed Image with 256 Sensors at 2° Projection Increments

From the first reconstructed image, it is seen that the reconstruction algorithm needs many more data points to fully reconstruct the object, and, in *Figure 8.3*, it can be seen that doubling the number of sensors, as well as increasing the number of readings, the general shape of the object becomes somewhat apparent. Finally, with a total of 256 sensors, the object is very-closely reconstructed to the original shape, as can be seen in *Figure 8.4*.

Currently, the LabVIEW code allows for the rotating stage and antenna control to all be automated so that an object can be imaged by simply specifying the number of sensors and the degree increase per rotation of the stage. One limitation in this system, however, is the temperature that the motor reaches when it has been left on for more than several minutes; a

previous design of the stage melted due to the temperature, so a new stage was designed with a stronger plastic that has a higher melting point. The motor, however, still need to be monitored, as it can still over-heat the plastic stand in a short amount of time. To overcome the temperature issue, the motor and control circuitry can be turned off, but by doing so, there is a small amount of back-lash when the motor is turned back on, and this throws off the angular measurements by a large amount when taking many projections. This, however, will be shortly corrected by using wood to replace the plastic in some of the stage design.

To allow for more sensors to sample the scattered data at smaller intervals, a linear array, constructed out of HDPE plastic, with stepper-motor control, is nearly complete; this will provide much-more accurate reconstruction results, as evident from the previous figures. Once this has been completed, the LabVIEW code will add in the motor control for this second stepper-motor, which will allow for full-automation of the receiver.

The minimal-scan, filtered back-propagation code, outlined in Chapter 2 of this thesis, assumes that the receiver array is in a straight arc, however, with current spatial limitations in the NDE lab, the circular arc provides better isolation from some of the walls and other objects that cause scattering and noise to be integrated into the system, and, so far, we have not seen a noticeable difference in either the scattered fields, or the reconstruction procedures, when using a linear arc versus a curved arc for the receiver array. The noise, however, as mentioned in Chapter 7, does play a significant role in altering the data that is being collected. While the system is currently functioning, the noise floor is high, and a few steps can be taken to have that reduced. First, testing the system in an anechoic chamber would be a good starting point to see how much the noise is actually affecting the data we are collecting. The idea of turning a portion

of our lab into an anechoic chamber was discussed and researched, but the costs of doing so would have been exorbitant, and, at this time, has not been further pursued.

Another option would be to purchase EMI shielding boxes for the switches and for the control circuitry for the stepper-motors that control the rotating stage and linear array movements; as previously mentioned, the circuitry includes 555-timers, which radiate unwanted signals due to the digital clock, which could interfere with the data that the antennas are collecting, as well as coupling onto the feed lines of the switches and the coaxial cables.

Currently, on the post-processing end, weight-filters and the method of total-variation, used for smoothing out the data, is being implemented with the code, which has shown promising results for the simulated data, and is being explored as to how this can be used with the experimental data, but more time needs to be spent searching for how weight filters can be used in experimental data, as that has not been done to this point.